Variability in the Lower Circumpolar Deep Water and the Lazarev Sea

Thesis submitted in accordance with the requirements of the University of Liverpool for the Degree of Doctor of Philosophy by Matthew Simon Donnelly

March 2014

Dedication

This thesis is dedicated to my Nan, Alice Donnelly,
who died a few days after the final version of this thesis was approved.

She was a force of nature as strong as the Antarctic Circumpolar Current,
and her strength and influence will continue to be felt.

Wise words for all PhD students:

"Success is not final,

Failure is not fatal,

It is the courage to continue that counts"

In a flash of academic irony this quote is frequently misattributed to Winston Churchill, and comes from an unknown source. It is nevertheless true.

Acknowledgements

Harry Leach at the University of Liverpool and Volker Strass at the Alfred Wegener Institute (AWI) provided me with the necessary data, guidance and feedback to make progress over the past four years. They also provided me with the invaluable scientific and personal experience of going to sea on *Polarstern*. Boris Cisewski provided useful data and insights regarding the ADCP data collected during the LaKriS campaign.

To my family, thank you for your support and understanding whilst I undertook this challenge. In particular to my wife, Jess; it is impossible to adequately describe how extensive her patience and understanding has been throughout, without which it simply wouldn't have been possible.

To Clare Forshaw, for saving me from being buried by other commitments.

My fellow PhD students and friendly post-docs at the University of Liverpool, AWI and beyond have been the source of vital advice, opinion and friendship without which the experience would have been far more troublesome.

During the final stages of this work a special thank you is due to several people. Firstly to Martin Losch at AWI for exposing some vital considerations regarding inverse theory; to Pascal Salaun in Liverpool for invaluable encouragement, support and useful feedback; and finally to Viena Puigcorbé at the Universitat Autònoma de Barcelona and Elizabeth Jones at AWI for morale support and valued critical feedback.

Ultimate thanks must go to the public of the United Kingdom and of Germany for kindly, and largely unknowingly, funding this work through the National Environment Research Council and the Alfred Wegener Institute. I trust it was worth the investment!

Contents

Preamble

Scarcely a single piece of prose written about the Southern Ocean will fail to mention its uniqueness; and for good reason. The Southern Ocean is the nexus of oceanic circulation, providing the primary direct oceanic link between the Atlantic/Arctic, Pacific and Indian Oceans. The only exceptions to this are the relatively narrow and shallow Bering Strait connecting the Pacific and Arctic basins, and the Indonesian Throughflow. However, these connections are dwarfed by the exchanges of mass, heat, salt, oxygen, nutrients and carbon through the Southern Ocean. As a result, the large-scale global overturning circulation and the associated biogeochemical processes are forced to a significant extent by the physical processes occurring in the Southern Ocean.

The linking of the Global Ocean through the Southern Ocean is particularly notable due to the absence of a meridional barrier at sub polar latitudes. Not only does this isolate the Antarctic continent from the other continents both geographically and climatically, it also gives rise to the only circumnavigating oceanic flow in the form of the Antarctic Circumpolar Current. This eastward circumpolar flow results in a set of circumpolar water masses which – when compared to the differing characteristics of the Atlantic, Pacific and Indian Oceans – are relatively homogeneous. The generic names being Circumpolar Deep Water, Antarctic Intermediate Water, Antarctic Surface Water and Antarctic Bottom Water; however the homogeneity of these water masses is by no means absolute and regional flavours are evident in the different sectors of the Southern Ocean.

The inaccessibility, remoteness and challenging environmental conditions of the Antarctic, which limit the potential for human activity, have allowed a unique political situation to emerge, with the establishment of the Antarctic Treaty in 1961 designating the Antarctic as a region for the betterment of all humankind. Yet despite this stable political situation, the practical challenges and financial cost of accessing the Antarctic mean that there is still to this day a relative scarcity of oceanographic measurements in the Southern Ocean. Recent efforts to establish a Southern Ocean Observing System to bring together the diaspora of observational techniques and countries engaged in Antarctic research appears to have as-yet-unrealised potential, however the availability of high

quality, high density hydrographic data will continue to be problematic due to enduring budgetary constraints. It is with this in mind that this study seeks to make use of existing available hydrographic data in new ways to examine different aspects of the Southern Ocean.

One of the enduring challenges of oceanography is the range of time and spatial scales at work. The overturning of the global ocean occurs over thousands of years and across thousands of kilometres, playing a long-term role in the global climate and consequently imposing long-term controls upon local processes. However, micro-scale turbulence occurring over a few fleeting seconds has not only a local short-term role, but also a cumulatively important role on the overall rate of oceanic stratification and mixing.

From these two examples come two different extreme points-of-view when examining the world's oceans. Firstly the long-term climatic state of the ocean can be seen as the integrated sum of the small scale processes, whereby the chaotically unpredictable micro-processes sum to a variable yet functioning system. Conversely, the small spatial and short temporal variability can be viewed as deviations from a mean dynamically stable state. The reality - such as it might exist - is likely somewhere between those two view points, and the key is to address a particular problem, or set of problems, at an appropriate scale in time and space to allow examination of the components of interest. However, this is far from an easy challenge and requires care, diligence and scientific honesty to confront.

The dynamical environment of the Southern Ocean's Antarctic Circumpolar Current is perhaps the most complex and challenging of environments in which to understand the interleaving impacts of forcing and response. The Antarctic Circumpolar Current has the largest volume transport of any ocean current system on Earth, with strong horizontal property gradients – or fronts – being evident along its entire length through varying parameters, frequently being disturbed by the movement of mesoscale eddies shed from meandering fronts. This eddy activity has a net southward flux, which is balanced by a net northward Ekman transport in the surface ocean. This dynamical

regime influences the interleaving water masses of the surface, intermediate, deep and bottom of the water column, each with their own varying origins, history and characteristics.

Within the Southern Ocean, the large-scale upwelling, modification and subduction of these key water masses occur. Along with similar processes in the Arctic and North Atlantic, it is these modification processes driven largely by atmospheric forcing that are responsible for setting the basic structure of the deep circulation of the entire Global Ocean. These processes are most prevalent near the Antarctic coastline where cold strong winds blowing off the Antarctic continent drive rapid sea-ice formation and the resultant modification of surface water properties. It is thus notable that local coastal processes contribute to a global circulation which also impacts upon individual ocean basins across the globe.

Despite the extent of our collective knowledge of the Southern Ocean, there is still much we do not know. This is particularly so in the realm of quantifying the myriad of processes and translating these into sufficient detail to be represented in global climate models. It is known, for instance, that deep water formation is often simply parameterised using open ocean deep convection, despite knowledge to the contrary. More modelling effort is clearly needed to improve the representation of the Southern Ocean and its processes, but equally the scarcity of measurements makes attempts to compare model output with observations a difficult and uncertain task.

For these reasons, furthering our understanding of the Southern Ocean as a critical component of the global climate system and its variability in both space and time, is a focus of an increasingly large number of investigations. This thesis aims to add to that effort by addressing two important questions.

The first chapter will set the role of the Southern Ocean into greater context, clarifying the framework and background for its examination.

The second chapter will examine a simple 1-dimensional model of the modification of the Lower Circumpolar Deep Water as it moves southwards across the ACC and into the Weddell Gyre. This leads into the third chapter which will address the first question of how variable are the

characteristics of the Lower Circumpolar Deep Water? The variability of the salinity maximum associated with the Lower Circumpolar Deep Water is examined in order to address its spatial variability – from entry via the South Atlantic, through its circumpolar transit, ending with a terminal repository in the Weddell Gyre – by making use of freely available hydrographic data. It also examines temporal variability where repeat data allows, and provides new estimates of deep ocean mixing rates.

The fourth chapter will seek to address the second question of how variable was the volume transport during the Lazarev Sea Krill Study (LaKriS) cruises? The LaKriS cruises provide a rare set of semi-repeat grids of hydrographic measurements near the Greenwich Meridian. This provides the opportunity to attempt to assess seasonal and inter-annual variability by making use of an inverse modelling technique.

The fifth and final chapter will set the knowledge gained from addressing these two questions against the wider knowledge of the Southern Ocean system and consider the implications for future oceanic sampling and research.

Chapter 1

The Southern Ocean System

1.1 Forcing, fronts, water masses and mixing

The Southern Ocean is the primary link between the Atlantic, Pacific and Indian Oceans (Georgi and Toole 1982), providing the conduit for the Global Meridional Overturning Circulation (GMOC) driven by the eastward flowing Antarctic Circumpolar Current (ACC) which flows uninterrupted around the Antarctic continent owing to the absence of a zonal continental barrier (Gordon et al. 1978). The most meridionally constrained part of the ACC's path is within Drake Passage where consistent volume transports with a mean 134 Sv have been observed (Cunningham et al. 2003).

The GMOC transports the warm saline North Atlantic Deep Water (NADW) southwards through the Atlantic, where it becomes part of the Circumpolar Deep Water (CDW) in the ACC. This water mass is distributed into the Indian and Pacific Oceans where it gradually upwells through erosive mixing processes and returns to the Atlantic via the surface circulation. The westerly winds over the ACC force an equatorwards Ekman transport, whilst the easterly winds south of the ACC force a poleward Ekman transport, creating a divergent flow at the Southern Boundary of the ACC. The divergence results in upwelling which is manifest by the upward sloping of isopycnals towards the pole, allowing CDW to move upwards in the water column, with an upper branch of the overturning circulation associated with the equatorward Ekman transport, and a lower branch of the overturning circulation associated with the poleward Ekman transport (Marshall and Speer 2012). Near the Antarctic continent, the CDW is involved in water mass transformation driven by sea-ice formation in the leads and polynyas primarily near the coast and ice-shelves. This leads to the creation of the dense cold saline Antarctic Bottom Water (AABW) which ventilates the deep ocean, spreading over bathymetry and through submarine passages to reach all but the most isolated ocean basins, as demonstrated by Purkey and Johnson (2010). Garabato et al. (2003) describe the

distinction between denser Lower CDW where topographic mixing is important in the ACC, and lighter Upper CDW where the air-sea-driven diapycnal volume fluxes are dominant.

Cold fresh surface waters formed by summer sea ice melt are advected northwards by Ekman transport and are subducted within the ACC to form Antarctic Intermediate Water (AAIW) which also spreads northward into the South Atlantic, Indian and South Pacific Oceans (Sallée et al. 2010). These two processes form the upper and lower branches of the GMOC in the Southern Ocean (see Figure 1.1 for an Atlantic-centric depiction of the MOC).

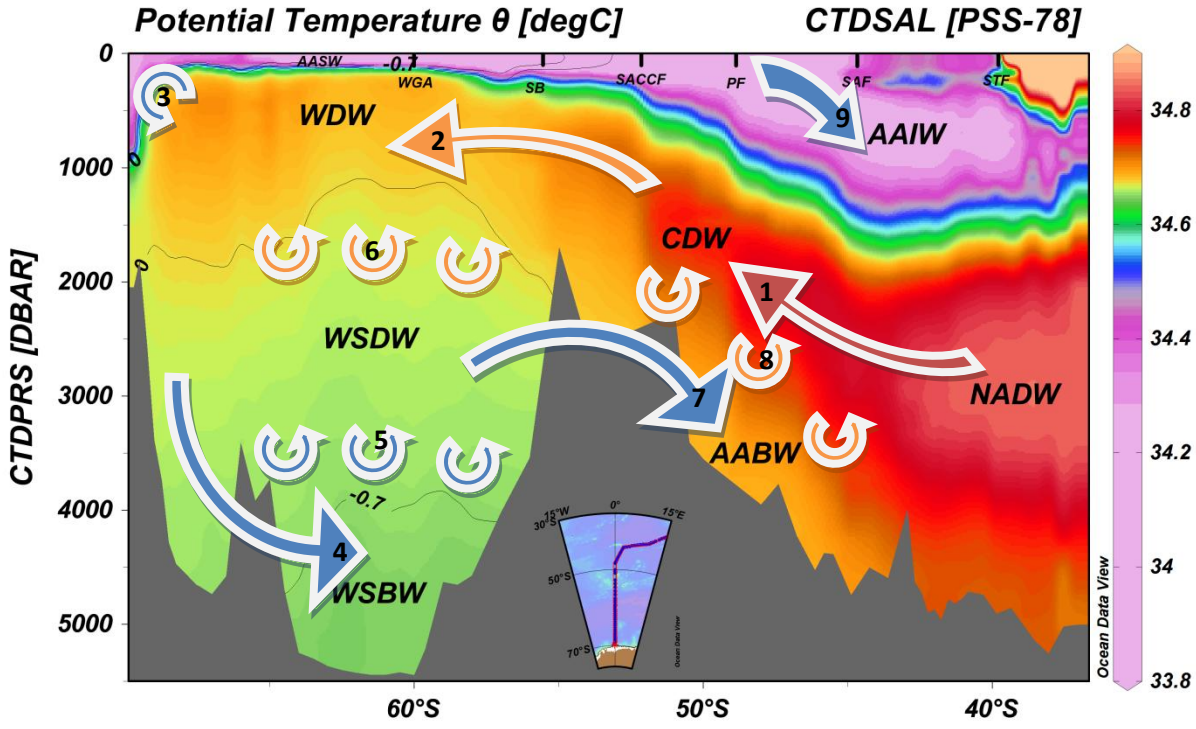

Figure 1.1 – Section of practical salinity (filled contours) with potential temperature (black contour lines at -0.7°C and 0°C demarking Weddell Gyre deep water mass boundaries) along the A12 cruise track (inset).

Water masses are indicated as follows: North Atlantic Deep Water (NADW), Circumpolar Deep Water (CDW), Warm Deep Water (WDW), Antarctic Surface Water (AASW), Antarctic Intermediate Water (AAIW), Weddell Sea Deep Water (WSDW), Weddell Sea Bottom Water (WSBW), Antarctic Bottom Water (AABW).

The position of the Southern Ocean fronts are indicated: Weddell Gyre Axis (WGA), Southern Boundary (SB), Southern ACC Front (SACCF), Polar Front (PF), Sub-Antarctic Front (SAF) and Sub-Tropical Front (STF).

A schematic of the upper and lower Southern Ocean limb of the global meridional overturning circulation: (1) entrainment of NADW into the ACC, (2) entrainment of CDW into Weddell Gyre, (3) dense water formation over the continental shelf, (4) sinking of dense water, (5) upward mixing into WSDW, (6) upward mixing into WDW, (7) export of AABW over bathymetry, (8) mixing of AABW with overlying CDW, (9) downwelling of AAIW.

The formation of dense waters is highly variable around Antarctica, with the greatest volume of AABW resulting from dense water formation over the broad deep continental shelves in the south-western Weddell and Ross Seas which allow the intrusion of CDW onto the shelf, and lesser volumes from the narrower shelf around the East Antarctic coast (Grumbine 1991). The presence of large ice shelves enhances the deep water formation by preconditioning cold dense Ice Shelf Water (ISW) and High Salinity Shelf Waters (HSSW).

The combined action of the spatially and temporally variable density driven GMOC and wind driven ACC give rise to the distribution of oceanic tracers (Orsi et al. 1995). The deep water masses of the Southern Ocean are advected eastwards by the ACC and shifted gradually poleward by the action of mesoscale eddies crossing the strong meridional property gradients known as fronts (Hibbert et al. 2009). These fronts are associated with strongly sloping isopycnals and maxima in sea surface height gradients (Sokolov and Rintoul 2002) giving rise to large zonal velocities of up to ~20 cm s^{-1} in the surface ocean. These fronts vary in space and time (Moore et al. 1999) although they are quasi-permanent features (Sokolov and Rintoul 2009a). The horizontal/isopycnal mixing across the ACC is primarily facilitated by the cross frontal transport of mesoscale eddies below the Ekman layer (Smith and Marshall 2009) formed by the meandering of the frontal barrier. However, leaky fronts in the wake of bathymetry allow for the enhanced poleward movement of the water column demonstrating far more complicated local variations of the ACC system than classically described (Naveira Garabato et al. 2011).

The process of diapycnal mixing acts to modify water masses as they move over one another (Orsi et al. 1999). Diapycnal mixing is low over smooth deep bathymetry but enhanced over shallow rough bathymetry (Polzin et al. 1997, Zika et al. 2009, Ledwell et al. 2010), reinforcing the importance of bathymetry on ocean circulation.

1.2 Bathymetry, the ACC and Antarctic gyres

The Antarctic Circumpolar Current is known to follow the major bathymetric features of the Southern Ocean as shown in Figure 1.2 by the location of the fronts from Orsi et al. (1995) and described by many authors. Starting in the eastern Atlantic sector, the Southwest Indian Ridge (SWIR) provides the initial boundary between the sub-tropical circulations to the north and polar gyres to the south, with the ACC centred over the ridge. Further east near 30°E the ACC spreads laterally southwards as the Weddell Gyre diminishes. To the north the Sub-Antarctic and Polar Fronts are steered by the twin presence of Del Cano Rise and Conrad Rise.

The ACC fronts are most distantly spread as they pass north and south of the Kerguelen Plateau at ~80°E. The Southern Boundary and Southern ACC Front remain near the continental slope whilst the Sub-Antarctic and Polar Fronts are steered along the Southeast Indian Ridge (SEIR). Through its broken ridge system, the Macquarie Ridge acts to steer the ACC as it passes between New Zealand and Antarctica. The flow is then steered north-eastward by the presence of the Pacific-Antarctic Ridge, before being deflected through the Udintsev and Eltanin Fracture Zones.

East of the fracture zones the ACC spreads laterally again due to the lack of bathymetric control and crosses the Amundsen, Bellingshausen and Mornington Abyssal Plains. At these longitudes the Southern Boundary of the ACC is aligned closely with the continental slope which guides the ACC along the Antarctic Peninsula. The ACC is steered through the bathymetrically constricted Drake Passage and into the Scotia Sea. Here, the Sub-Antarctic Front meanders northwards around the Falkland Escarpment and along the continental slope of South America, with the other fronts also diverting north-eastwards leading to another meridional spreading of the ACC. The Southern Boundary and Southern ACC Front tend to wrap around the Scotia Arc. The flow narrows upon return to the Southwest Indian Ridge across ~10°E.

South of the ACC lie the largely open abyssal plains and the broad and deep continental shelves of Antarctica. In addition to the seamounts and plateaus beneath the ACC, there are a number of similar features south of the current offering island refuge to a broad range of species owing to

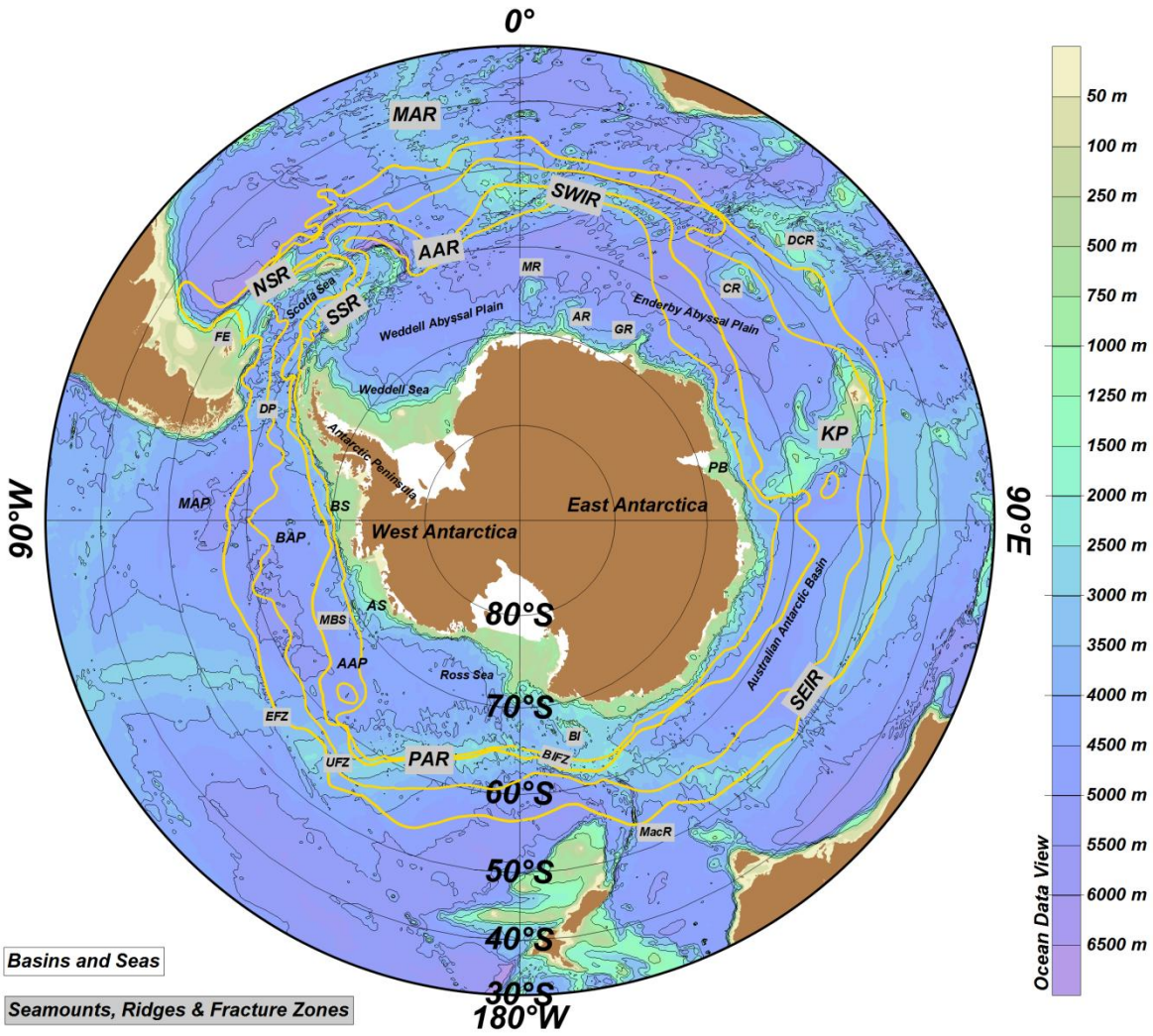

Figure 1.2 – Major bathymetric features of the Southern Ocean. The following abbreviations have been used:

Basins and seas: Amundsen Abyssal Plain (AAP), Amundsen Sea (AS), Bellingshausen Abyssal Plain (BAP), Mornington Abyssal Plain (MAP), Prydz Bay (PB).

Major ridge systems: Mid-Atlantic Ridge (MAR), Southwest Indian Ridge (SWIR), Kerguelen Plateau (KP), Southeast Indian Ridge (SEIR), Pacific-Antarctic Ridge (PAR), North Scotia Ridge (NSR), South Scotia Ridge (SSR), American-Antarctic Ridge (AAR), Drake Passage (DP) , Falkland Escarpment (FE).

Smaller bathymetric features: Maud Rise (MR), Astrid Ridge (AR), Gunneras Ridge (GR), Conrad Rise (CR), Del Cano Rise (DCR), Macquarie Ridge (MacR), Balleny Islands (BI), Balleny Islands Fracture Zone (BIFZ), Udintsev Fracture Zone (UFZ), Eltanin Fracture Zone (EFZ).

North to south, the Sub-Antarctic Front, Polar Front, Southern ACC Front and Southern Boundary from Orsi et al. (1993) are displayed as yellow lines

their advantageous physical, chemical and biological characteristics (Brandt et al. 2011). There are a few notable polar seamounts and ridges including: Maud Rise, Astrid Ridge and Gunnerus Ridge in

the Weddell-Enderby Basin; the Balleny Islands to the west of the Ross Sea; and the Marie Byrd Seamount rising from the Amundsen Abyssal Plain. Unlike the bathymetric features in more accessible locations such as the Kergeulen Plateau and the Scotia Arc, many of these have been poorly sampled.

Complex bathymetry on the continental shelf is influenced by the presence of marine terminating glaciers and floating ice shelves, which produce regions of particularly intense dense water formation. Bathymetry is therefore of great significance in the Southern Ocean not only because of its impact on ocean circulation, as previously discussed, but also because of its importance in the formation of dense water through water mass modification.

In addition to the ACC, there exists a number of large-scale cyclonic gyre circulations south of the Southern Boundary. East of the Antarctic Peninsula lies the Weddell Gyre which is protected from the flow of the ACC by the peninsula's zonal barrier and the South Scotia Ridge along the gyre's northern flank. This gives rise to the Weddell Front which emerges from the Weddell-Scotia Confluence trailing from the tip of the Antarctic Peninsula (Heywood et al. 2004). Inflow of LCDW into the eastern limb of the Weddell Gyre occurs at ~30^{o}E where the eddy field dominates transport (Gouretski and Danilov 1993).

The deep Australian-Antarctic Gyre lies east of the Kerguelen Plateau (McCartney and Donohue 2007) and demonstrates the major impact of bathymetry on oceanic circulation on a large-scale. The ACC fronts split either side of the Kerguelen Plateau and the ACC then overlies the deep gyre flow in the Australian-Antarctic Basin. The deep gyre is the result of a subsurface zonal barrier, much like how the Weddell Gyre is protected by the Antarctic Peninsula. However, the Ross Gyre does not have the same bathymetric protection from the ACC as provided by the Antarctic Peninsula or the Kerguelen Plateau. The Pacific-Antarctic Ridge which occurs at ~3000m is much deeper, and thus represents a different dynamic environment (Gouretski 1997) and this leads to different characteristics of the local AABW (Muench et al. 2009). The bathymetric constraints are limited and so do not retain bottom waters to the extent that occurs in the Weddell Gyre, instead these flow freely

north and eastward filling basins, rather than needing to overflow significant bathymetry. Thus whilst both the Weddell and Ross Gyres produce AABW, the different dynamical regimes give rise to a different method of distribution and different characteristic of dense water. Specifically, the Weddell Sea Bottom Water has a minimum Practical Salinity (S_P) ~34.64 and minimum $\theta \sim -1.0^oC$, whilst Ross Sea Bottom Water has a more saline minimum S_P ~34.70 and warmer minimum $\theta \sim -0.5^oC$ (Mantyla and Reid 1983, Orsi et al. 1999, Pardo et al. 2012) which are propagated beyond the area of formation. Attempts to directly compare production and export rates can therefore be misleading as they are not of identical origin (Gouretski 1997, Orsi and Wiederwohl 2009). Lesser gyres exist in smaller embayments, such as in the Cosmonaut Sea/Prydz Bay where the Amery Ice Shelf is thought to provide a tertiary area of significant AABW production (Comiso and Gordon 1996, Nunes Vaz and Lennon 1996).

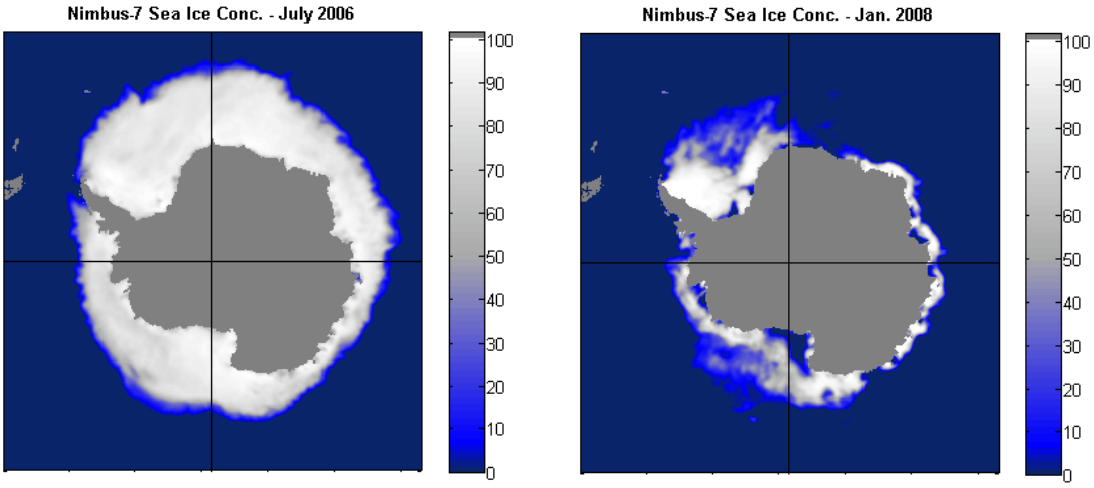

Figure 1.3 – Nimbus-7 monthly sea ice concentrations from the NSIDC for July 2006 and January 2008 (covering the periods of two Lazarev Sea Krill Study cruises) showing the Austral winter and Austral summer sea-ice concentrations respectively.

The gyres are regions in which the lower branch of the overturning circulation occurs and thus control the formation of dense water. The significant lateral recirculation of the gyres may buffer the high-latitude Antarctic seas from short-term changes in water mass properties. The gyres provide the environment for a large seasonal sea-ice zone which experiences rapid changes in cover from Austral summer to Austral winter (Figure 1.3).

1.3 The significance of the deep salinity maximum

The significant role of the Southern Ocean in the global climate system has already been elucidated. However, the critical link in the lower overturning cell of the Southern Ocean has particular significance as it supplies the source waters which feed into the climate critical water mass modification processes driven by sea-ice formation.

Further understanding of the deep ocean link between the ACC and the Weddell Gyre through the transfer of LCDW into the WDW is of critical importance to assessing the response of Antarctica to changes in the global climate system. The eastern Weddell Gyre in particular appears to be a key region for the regulation of deep polar heat transport and these processes may represent one of the long-term climatic tipping points which could switch a relatively stable and insulated Antarctic cryosphere – the Antarctic Peninsula and eastern Bellingshausen Sea not withstanding (Martinson et al. 2008) – into a rapidly warming region despite the atmospheric barrier posed by the polar vortex (Joseph and Legras 2002). This assertion arises from the eddy saturation of the ACC whereby increased energy input from the westerly winds, rather than accelerate the ACC, may act to increase the residual overturning circulation through an increased eddy transport across the ACC (Lauderdale et al. 2013). Such an increase in eddy transport would facilitate an increase in thermohaline fluxes and thus reduce the effective strength of the meridional barrier posed by the ACC.

It has been observed that the thermohaline signature of the LCDW/WDW is capable of having short-term effects. There is a recurrent loss of sea ice from the middle of the ice pack west of Maud Rise owing to the warming of the surface ocean in the wake of the bathymetry. A warming of the inflowing LCDW or a modification of its circulation could lead to the recurrence of the Weddell Polynya (Smedsrud 2005) and a general decrease of sea-ice cover in Antarctica. Such an effect is already being felt by the reduced sea-ice cover and retreating marine terminating glaciers on the west Antarctic Peninsula due to the on-shelf transport of warm CDW (Martinson et al. 2008).

Key to understanding the circulation of WDW into the Weddell Sea proper is first assessing the variability of the LCDW within the ACC and subsequently examining the variability of the transport through the Lazarev Sea, where the Greenwich Meridian is one of the best sampled sections in the Southern Ocean and the LaKriS campaign offers a wider distribution of repeat gridded hydrography.

Chapter 2

A 1-Dimensional Model of Lower Circumpolar Deep Water Transformation

2.0 Abstract

A simple 1-D model was created to demonstrate in basic terms the effect of the southward transit of the Lower Circumpolar Deep Water (LCDW) across the Antarctic Circumpolar Current (ACC) into the Weddell Gyre. A single hydrographic section from the A12 WOCE cruise line was used as an initial profile, with a prescribed vertical mixing coefficient and set boundary conditions for the surface and deep ocean to represent the southward changes in overlying surface and bottom waters with which the LCDW mixes. An upwelling term is included to mimic the effects of Ekman suction drawing deeper water towards the surface and the topographically constrained dense waters of the Weddell Gyre which act to force the LCDW upwards in the water column. The result is a LCDW which first rises rapidly up towards the typical depth of the Warm Deep Water (WDW) in the Weddell Gyre and then remains at that depth whilst the salinity maximum moves to higher densities as a result of mixing with surrounding water masses.

2.1 Introduction

The Lower Circumpolar Deep Water in the Antarctic Circumpolar Current (ACC) exists at a fairly constant neutral density layer of 28.04-28.08 kg m^{-3} throughout its circumpolar journey **(detailed in Chapter 3)**. However, when LCDW is entrained into the Weddell Gyre as Warm Deep Water (WDW) the salinity maximum associated with the LCDW and WDW shallows dramatically and increases in density. A simple 1-dimensional model is used to illustrate how the transport of the LCDW/WDW and its interaction with overlying and underlying water masses act to modify the density profile of the water column and help explain why, outside of the ACC regime, the tracking of the salinity maximum remains an acceptable technique for assessing water mass changes in the LCDW/WDW throughout its Southern Ocean journey.

Imagine that a hydrographic profile is being carried along by the ACC and as it does so it is slowly being drawn southwards into the Weddell Gyre, whilst mixing with the overlying and underlying water masses. As a result of the poleward movement, the characteristics of these boundary water masses will change. The northward Ekman transport – out of the Weddell Gyre – results in near-surface waters occupying a shallower depth range south of the ACC. This includes the absence of Antarctic Intermediate Water (AAIW) which only subducts near the Polar Front within the ACC (Sallée et al. 2010).

Dense water which forms over the Antarctic continental shelf mixes with deeper waters as it descends the continental slope to the deep ocean. This leads to the formation of topographically constrained Weddell Sea Deep Water (WSDW, $-0.7^{o}C < \theta < 0^{o}C$) and Weddell Sea Bottom Water (WSBW, $\theta < -0.7^{o}C$) (Eberhard et al. 1995, Gordon et al. 2001), the former of which is present at depths as shallow as 1100m compared to the salinity maximum of the LCDW in the ACC which can lie at depths of up to 2500m. The presence of WSDW and WSBW acts to force the LCDW/WDW upwards from beneath, resulting in the shoaling of isopycnals and the rise of LCDW/WDW in the water column.

The standard framework for considering the ACC includes transport being dominated by streamlines of eastward flow aligned with the position of circumpolar fronts and a strong dependence on the sloping isopycnal surfaces associated with these fronts for tracking conservative tracers. This is against the background of a strong northward Ekman transport and an opposing southward flux below by the mesoscale eddy field. However, whilst this approach is suitable for the ACC, the Weddell Gyre represents a different dynamical regime characterised by the recirculation of gyre water masses, water mass transformation, and interaction with the ACC along the northern and western boundaries of the gyre. This brief study explores a simple example to explain the observed changes in the properties of the LCDW as it is entrained into the Weddell Gyre.

2.2 Source Data, Boundary Constraints and Model Setup

To provide a useful real baseline, the hydrographic profile from station 25, cast 1 of the 2002 A12 cruise track undertaken during *FS Polarstern's* expedition ANT-XX/2 was used as the starting hydrographic profile. The station was located at 49^{o}S, 2.8^{o}E placing it south of the Sub-Antarctic Front but north of the Polar Front.

At the surface boundary, the sea surface temperature decreases by 0.005^{o}K per time step to represent the decreasing surface temperature moving towards Antarctica, whilst the sea surface salinity is constant to represent the general stability and relative freshness of the Antarctic Surface Water. The potential temperature at the bottom boundary of 4000m decreases by 0.0018^{o}K per time step and the salinity decreases by 0.00005 per time step, mimicking the transition into the WSBW/WSDW regime at depth.

These linear changes were derived from the total meridional temperature and salinity gradient over the A12 section as a representative trend for surface and bottom waters. As both surface and bottom waters are formed locally, these boundary conditions provide a reasonable first order approximation to real oceanographic conditions, although clearly this is an idealized approach.

In the vertical, the grid was set at 101 grid points, spaced every 40m from 0m to 4000m. The initial A12 profile was used for the model down to a depth of 4000m (of a total cast depth of 4090m), whilst the shallowest data (at 9 dbar) was used as the surface value. Except the surface values there were no missing data.

The 1-dimensional model is based around simple equations for the modification of potential temperature and salinity:

$$\theta_t = \theta_{t-1} + \frac{d\theta}{dt}.dt \quad where \quad \frac{d\theta}{dt} = \kappa\frac{(\theta_{i-1} - 2\theta_i + \theta_{i+1})}{(\Delta z)^2} + w\frac{\theta_i - \theta_{i-1}}{\Delta z}$$

$$S_t = S_{t-1} + \frac{dS}{dt}.dt \quad where \quad \frac{dS}{dt} = \kappa\frac{(S_{i-1} - 2S_i + S_{i+1})}{(\Delta z)^2} + w\frac{S_i - S_{i-1}}{\Delta z}$$

where θ is potential temperature, S is practical salinity, t is time, i is the vertical grid spacing positive downwards, z is the vertical co-ordinate positive downwards, κ is the diapycnic diffusivity coefficient, and w is the uplift rate.

An approximated 12 year transport duration was derived from an estimated 40000 km track from the station location in the ACC eastward into the Weddell Gyre at an assumed 1 cm s^1, rounded down to the nearest whole year. The number of time steps was set at 365 and the time step size set to 120 days for a simple scaling of the duration. This is consistent with the distances and times discussed in Chapter 3, whereby LCDW is shown to recirculate in the ACC before entering the gyres.

The vertical thermal diffusivity coefficient, κ, was set to 5 x 10^{-5} m^2 s^{-1} which falls within the range of many studies of vertical mixing in the ocean (e.g. Munk 1966, Naveira Garabato et al. 2004, Zika et al. 2009). In addition, to represent the rise of LCDW/WDW in the water column, a rate of water column uplift of 20 m yr^{-1} was applied.

Both potential density and Neutral Density were calculated based upon the new potential temperature, practical salinity and pressure at each time step.

2.3 Results

The initial and final profiles of the 1-D model shown in Figure 2.4 includes: an overall decrease in temperature at all depths; a marked increase in salinity in the upper water column but a slight decrease in deeper waters resulting in the upward shift of the salinity maximum; and an overall increase in the density of the profile.

The salinity time-series contour shown in Figure 2.5a illustrates the rapid upward shift of the salinity maximum as the profile moves into the modelled regime of the Weddell Gyre. Salinity stabilises at depth reflecting the shallow salinity gradient in the WSDW and WSBW whilst a shallow fresh layer is retained. The potential temperature shown in Figure 2.5b shows a steady decrease at all depths, with the temperature maximum remaining at about 100m depth.

Density, as shown for potential density in Figure 2.5c and for Neutral Density in Figure 2.5d, increases at depth resulting in a decreasingly stratified deep water column, whilst the surface boundary constraint results in a strongly stratified upper water column. The key result is that density increases at depth such that the salinity maximum initially uplifts at a similar rate to the neutral surfaces (see Figure 2.5d) until about year 70 when the density at the salinity maximum increases whilst the depth of the salinity maximum stabilises at about 400m depth after 80 years. The intervening period represents the entrainment of the water mass into the Weddell Gyre proper.

2.4 Discussion & Conclusion

The framework for examining the ACC described earlier is well established, however, this framework does not extend to the transition to the hydrographic regime of the Weddell Gyre (Schröder and Fahrbach 1999). This 1-D model shows an initial decrease in the depth of LCDW from ~2500m to ~400m, paralleling the north-south distribution of temperature, salinity and density evident on sections crossing the ACC into the Weddell Gyre.

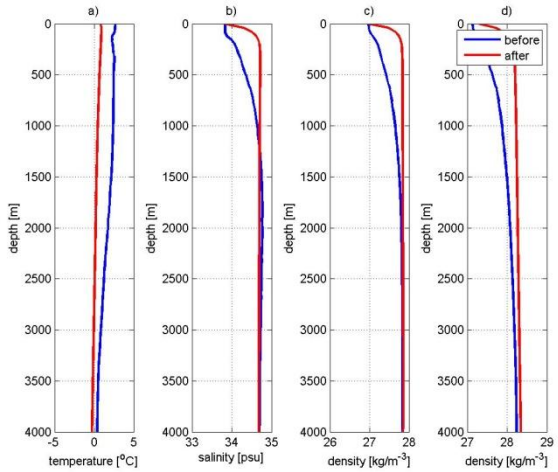

Figure 2.4 - Initial and final profiles of a) potential temperature, b) practical salinity, c) potential density (σ_θ) and d) Neutral Density (γ_n)

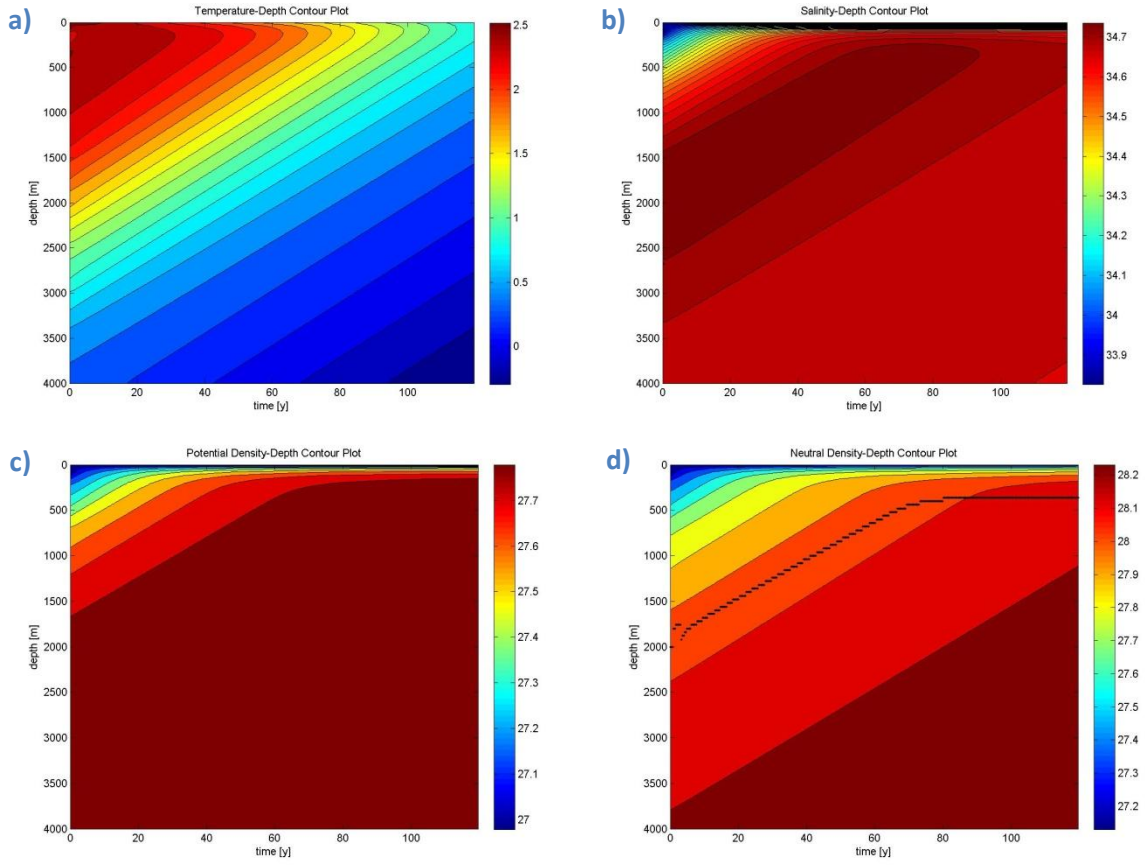

Figure 2.5 – Time-series contours of a) potential temperature, b) practical salinity, c) potential density (σ_θ) and d) Neutral Density (γ_n). Figure 2d) also includes the position of the salinity maximum (black line) to demonstrate its migration through density space.

Whilst simple, this model – when viewed as a representation of the mean-state of more complex Southern Ocean dynamics over long time scales – serves to demonstrate what the broad-scale effect of crossing from one regime to another has upon the core of the LCDW. The core of a traditional tracer can be mixed and advected over multi-year time scales to produce a result which is consistent with observations. Whilst within the core of the ACC the salinity maximum remains within a constant density layer, this is not the case as the regime shifts from a circumpolar flow to the Weddell Gyre circulation. The normal framework for examining the ACC on streamlines and isopycnal surfaces does not apply beyond the Southern Boundary of the ACC, where complicated processes of advection, mesoscale eddies and frontal meandering together modify the water column. Recognition must be given to the effects of the contrasting hydrographic regimes of the ACC and Weddell Gyre, which demonstrate a situation in which the signal of the deep salinity maximum crosses isopycnal surfaces.

Chapter 3

Variability and Mixing in the Lower Circumpolar Deep Water

3.0 Abstract

A collection of 37 hydrographic sections undertaken over a period of 20 years in the Southern Ocean as part of the WOCE/CLIVAR program provides the opportunity to assess the variability of the deep salinity-maximum associated with the origin, circulation and fate of the Lower Circumpolar Deep Water (LCDW). This includes quantifying the circumpolar trend of the salinity-maximum, the assessment of entrainment and the calculation of deep ocean mixing rates. A circumpolar decrease in the value of the salinity maximum is observed eastwards from the North Atlantic Deep Water (NADW) in the Atlantic sector of the Southern Ocean through the Indian and Pacific sectors to Drake Passage. This is followed by limited cross-frontal mixing processes in the Atlantic sector which act to mediate the poleward salinity signal and insulates the Weddell Gyre from direct influence by the NADW. Limited entrainment occurs into the Weddell Gyre, with LCDW entering primarily through the eddy dominated eastern limb. A vertical mixing coefficient of $\kappa_V = (2.86 \pm 1.91) \times 10^{-4}\ m^2\ s^{-1}$ and an isopycnic mixing coefficient of $\kappa_I = (8.97 \pm 2.13) \times 10^{2}\ m^2\ s^{-1}$ are calculated for the eastern Indian and Pacific sectors of the Antarctic Circumpolar Current (ACC). A $\kappa_V = (2.39 \pm 0.73) \times 10^{-5}\ m^2\ s^{-1}$, an order of magnitude smaller, and a $\kappa_I = (2.47 \pm 0.27) \times 10^{2}\ m^2\ s^{-1}$, three times smaller, are calculated for the southern and eastern Weddell Gyre. This reflects a more turbulent regime in the ACC and a less turbulent regime in the Weddell Gyre. In agreement with the findings of other studies, we propose that the ACC acts as a meridional barrier to transport and mixing due to the eastward propagation of the deep salinity-maximum signal, insulating the Weddell Gyre from short-term changes in NADW characteristics.

3.1 Introduction

The Southern Ocean is dominated by two main circulation features: the Antarctic Circumpolar Current (ACC) and the Meridional Overturning Circulation (MOC). The MOC acts on a large scale to transport North Atlantic Deep Water (NADW), which has origins in the North Atlantic, southwards into the Southern Ocean as Circumpolar Deep Water (CDW). CDW is brought towards the surface by sloping isopycnals in the Southern Ocean, with the upper branch being advected northwards by the MOC. This results in Upper Circumpolar Deep Water (UCDW) undergoing modification to form Antarctic Intermediate Water (AAIW) in the Antarctic Convergence. The lower branch composed of Lower Circumpolar Deep Water (LCDW) – identified by the deep salinity maximum – is advected further southwards and undergoes modification processes driven by sea-ice formation over the continental shelf to form denser Antarctic Bottom Water (AABW). This aspect of the MOC is further complicated in the presence of the Antarctic gyres where modified local forms of deep water masses are formed such as the fresher Warm Deep Water (WDW) in the Weddell Gyre (Orsi et al. 1993).

Simultaneously, the eastward flowing ACC is a sustained equivalent-barotropic circumpolar flow within which Antarctic Surface Water (AASW), AAIW, CDW and AABW are transported. These water masses are often treated as being relatively homogenous due to their circumpolar distribution, however local flavours have been demonstrated to exist owing to variable rates and characteristics of water mass modification processes.

The transport of the ACC is associated with circumpolar fronts formed by strong meridional density gradients. The common major fronts from north to south are: the Sub-Antarctic Front (SAF), Polar Front (PF), the Southern ACC Front (SACCF) and the Southern Boundary (SB). North of the SAF lies the Sub-Antarctic Zone (SAZ) which is dominated at depth by the NADW in the Atlantic sector of the Southern Ocean. The ACC includes the enhanced transport associated with the SAF, PF and SACCF and incorporates the Polar Front Zone (PFZ) to the north of the PF and Antarctic Zone (AZ) to the south of the PF, dominated at depth by the CDW. South of the SB of the ACC lies the

coastal waters and Antarctic gyres dominated by local deep water masses modified from CDW (Orsi et al. 1995). These represent clear circulation regimes.

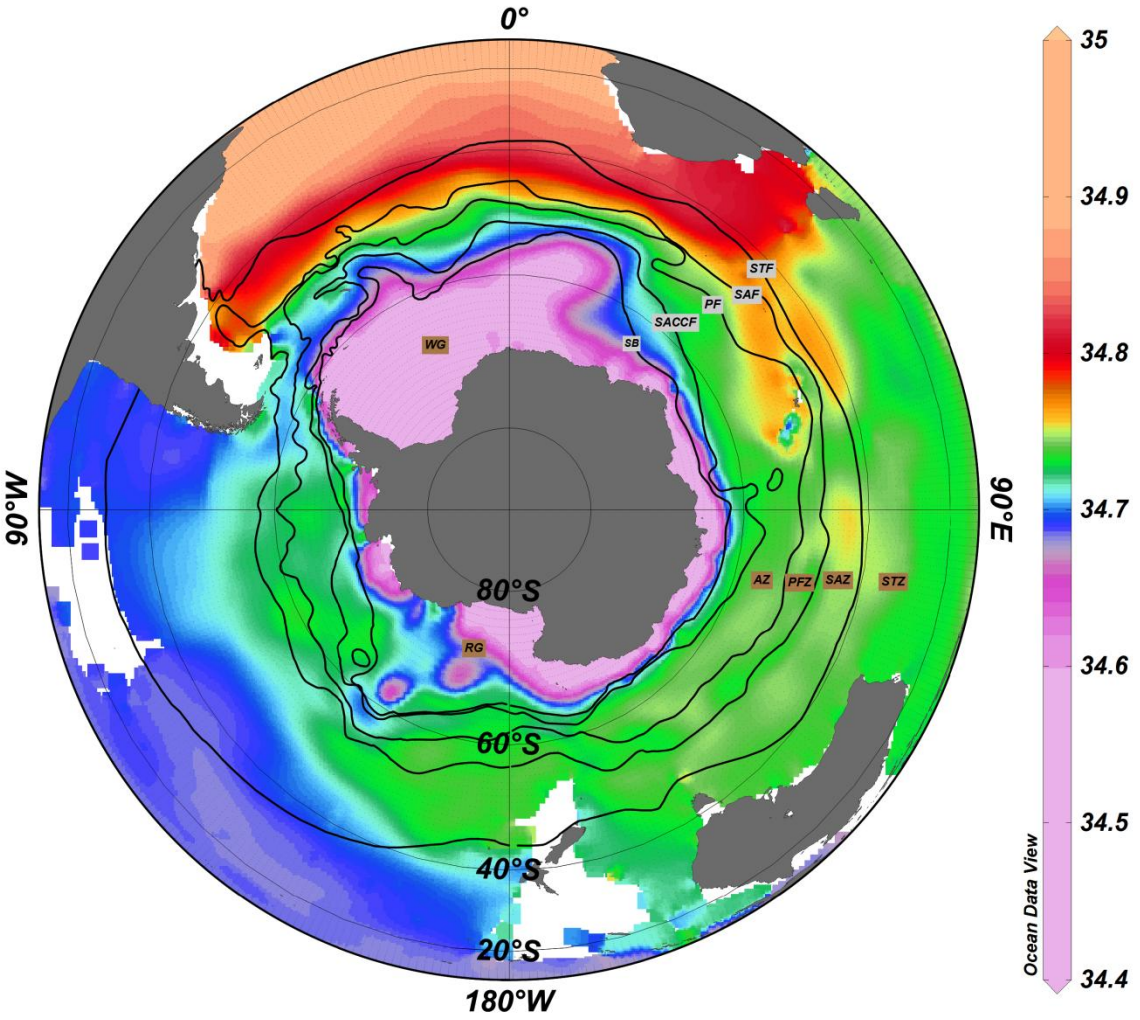

Figure 3.6 – Salinity on the 28.05 kg m^{-3} Neutral Density surface from the World Ocean Atlas 2009 with the major fronts (black lines and grey highlighted labels) and zones (brown highlighted labels) as follows: Sub-Tropical Front (STF), Sub-Antarctic Front (SAF), Polar Front (PF), Southern ACC Front (SACCF), Southern Boundary (SB), Sub-Tropical Zone (STZ), Sub-Antarctic Zone (SAZ), Polar Front Zone (PFZ), Antarctic Zone (AZ), Weddell Gyre (WG) and Ross Gyre (RG).

A more complex view presented by Sokolov and Rintoul (2009a, 2009b) identifies the consistent alignment of multiple ACC jets/frontal filaments with particular streamlines along the circumpolar path. By tracking the sea surface height contours they show that the positions of these fronts vary but are consistently present, which in turn supports a quasi-constant transport for the ACC. This set of studies suggests that the multiple circulations of water masses within a relatively stable

ACC may provide the conditions for LCDW with a dampened temporal variability, whilst permitting an advected downstream change in the salinity-maximum of the LCDW.

Many studies have sought to examine either one or the other circulation feature. However it is their combined spatial and temporal variability acting upon hydrographic properties which together give rise to the distribution of conservative tracers, as described in chapter 1. This is well demonstrated by the distribution of salinity along the Neutral Density surface, γ_n = 28.05 kg m^{-3} shown in Figure 3.6. This Neutral Density surface corresponds to the density of the spatially variable core of the deep salinity-maximum. The highest values are in the South Atlantic, with an eastward moving core evident through the Indian and Pacific sectors of the Southern Ocean. Upon return to the South Atlantic via Drake Passage a strong salinity gradient is present across the AAC spanning a depth range of some 2000 m, with the freshest deep waters found in the gyre to the south. In Drake Passage the LCDW salinity maximum has been observed as reaching a local minimum of S_P ~34.73 by Whitworth and Nowlin (1987) and Naveira Garabato et al. (2002a).

Variability of the transport in the Southern Ocean and the characteristics of CDW over different timescales have been noted by a variety of authors, including, Gille (2002), Meredith and Hogg (2006), Sokolov and Rintoul (2009a, 2009b), and Turner and Overland (2009). Indeed many authors have taken into consideration the local condition of the LCDW in particular sectors of the Southern Ocean (for example: Naviera Garabato et al. (2002a) in the Scotia Sea, Gladyshev (2008) along 30^{o}E, and Bindoff et al. (2000, 2009) in the Ross Sea). Callahan (1972) examines the general distribution of water masses across the deep Southern Ocean, identifying the broad trends in the LCDW. Williams et al. (2006) provide a detailed study of the variability of the LCDW within Drake Passage and observe no long-term trend in the salinity-maximum between 1926 and 2004. They also provide a brief examination of the circumpolar characteristics of the LCDW as reproduced in Figure 3.7. However a detailed recent examination of the circumpolar change of the salinity maximum along the ACC seems absent since Callahan (1972).

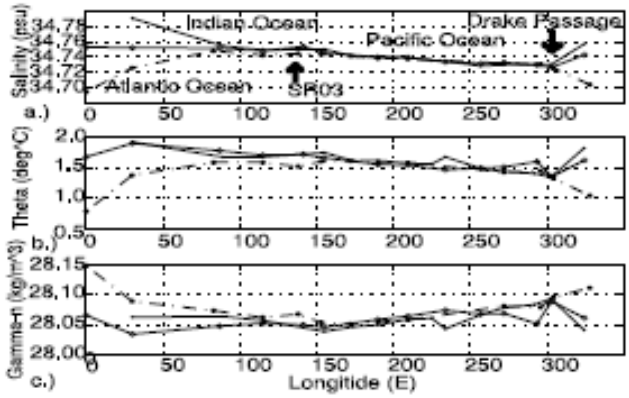

Figure 3.7 – Property variability of the LCDW salinity maximum layer determined from WOCE meridional hydrographic sections (1990-1996). Properties are followed along three continuous dynamic height contours at the sea surface relative to 2000 m (0.7(dot-dash), 0.9(thin black, circles) and 1.1(thick black) dyn m). a) Salinity, b) potential temperature (θ), c) Neutral Density. Reproduced from Williams et al. (2006)

A key part of the framework of both the ACC and the MOC is the crucial role of mixing in balancing the movement of water masses. It is recognised that at different spatial and temporal scales different mechanisms for mixing can be less or more important, with the size of vertical and horizontal mixing being scale dependent (Okubo 1971, Ledwell et al. 1998). For instance, at the mesoscale level, the balance between turbulent and diffusive processes may be of significance to variability of local water mass properties. In the spirit of Munk (1966), on a global scale the bulk mixing between different water masses – irrespective of exactly how that mixing occurs – forms an important and intrinsic part of the global thermohaline circulation.

There have been many studies of mixing conducted in various parts of the ocean and here a brief overview is presented. Naveira Garabato (2004) obtained an estimate of $K_V = 3 \times 10^{-4}$ m^2 s^{-1} to 1 x 10^{-2} m^2 s^{-1} in Nordic Seas; Munk (1966) estimates a bulk K_V of 1.3 x 10^{-4} m^2 s^{-1} for the Pacific interior, and in an earlier paper Munk (1950) required $K_H = 5 \times 10^3$ m^2 s^{-1} in order to obtain a realistic scale for the western boundary current of a wind driven gyre; Cisewski et al. (2005, 2008) obtain a $K_V = 7 \times 10^{-4}$ m^2 s^{-1} in the upper pycnocline of the ACC at ~20°E; Hibbert et al. (2009) obtains a maximum $K_V = 3 \times 10^{-4}$ m^2 s^{-1} and K_H = 30-100 m^2 s^{-1} within a cold core eddy. These provide a useful backdrop for this study. As will be alluded to in the methods of this investigation, there are

different approaches and definitions when determining mixing through the water column. For purposes of inter-study comparison, the vertical mixing coefficient (κ_V) and diapycnic mixing coefficient (κ_D), along with the horizontal mixing coefficient (κ_H) and isopycnic mixing coefficient (κ_I), can be considered to be roughly analogous, however they are derived by different means within different frameworks and this must be remembered whilst comparing values. In the ocean gyres where isopycnals do not significantly slope, the difference between the two sets of quantities is less than in the ACC where the strongly sloping isopycnals associated with the ACC fronts are strongly inclined compared to the isobars.

The next part of the thesis outlines the range of data and source of various types of data used in this study. Part 3.3 outlines the methods and considerations for examining the circumpolar variability of the salinity-maximum, estimates of entrainment and a mixing equation for calculating mixing coefficients. Part 3.4 presents the results following on from the content of part 3.3, and part 3.5 places those results into context. Part 3.6 finishes by presenting an interpretation of the Southern Ocean system based on the results and discussion.

3.2 Data

This study has made use of the available 'merged'-format CTD data from the CLIVAR and Carbon Hydrographic Data Office (CCHDO) website (http://whpo.ucsd.edu/). The CCHDO website provided a readily searchable range of data which was openly available for use and gave access to a circumpolar coverage of hydrographic data. An earlier study examining the LCDW by Williams et al. (2006) primarily focused on Drake Passage, although used a similar but less extensive set of sections to complete a cursory review of the circumpolar salinity changes. They likewise obtained their circumpolar data from the CCHDO, however this study makes use of additional cruise data which has more recently been released through the CCHDO.

In total 37 hydrographic sections were used in this study, as detailed in Table 3.1. The earliest cruise undertaken was the SR02-A section along the Greenwich Meridian in 1989, and the latest was the I06S section undertaken in 2008 along 30°E. Only those stations falling on the main section of each cruise were used, and only those stations whose profile reached an observable salinity maximum peak associated with the core of LCDW were considered for analysis.

A total of five sections undertaken in the western Drake Passage by the research vessel *Vidal Gormaz* between 1993 and 1998 were not included in the analysis due to anomalous salinity values which suggested a problem with salinity calibration.

A further section, P17A in the Pacific sector undertaken in 1992 by the research vessel *Knorr* was not included in this study due to a large longitudinal shift in the middle of the cruise track. This shift in cruise track was covered by only a single station spanning the vicinity of the Udintsev and Eltanin Fracture Zones on an orientation nearly perpendicular to the known topographically steered ACC path (Orsi et al. 1995). As such it was deemed unwise for inclusion in the analysis as any re-gridding of data would introduce unacceptable levels of uncertainty.

Two further sections, P17E (1992) and P18 (1994) in the Pacific sector, were excluded as the cruises did not extend sufficiently far south to reach the Southern Boundary of the ACC, likely due to ice cover during the time of occupation.

The approximate position of the Polar Front as defined by Orsi et al. (1995) was used as a proxy for the centre of the mean ACC path in order to obtain a circumpolar path length, as shown in Figure 3.8.

Finally, estimates of ocean velocity were obtained from the Estimating the Circulation & Climate of the Ocean (ECCO) project. This data was obtained from the Live Access Server for ECCO-GODAE version 3, iteration 73 using the adjoint method, with 1 degree horizontal resolution and 23 vertical levels. The model solutions span 1992-2007 which includes the majority of the timeframe of the CCHDO data and was the most suitable of the available solutions for this study.

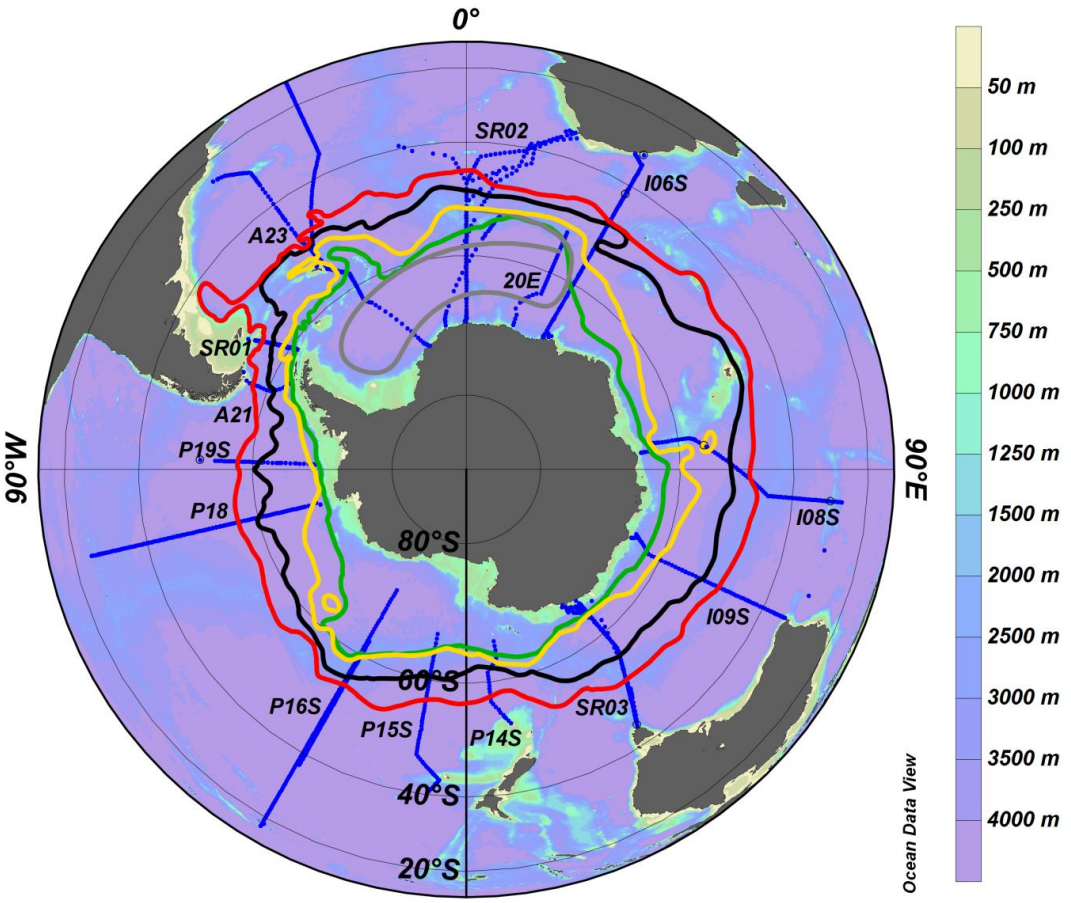

Figure 3.8 – Distribution of all cruise stations used in this study (blue dots) with corresponding sections names. Fronts from Orsi et al. (1995) are shown to illustrate the extent of the ACC: Southern Boundary (green), Southern ACC Front (yellow), Polar Front (black) and Sub-Antarctic Front (red). The Polar Front is used to calculate the circumpolar path length of the ACC. The estimated path for the Weddell Gyre is shown in grey.

Section code (1)	Approx. Longitude (2)	Sub-section no. (3)	Eastward path distance from Greenwich Meridian, including sub-section tags (4)	Cruise ref. Code (5)	#	EXPO code (6)	Cruise dates (7)
A23	35°W (for ACC)	1 3 16 21 22	-2900 (SAZ) -2900 (PFZ) 24400 (AZ) 32800 (SWG)* 35400 (NWG)*	A23	103	A16S_74JC10_1	20th Mar - 6th May 1995
				A16S-2005*	60	A23_33RO200501	11th Jan - 24th Feb, 2005
SR02	0°	2 4 17 20 23	0 (SAZ) # 0 (PFZ) # 27300 (AZ) ^ 31800 (SWG) * 37100 (NWG) *	SR02 # ^	51	SR02_06MT11_5	6th Sept - 8th Oct, 1989
				SR02-A *	43	SR02_06AQANTVIII_2	6th Sept - 8th Oct, 1989
				A12-1992 # ^*	52	A12_06AQANTX_4	21st May - 5th Aug, 1992
				S04A *	48	S04_06AQANTXIII_4	17th Mar - 20th May, 1996
				SR04-E # ^*	46	SR04_06AQANTXV_4	31st Mar - 21st May, 1998
				A12-1999 ^*	26	A12_06ANTXVI_2	9th Jan, 1999 - 16th Mar, 1999
				A12-2000 # ^*	28	A12_06ANTXVIII_3	11th Dec, 2000 - 11th Jan 2001
				A12-2002 # ^*	11	A12_ANTXX_2	26th Nov, 2002 - 15th Jan, 2003
I06S	30°E	5 18	2200 (ACC) 30300 (EWG)	I06S-A	30	I06SA_35MFCIVA_1	23rd Jan - 9th Mar, 1993
				I06S-B	28	I06SB_35MF103_1	20th Feb - 22nd Mar, 1996
				I06S-2008	27	I06S_33RR20080204	4th Feb - 17th Mar, 2008
I08S	90°E	6	7800	I08S	27	I08S_316N145_5	1st Dec, 1994 - 19th Jan, 1995
				I08S-2007	33	I8S_33RR20070204	4th Feb - 18th Mar, 2007
I09S	115°E	7	9600	I09S	35	I09S_316N145_5	1st Dec, 1994 - 19th Jan, 1995
SR03	141°E	8	11500	SR03-A	20	I09S_09AR20041223	25th Sept - 27th Oct, 1991
				SR03-B	30	SR03_09AR101_1	11th Mar - Apr 03, 1993
				SR03-C	16	PR12_09AR309_1	1st Jan - 1st Mar, 1994
				S03	12	PR12_09AR407_1	13th Dec, 1994 - 2nd Feb, 1995
				SR03-D	28	SR03_09AR9404_1	17th Jul - 2nd Sept, 1995
				SR03-G	5	SR03_09AR9501_1	22nd Aug -22nd Sept, 1996
				SR03-2001	22	SR03_09AR9601_1	29th Oct - 22nd Nov, 2001
P14S	172°E	9	13500	P14S	15	SR03_09AR200011029	5th Jan - 10th Mar, 1996
P15S	170°W	10	14500	P15S	23	P14S_31DSCG96_1	5th Jan - 10th Mar, 1996
P16S	150°W	11	15800	P16A	23	P15S_31DSCG96_1	6th Oct - 25th Nov, 1992
				P16S	23	P16A_316N138_9	9th Jan - 19th Feb, 2005
P18	103°W	12	18800	P18-2008	43	P16S_33RR200501	15th Dec , 2007 - 23rd Feb, 2008
P19S	88°W	13	19900	SR01-B	53	P17E_316N138_10	11th Nov - 17th Dec, 1992
				P19S	75	P18S_31DSCG94_2	4th Dec, 1992 - 22nd Jan 1993
A21	68°W	14	21200	A21	29	P18_33RO20080121	23rd Jan - 8th Mar, 1990
SR01	57°W	15	22100	SR01-E	65	SR01_74DI198_1	20th Nov - 18th Dec, 1993
				SR01-F	18	P19S_316N138_10	13th Nov - 12th Dec, 1994
				SR01-K	66	A21_06MT11_5	15th Nov - 20th Nov 1996
				SR01-M	43	SR01_74JC27_1	27th Dec, 1997 - 7th Jan, 1998
20E	20°E	19 24	30900 (SWG) 38500 (NWG)	A12-20E	32	A12_ANTXX_2	26th Nov, 2002 - 15th Jan, 2003

Table 3.1 – Details of cruises used from the CCHDO database. Partitioned sections denoted with the accompanying symbols *, ^, # in column 4 are only occupied by the correspondingly marked sections in column 5. All other non-marked sections are covered by all occupations. # denotes total number of stations used per cruise.

3.3 Methods

3.3.1 Distribution of the salinity-maximum

The initial step in examining the variability of the NADW north of the ACC, the LCDW within the ACC and the WDW in the Weddell Gyre is to evaluate the distribution of the salinity signal in space and time. This includes examining individual cruise potential temperature-practical salinity (θ-S_P) plots and comparing conservative temperature and absolute salinity (Θ-S_A) plots for the salinity-maximum across all cruises.

In order to examine the circumpolar spatial variability of the salinity-maximum associated with the LCDW it is necessary to consider the different regimes in which it is present. Firstly, it is necessary to separate NADW in the South Atlantic Gyre from the LCDW in the ACC, and the LCDW in the ACC from the WDW in the Weddell Gyre. This was achieved through setting maximum (1.823 dyn m) and minimum (0.732 dyn m) limits for the dynamic height at 20 m referenced to 2500 m as a proxy for the respective northern and southern boundary of the ACC. A depth of 20m provides a consistent level at which all stations were sampled to avoid problems with missing data from the near-surface of profiles. Williams et al. (2006) use a reference level of 2000 m for their investigation of LCDW variability, however Sokolov and Rintoul (2009a) use a deeper reference level of 2500m which maximises the mass included in the dynamic height calculation whilst minimising the area of ocean discounted due to shallower topography, and the latter was deemed the preferable reference level.

The next step is to partition the Atlantic Sector of the ACC into the Polar Front Zone and the Antarctic Zone by establishing a section specific position for the Polar Front. There are many different definitions based on different parameters at different depths. In this study the 2.2^{o}C isotherm at 800m was chosen as the preferable option as it is a deep, as opposed to surface signature, which was clearly observable in almost all sections.

The final step in section partitioning was to delineate between the northern and southern limbs of the Weddell Gyre. After interrogation of the data, the criterion used to determine the central

axis of the Weddell Gyre was the latitude of maximum Neutral Density at 300 m (the approximate depth of the Salinity-maximum in the WDW). The doming of density surfaces is thought to be related to variability in the transport of the Weddell Gyre (Meredith et al. 2011) and the northward/southward sloping of the surfaces related to eastward/westward transport. Thus the maximum in Neutral Density represents an estimate of the central axis where near zero-flow occurs.

Using this partitioning, an examination of the variability along the circumpolar path of the LCDW can be conducted with respect to longitude and time, taking into consideration depth and the value of the salinity-maximum.

3.3.2 Appropriateness of Sampling

The majority of cruise sections used in this study have been undertaken with a regular sampling pattern where a standard distance exists between one station and the next, within the limits of a research vessel being able to maintain station. Given that small scale fluctuations over these distances are at least as large as the variability between stations; this negated the need to grid the CTD data onto an equidistant spacing. Such a gridding process would introduce unnecessary error and false confidence in data coverage. Furthermore, the partitioning of sections in the Atlantic Sector of the Southern Ocean into their various regimes avoids the likelihood of cross-regime sampling bias.

The only region where station spacing is cause for concern is the varying northern coverage of the South Atlantic. However, as this study only refers to this northerly data generically as a source of the LCDW signal, and is not involved in subsequent mixing calculations there was no need to attempt to regularise the data distribution. Given the generally sparse and irregular sampling of more northerly waters in this dataset, it would be even less desirable to attempt to re-grid this northerly data than in the case of the more regularly spaced data straddling the ACC and Weddell Gyre.

3.3.3 ACC and WG Track Length

The along ACC path distance was calculated between each pair of sections using the position of the Polar Front estimated by Orsi et al. (1995). The Polar Front is the latitudinal centre of the ACC fronts, however frontal positions can vary in time by up to 5^{o} latitude as described by Moore et al.

(1999). In addition, branches of the main fronts diverge and converge at various points in time and space around the Southern Ocean, as described by Sokolov and Rintoul (2009a, 2009b). Therefore, any representation of the fronts will at best be an approximation to the mean state and therefore the position of the Polar Front from Orsi et al. (1995) is considered a sufficient approximation to the mean ACC path length. This was used for both demonstrating spatial variability and for calculating a term of the mixing equation.

In order to determine an estimate of the pathway of the LCDW/WDW through the Weddell Gyre, the partitioned sections were analysed to identify an approximate latitudinal centre for each section. In conjunction with examining the circumpolar salinity trend, a corresponding distance track was calculated using Ocean Data View's 'Graphic Objects' tool.

3.3.4 Entrainment Estimate Equation

In an effort to examine the relative downstream contributions of the salinity maximum between different regimes in the Atlantic sector of the Southern Ocean, a series of basic entrainment calculations were made. Specifically, the entrainment of NADW into the LCDW of the ACC and the entrainment of LCDW into the WDW of the Weddell Gyre are examined where the pathway is identified by the circumpolar salinity trend. The ratio of contributions from two source sections to a downstream mixed section is calculated as follows:

$$[1] \quad C_{S2} = \frac{\overline{S_{S1}} - \overline{S_M}}{\overline{S_{S1}} - \overline{S_{S2}}}$$

$$[2] \quad C_{S1} = 1 - C_{S2}$$

Where $\bar{S}$ is the average section salinity-maximum value; subscripts denote the highest salinity-maximum contributor (S_{S1}), the lowest salinity-maximum contributor (S_{S2}), and the mixed end-point value (S_M); and C is the fractional contribution from the corresponding subscript. The calculation is a rough estimate to gauge the overall contribution to the downstream salinity signature without making an inference regarding actual mass contributions or the rates of contribution. Instead it is a simple metric to examine the broad structure of the Atlantic sector regime.

3.3.5 Mixing Estimate Equation

The equation

In order to make an estimate of the rate of mixing along the path of the LCDW a diffusive-advective mixing scheme is assumed to sufficiently approximate the large-scale effects of mixing across a range of smaller scales:

$$[3] \quad \frac{\partial S}{\partial t} + u\frac{\partial S}{\partial x} + v\frac{\partial S}{\partial y} + w\frac{\partial S}{\partial z} = \kappa_H\left(\frac{\partial^2 S}{\partial x^2} + \frac{\partial^2 S}{\partial y^2}\right) + \kappa_V\frac{\partial^2 S}{\partial z^2} + R$$

$$[4] \quad R = -\frac{\partial}{\partial x}(\overline{u'S'}) - \frac{\partial}{\partial y}(\overline{v'S'}) - \frac{\partial}{\partial z}(\overline{w'S'})$$

Where $\frac{\partial S}{\partial t}$ is the change in salinity with time; u, v, w are respectively the mean zonal, meridional and vertical components of velocity; $\frac{\partial S}{\partial x}, \frac{\partial S}{\partial y}, \frac{\partial S}{\partial z}$ are respectively the mean change in salinity in the zonal, meridional and vertical directions; κ_H is the horizontal mixing coefficient & κ_V is the vertical mixing coefficient; $\frac{\partial^2 S}{\partial x^2}, \frac{\partial^2 S}{\partial y^2}, \frac{\partial^2 S}{\partial x^2}$ are respectively the uniform rate of change in salinity gradient with respect to the zonal, meridional and vertical directions; and R represents the eddy flux components of the Reynolds Stress terms as shown in [4]. Despite the dynamic nature of the Southern Ocean, the terms of [3] must be assumed to be uniform values.

Assessment of terms

Using scale analysis we can determine which, if any of these terms can be neglected in calculating rates of oceanic mixing.

On the LHS, firstly we can reasonably neglect the $\frac{\partial S}{\partial t}$ term as this study did not identify an observable temporal trend in the source of the salinity signal: the salinity maximum of the NADW. Next we can neglect the $v\frac{\partial S}{\partial y}$ term as the meridional transport across the ACC is dominated by transient eddies and is relatively small compared to the zonal transport; furthermore individual

meridional hydrographic sections can poorly resolve meridional velocities. Similarly, the $w\frac{\partial S}{\partial z}$ term can also be neglected as vertical transport is relatively small compared to zonal and meridional transport, and when considered within the context of shoaling isopycnals this term is even less significant.

On the RHS, we can neglect the $\frac{\partial^2 S}{\partial x^2}$ term as it estimated to be ~10^{-16} m^{-2}, whereas the $\frac{\partial^2 S}{\partial y^2}$ is estimated at ~10^{-14} m^{-2} and therefore dominates the overall term relating to κ_H. Finally, there is insufficient information to accurately include the Reynold's Stress terms and so the effect of the terms must be implicitly included in the remaining terms. This leaves us with:

$$[5] \quad u\,\frac{\partial S}{\partial x} = \kappa_H \frac{\partial^2 S}{\partial y^2} + \kappa_V\,\frac{\partial^2 S}{\partial z^2}$$

However, owing to the nature of the ACC, where the isopycnal surfaces are strongly sloping, it is necessary to alter the equation to represent isopycnal (κ_I) rather than horizontal (κ_H) mixing, giving us the equation:

$$[6] \quad u\,\frac{\partial S}{\partial x} = \kappa_I \frac{\partial^2 S}{\partial y^2} + \kappa_V\,\frac{\partial^2 S}{\partial z^2}$$

Furthermore, as the path of the ACC meanders across the Southern Ocean it is inappropriate to consider the downstream flow to be strictly zonal or the rate of change in salinity across the ACC to be strictly meridional and the equation therefore becomes:

$$[7] \quad \boldsymbol{u}\,\frac{\partial S}{\partial i} = \kappa_I \frac{\partial^2 S}{\partial j^2} + \kappa_V\,\frac{\partial^2 S}{\partial z^2}$$

Where $\boldsymbol{u}$, the downstream velocity is obtained from the ECCO model; $\frac{\partial S}{\partial i}$ is the downstream change in salinity obtained from an appropriate linear fit of circumpolar changes in salinity; $\frac{\partial^2 S}{\partial j^2}$ is the rate of change in salinity gradient in the across-stream direction. By collecting information on each of these terms for every appropriate section in the circumpolar transit of the LCDW an estimate of bulk

mixing can be obtained for the deep ocean using linear regression. A statistical estimate of error associated with these calculated mixing terms is provided by the standard error of the mean for both the isopycnal and vertical mixing coefficients.

Velocity estimates

It was essential to obtain a realistic estimate for the downstream velocity. At a basic level, if we assume a typical ~150 Sv transport for the ACC through Drake Passage, with a mean depth of 4000 m and an approximate width of 5^{o} of latitude, we arrive at a mean value for *u* of 7.1 cm s^{-1} for the entire water column. This represents an absolute upper bound for velocities at LCDW depth which is in the lower half of the water column.

Döös (1995) estimates a mean residence time for water particles moving between the different ocean basins via the indirect ventilated route in the Southern Ocean to be 243 years. When scaled by the estimated 6 circumnavigations, it suggests a typical circumnavigation time of 40.5 years. Using an ACC circumpolar track length of order 27 000 km derived from Orsi's (1995) Polar Front; this would provide a mean current speed of 2.1 cm s^{-1}. This is an estimate for water masses at a range of mid water column depths and provides a reasonable value well within the upper limit described previously.

Another useful point of reference is the estimate of the mean tangential velocity to the path of the ACC estimated by Olbers et al. (2004). The mean estimate of Southern Ocean velocity suggests velocities ranging from 8 cms^{-1} at depths of ~1000m, decreasing to 2 cms^{-1} at depths of ~3000m: this is consistent with both of the above estimates.

To obtain a robust set of estimates for eastward velocities, the ECCO live access server was used to obtain velocity data for each section spanning the full range of the model solutions, from 1992 to 2008. The average (where repeat occupations occur) north and south limits defined by the section partitioning was used for the meridional limits of the ECCO data at a constant depth relevant to the average depth of the salinity-maximum for each section. A simple time-latitude average was

calculated to obtain a mean velocity. This is a preferable method to calculating individual section transport velocities, say based on hydrography, as such a method would provide only snapshot estimates of velocities when the circumpolar distribution of tracers is determined by the long-term flow.

Second differentials

The terms $\frac{\partial^2 S}{\partial j^2}$ and $\frac{\partial^2 S}{\partial z^2}$ in equation 5 were estimated by calculating the second differential of a quadratic fit to the salinity data. The $\frac{\partial^2 S}{\partial j^2}$ term is obtained from a single fit to the profile of the salinity-maximum along the section. The $\frac{\partial^2 S}{\partial z^2}$ term is the mean of the second differential of the quadratic fit to each station salinity profile, for appropriate ranges of salinity. Within the ACC the vertical quadratic fit was obtained for $S_P > 34.68$, and for the Weddell Gyre $S_P > 34.67$. This discrimination was necessary due to the lower salinity values in the upper water column of the Weddell Gyre.

3.4 Results

3.4.1. Spatial and Temporal Variability of the Salinity-Maximum

The salinity-maximum associated with the NADW, LCDW and WDW (S_P~34.6-34.8, θ~0-3^{o}C) is evident at all latitudes as a 'knee' in the θ-S_P distribution as shown in panel A of Figure 3.9 in the box labelled 'Deep Waters'. Intermediate and surface waters account for the fresher and/or warmer part of the distribution, whilst the increasingly cooler and denser Weddell Sea Deep (WSDW) and Bottom Waters (WSBW) account for the remainder of the distribution. The deep and bottom waters are enlarged in panel B of Figure 3.9.

The salinity-maximum 'knee' successively freshens and cools polewards from the NADW to the CDW, and this pattern is present in each section used in this study and is therefore observable at all longitudes. Of particular note, however, is the reversal of this trend, where the salinity-maximum decreases from the CDW at ~55^{o}S (turquoise) to reach its lowest value at ~60^{o}S (blue), yet there are

higher values further south towards 70°S (pink). This represents the higher salinity maximum in the southern limb of the Weddell Gyre compared to the northern limb demonstrating entrainment of LCDW in the eastern Weddell Gyre.

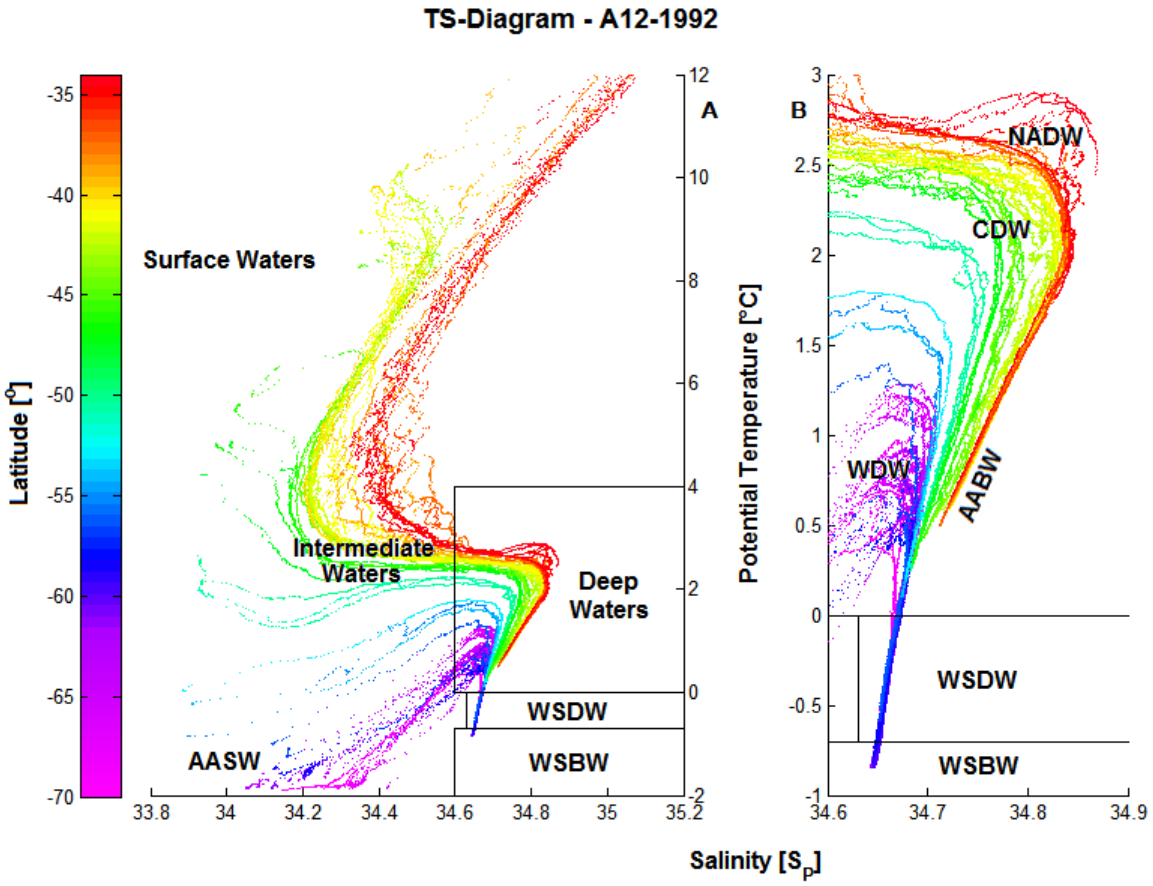

Figure 3.9 – Potential temperature-practical salinity plot coloured by latitude for the A12-1992 cruise along the Greenwich Meridian. Black boxes denote the following water masses: WSBW (θ < -0.7°C); WSDW (0°C < θ < -0.7°C); Deep Waters including the NADW, CDW and WDW (θ > 0°C, S_p > 34.6). AABW is the deepest end-member of the circumpolar water masses. The general distributions of intermediate and surface waters are shown, including AASW.

In order to examine the circumpolar salinity-maximum signature it is necessary to focus on this data only, as shown in Figure 3.10. Overall there is a pattern of warm, saline NADW with a potential density of ~27.85 kg m^{-3} in the Sub-Tropical Zone of the South Atlantic (red) gradually freshening and cooling as the signature moves southward and is entrained into the ACC (black). The cooling and freshening continues but the potential density remains relatively constant at ~27.8 kg m^{-3}

until entrainment into the Weddell Gyre, where a more pronounced cooling results in an increase in potential density to 27.85 kg m^{-3}.

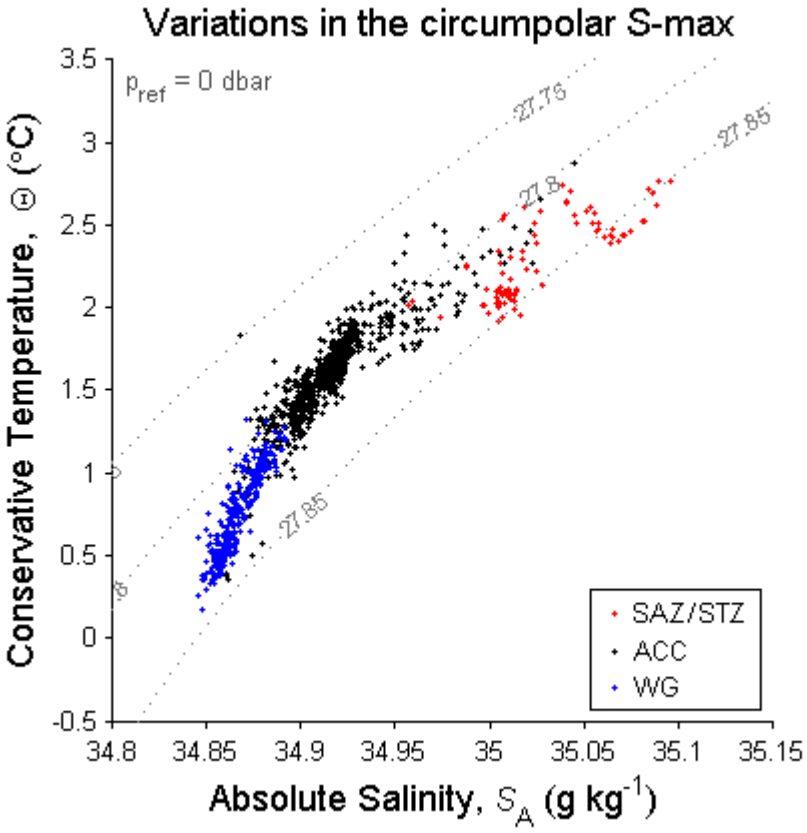

Figure 3.10 – Conservative Temperature-Absolute Salinity plot for all deep salinity-maximum values from all cruises showing the relative distribution according to regimes of the Sub-Antarctic Zone and Sub-Tropical Zone (red), ACC (black) and Weddell Gyre (blue). The potential density surfaces are marked by dotted lines.

The mechanism for this change between regions of the Southern Ocean is described in ***chapter 2*** and can be summarised as being the result of cross-frontal mixing moving the salinity-maximum signature from one regime to another, whereby there is a change in the overlying and underlying water masses and a vertical move upwards in the water column. This study is conducted under the assumption that tracking the salinity maximum along this continuous temperature-salinity curve is legitimate as the changes in density are the result of real modification of the water mass as it moves from regime to regime.

It is worth considering how this modification impacts not only upon potential density, but also upon Neutral Density, as it is the preferred definition of surfaces upon which no energy is required for movement. Panel A of Figure 3.11 shows practical salinity plotted against potential density

demonstrating the same distribution as in Figure 3.10. Note how the distribution changes with latitude (top) reflecting Figure 3.9, and how the distribution changes with longitude (bottom); the Greenwich Meridian (green) and western South Atlantic (turquoise) including the most saline NADW as well as the freshest WDW. The intermediate S_P values are present in the Indian and Pacific sectors of the Southern Ocean (blue and red).

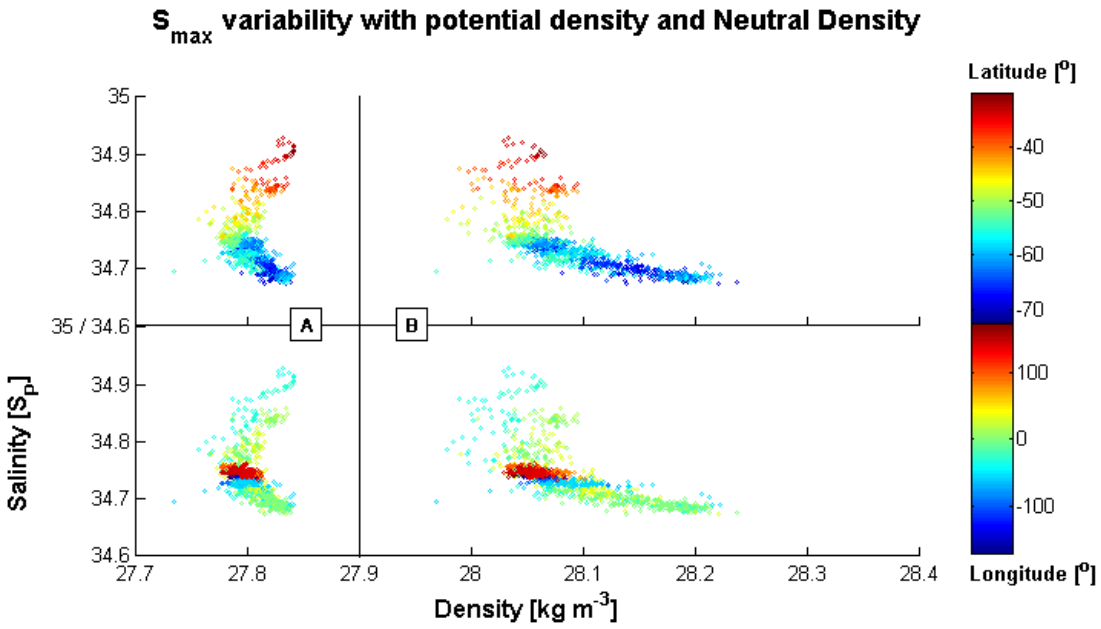

Figure 3.11 – The variability of all the deep salinity-maximum values from all cruises versus: A) potential density referenced to the surface and B) Neutral Density. Data points are coloured by latitude in the top panel and by longitude in the bottom panel.

The dataset curvature of the potential density with S_P (Figure 3.11, panel A) is shown to be around the value of 27.8 kg m^{-3} with high densities associated with NADW and WDW. The equivalent Neutral Density distribution shows a greater range of densities with a mean of approximately the same as for the Neutral Density surface shown in Figure 3.6 of γ_n = 28.05 kg $^{m-3}$ (Figure 3.11, panel B). The prominent departure from the main 'grouping' in Neutral Density space is for the poleward part of the distribution associated with the Weddell Gyre and not the equatorward part of the distribution, reflecting the misleading role of pressure on potential density referenced to the sea surface.

The salinity-maximum is therefore used as a proxy for the overall impact of mixing upon the deep salinity-maximum core of the NADW, LCDW and WDW. It can be used to examine spatial and

temporal variability, entrainment from one regime to another, and to estimate mixing rates along the circumpolar pathway.

3.4.2 Temporal and Spatial Change

The change in the salinity-maximum along the circumpolar pathway can be seen in Figure 3.12a. Starting from the highest NADW salinities, in the Sub-Antarctic Zone (SAZ, sections 1 & 2), NADW is then entrained into the Polar Front Zone (PFZ, 3/4) producing the highest values in the ACC. The salinity-maximum decreases throughout the ACC in the Indian and Pacific sectors of the Southern Ocean and back through Drake Passage and into the Antarctic Zone (A23-AZ) of the Atlantic sector (5-16). There is then a noticeable increase in salinity in the transition from the A23-AZ sections to the SR02-AZ sections resulting from cross-frontal mixing with the PFZ. LCDW is then entrained into the WDW in the eastern Weddell Gyre, with the decrease continuing through the eastern and southern Weddell Gyre. The salinity signature then increases in the northern Weddell Gyre (22-24) due to cross-frontal mixing with the AZ of the ACC.

The change in the depth of the salinity maximum is more variable than the actual salinity values as shown in Figure 3.12b. The NADW values place the salinity maximum at ~2750 m depth, rising to ~2500 m in the Polar Front Zone and stabilising at a depth of ~1500m across the Indian sector. The depth then fluctuates between 1500 m and 2100 m across the Pacific sector apparently due to the combined impact of the shift in the vertical distribution of water masses and topographic effects. In detail, the ACC fronts remain on or south of the Australian-Antarctic Ridge through the Indian sector resulting in the consistent vertical distribution of the overlying AABW and AAIW, corresponding to a steady salinity-maximum depth (see section group 5-8). However, to the east of the Macquarie Ridge the fronts move to the north of the Pacific Antarctic Ridge (~3000m ridge depth) into the Southwest Pacific Basin where lower volumes of AABW are present due to topographic barriers in the northwest Ross Sea, resulting in the downward displacement of the water column and the increased depth of the salinity-maximum (see section group 9 & 10). The salinity-maximum depth shallows as the ACC crosses the Pacific-Antarctic Ridge due to topographic uplift, and returns

a)

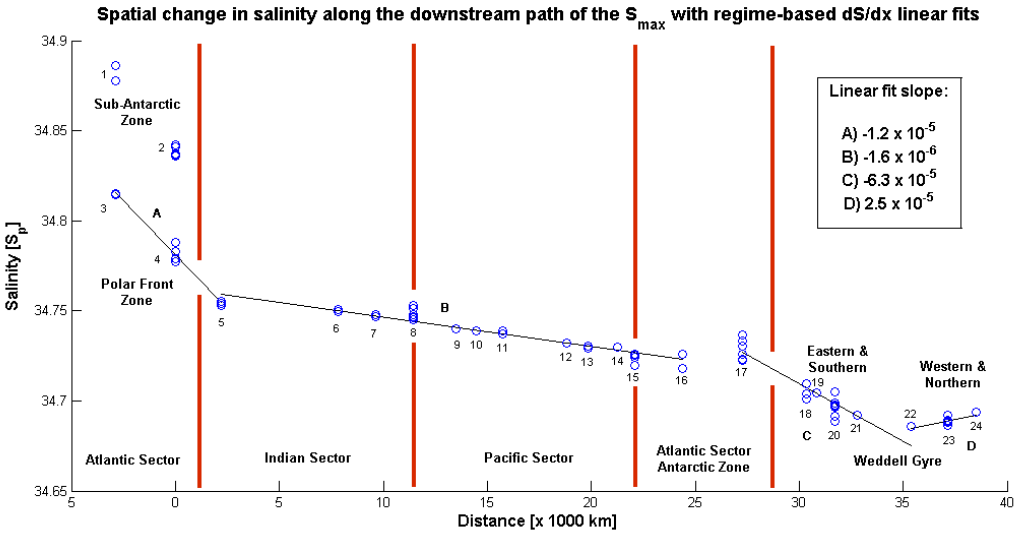

b)

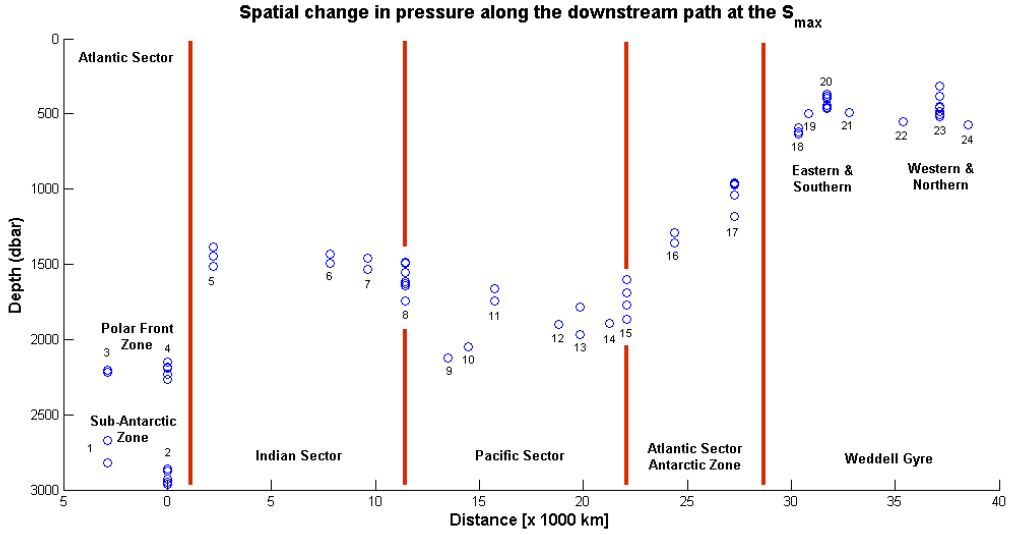

Figure 3.12 – Downstream spatial change of the salinity-maximum (as described in section 3.3.3), with distances referenced to the Greenwich Meridian. Red vertical lines and labels denote the different sectors of the Southern Ocean under consideration, with a distinction between two different zones of the northern Atlantic Sector and two different regimes in the Weddell Gyre. Numbers are in accordance with Table 3.1 referring to section groups as follows: 1) A23-SAZ, 2) SR02-SAZ, 3) A23-PFZ, 4) SR02-PFZ, 5) I06S, 6) I08S, 7) I09S, 8) SR03, 9) P14S, 10) P15S, 11) P16S, 12) P18, 13) P19S, 14) A21, 15) SR01, 16) A23-AZ, 17) SR02-AZ, 18) I06S-EWG, 19) 20E-SWG, 20) SR02-SWG, 21) A23-SWG, 22) A23-NWG, 23) SR02-NWG and 24) 20E-NWG.

a) Variation in the value of the salinity-maximum. The letters refer to the lines of best fit for the (A) Polar Front Zone; (B) Pacific/Indian/Atlantic western AZ Sectors; (C) Atlantic eastern AZ, Eastern & Southern Weddell Gyre; and (D) Western & Northern Weddell Gyre, with the slope of each fit shown inset.

b) Variation in the pressure/depth of the salinity-maximum.

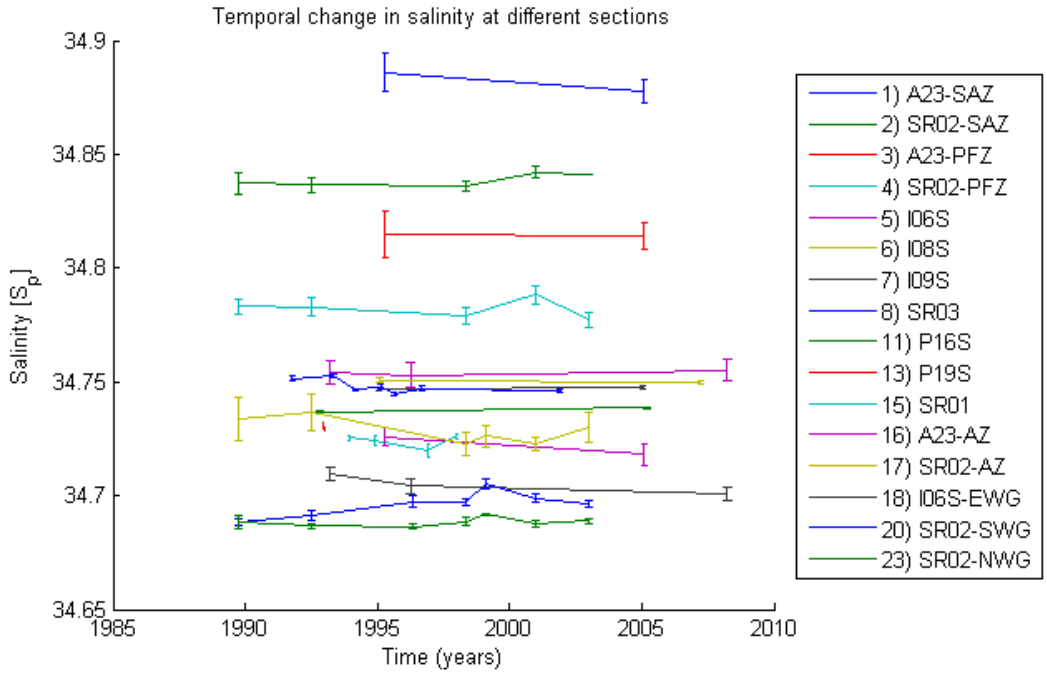

Figure 3.13 – Temporal distribution of the salinity maximum for each set of repeat occupations of a section group. The numbering and naming of section groups in the key is in accordance with Table 3.1 and Figure 3.12, omitting sections with only one available occupation. Error bars are the standard error of the mean of the maximum salinity values for each section occupation. The order of the line colours in the key is consistent with the order of the salinity distribution in the plot.

to a deeper level across the Amundsen, Bellingshausen and Mornington Abyssal Plains: here it is due to the lack of topographic constraint on AABW flowing northeast out of the Ross Sea resulting in a deeper and more saline bottom water signature. The salinity-maximum shallows towards 1000 m as it moves through Drake Passage and into the Antarctic Zone of the Atlantic sector. The signature finally shallows to ~500 m within the WDW representing the end of the shoaling of isopycnals associated with the LCDW.

The variability in the salinity-maximum signature between repeat occupations of a section is often only as large as the variability of the salinity-maximum (defined as standard error of the mean) between the stations of a single cruise. This is demonstrated in Figure 3.13 where the section mean of the salinity-maximum is plotted with bars of standard-error to demonstrate inter- and intra-section variability.

Overall, there appears to be no significant trend in the circumpolar salinity signature although small increases and decreases are observed:

- The SR02-SAZ (1) salinites are surprisingly stable considering that the data sampling for these regions are irregular, whilst there is actually greater variability within the SR02-PFZ (2) occupations which are more consistently surveyed. This suggests a relatively homogenous and quiescent SAZ and more variable and dynamic PFZ.
- The occupations of sections I06S (5) through to SR03 (8) show low variability between occupations of each section, and are collectively a consistently close grouping.
- The Pacific sector and Drake Passage sections (11-16) have a greater degree of variability compared to the previous group of sections, but still largely within the range of the associated error.
- The SR02-AZ (17) sections show the greatest variability, with values as high as the lowest P16S occupations and as low as the mid-range of the SR01 occupations. This suggests a variable cross-frontal influence from the PFZ, possibly the result of short-term impacts from eddy-activity.
- The smaller error bars and lower inter-section variability within the northern Weddell Gyre (23), compared to the more pronounced variability of the southern Weddell Gyre (20), suggests variability in the salinity-maximum signature may be mediated by local mixing processes in the western Weddell Gyre. The greater variability in the southern Weddell Gyre may be linked to known variability in volume transport into the region, as demonstrated by Cisewski et al. (2011) and in ***chapter 4***, associated with jets created by the topography of Maud Rise.
- The most profound statement which can truly be made about those sections with only two occupations (1, 3, 6, 7, 11, 13 and 16) is that the repeats are not unexpectedly different.

There are three main conclusions to be drawn from these results. Firstly, there is no observable temporal trend in the value of the salinity-maximum for the time period considered. Secondly, there are clear regimes of spatial change in the value of the salinity-maximum:

A. the Sub-Antarctic Zone/Polar Front in the Atlantic sector;

B. the Indian sector/Pacific sector/Drake Passage;

C. the Antarctic Zone of the Atlantic sector, and the eastern and southern Weddell Gyre;

D. the northern Weddell Gyre;

Thirdly, that the depth of the salinity maximum may vary during the circumpolar transit but it maintains a stable range of density, which is only modified by significant shifts from one regime to another.

3.4.3 Entrainment Estimates

Estimates of various entrainment ratios made using equations [1] and [2] are shown in Table 3.2 demonstrating how the NADW of the South Atlantic can only make a minimal direct contribution to the salinity signature of the Weddell Gyre. These values are now compared and contrasted to build up an understanding of cross-frontal mixing. Firstly, the PFZ of SR02 has a dominant 0.63 contribution from SR01 in Drake Passage when compared to the southward moving Sub-Antarctic Zone of A23 (0.37). Within the ACC, the Polar Front Zone at SR02 also has the highest contribution from the Polar Front Zone at A23 (0.65), rather than the Antarctic Zone at A23 (0.35).

Further south, the dominant contribution to the Antarctic Zone at SR02 is overwhelmingly – 0.93 – from the AZ at A23, with just a 0.07 contribution from the PFZ at A23. Comparisons to the more easterly I06S show the majority contribution is from the Antarctic Zone at both the A23 and SR02 sections, as opposed to the lesser contributions from the Polar Front Zone. Lastly the dominating 0.80 contribution from SR01 to I06S shows a relatively low entrainment of NADW into ACC from the Sub-Antarctic Zone (0.20). This information collectively suggests levels of cross-frontal mixing in the Atlantic Sector of the ACC that are insufficient to propagate NADW variability directly into the Weddell Gyre.

Source section 1 (S_{S1})	Ratio of Salinity contribution (C_{S1}:C_{S2})	Source section 2 (S_{S2})	Mixed section (S_M)
Entrainment into and across the ACC			
A23-SAZ	0.37 : 0.63	SR01	SR02-PFZ
A23-PFZ	0.65 : 0.35	A23-AZ	SR02-PFZ
A23-PFZ	0.07 : 0.93	A23-AZ	SR02-AZ
A23-PFZ	0.35 : 0.65	A23-AZ	I06S
SR02-PFZ	0.48 : 0.52	SR02-AZ	I06S
A23-SAZ	0.20 : 0.80	SR01	I06S
Entrainment into the Weddell Gyre			
A23-AZ	0.08 :0.92	A23-NWG	SR02-NWG
A23-AZ	0.30 : 0.70	A23-NWG	SR02-SWG
SR02-AZ	0.41 : 0.59	SR02-NWG	I06S-EWG
SR02-AZ	0.20 : 0.80	SR02-NWG	SR02-SWG
I06S-EWG	0.49 : 0.51	SR02-NWG	SR02-SWG

Table 3.2 - Entrainment estimates for contributions to the ACC (top dataset) and for contributions to the Weddell Gyre (bottom dataset). Values are decimal ratios of the source contributing sections to the mixed section. SAZ (Sub-Antarctic Zone), PFZ (Polar Front Zone), AZ (Antarctic Zone), NWG (Northern Weddell Gyre), SWG (Southern Weddell Gyre) and EWG (Eastern Weddell Gyre).

Additionally, the various estimates of entrainment into the Weddell Gyre from the ACC consistently show that existing WDW dominates the salinity signature of the gyre, reinforcing the idea of a mixing barrier existing between the ACC and the Weddell Gyre. The SR02 contributions to I06S-EWG, when compared to the contributions to the SR02-SWG, suggest that there is a significant entrainment of higher salinity LCDW/WDW from the eastern Weddell Gyre into the WDW from the northern Weddell Gyre. This is confirmed by comparing the I06S-EWG contribution (0.49) to the SR02-NWG contribution (0.51). In particular, this highlights the eddy dominated eastern Weddell Gyre as the primary source of entrainment of CDW into the gyre from the ACC.

3.4.4 *Mixing Coefficients*

With reference to Equation [7], whilst all stations provided a consistently negative $\frac{\partial^2 S}{\partial z^2}$ term, the $\frac{\partial^2 S}{\partial j^2}$ term was not consistently negative across all sections. Due to the near-linear profile of the salinity-maximum across the Polar Front and Antarctic Zones of the Atlantic sector, the $\frac{\partial^2 S}{\partial j^2}$ term either varies between being positive or negative or could be interpreted to be zero. I06S was similarly affected by the continuation of the deep salinity-maximum beneath the Agulhas Retroflection.

Additionally, I08S was affected by the presence of the Kerguelen Plateau which results in a bimodal peak in the salinity-maximum to the north and south of the plateau, with an intervening low salinity-maximum associated with the deep Australian-Antarctic Gyre (McCartney and Donohue 2007). The shallow bathymetry forces LCDW to be transported around the north and south of the plateau, as reflected in the diversion of the ACC fronts in Figure 3.8. The effect of this deep gyre can also be seen in the profile of one of the two occupations of I09S, suggesting it has a variable zonal impact.

	#	κ_V ($m^2\ s^{-1}$)	κ_I ($m^2\ s^{-1}$)
SR03 and Pacific sector	15	$2.86 \times 10^{-4} \pm 1.91 \times 10^{-4}$	$8.97 \times 10^{2} \pm 2.13 \times 10^{2}$
Eastern and southern Weddell Gyre	12	$2.39 \times 10^{-5} \pm 0.73 \times 10^{-5}$	$2.47 \times 10^{2} \pm 0.27 \times 10^{2}$
All of above combined	27	$2.86 \times 10^{-5} \pm 1.50 \times 10^{-5}$	$2.62 \times 10^{2} \pm 0.35 \times 10^{2}$

Table 3.3 – Results of 3 multiple linear regression calculations based on a given number of section realisations (#) providing estimates of the vertical mixing coefficient (κ_V) and isopycnal mixing coefficient (κ_I).

Finally, in the northern Weddell Gyre the term varies between positive or negative values due to the influence of the mixing with the Antarctic Zone to the north and with the southern Weddell Gyre. This also makes the $\frac{\partial S}{\partial i}$ term positive.

It was therefore only possible to calculate mixing coefficients for the SR03 and Pacific sector sections and the sections covering the eastern and southern Weddell Gyre as shown in Table 3.3. Within the ACC – from the SR03 sections to the A21 section – a vertical mixing coefficient is obtained of $\kappa_V = 2.86 \times 10^{-4}$ m^2 s^{-1} and an isopycnic mixing coefficient of $\kappa_I = 8.97 \times 10^2$ m^2 s^{-1}. Each has errors of the same order of magnitude, but numerically smaller.

In the eastern and southern Weddell Gyre the vertical mixing coefficient is an order of magnitude smaller, at $\kappa_V = 2.39 \times 10^{-5}$ m^2 s^{-1}: likely due to the generally less rough underlying topography when compared to that below the ACC. The isopycnal coefficient is the same order of magnitude as for the ACC, at $\kappa_I = 2.47 \times 10^2$ m^2 s^{-1}. Both have an associated error an order of magnitude smaller.

The combined calculation places the vertical mixing coefficient at $\kappa_V = 2.86 \times 10^{-5}$ m^2 s^{-1} with an error the same order of magnitude but numerically smaller. The isopycnal mixing coefficient remains at the same order of magnitude, at $\kappa_I = 2.62 \times 10^2$ m^2 s^{-1}, with the associated error an order of magnitude smaller. As the combined calculation produces coefficients which are similar to the eastern and southern Weddell Gyre coefficients, and the SR03 and Pacific sections have a much larger associated error, this suggests that there is greater variability in the vertical mixing rates in the Pacific sector than in the Weddell Gyre, with some regions of the Pacific being more quiescent than others. This is consistent with known variations in underlying bathymetry across the Pacific sector of the Southern Ocean.

Collectively, these values suggest it is best to consider the two regimes independently especially when considering the underlying bathymetry. In general the Weddell-Enderby Basin is bathymetrically smooth, with the exception of major features such as Maud Rise, whereas the SR03 and Pacific sector sections cross rough and complex bathymetry, particularly in south of Australia and New Zealand and across the Pacific Antarctic Ridge. However, the relatively large κ_V error for the SR03 and Pacific sector is likely the result of the ACC crossing the Amundsen, Bellingshausen and

Mornington Abyssal plains in the eastern Pacific sector which are devoid of any significant bathymetric features compared to those areas further west.

3.5 Discussion

3.5.1 Variability and Stability in the Southern Ocean

Circumpolar trends

The quantitative observations made in this study about the circumpolar freshening trend of the salinity-maximum downstream from the NADW source is consistent with the brief circumpolar part of the study by Williams et al. (2006) and reinforces the earlier observations of Callahan (1972) regarding the distribution of deep water masses. Within Drake Passage, Williams et al. (2006) identify no clear trend in the core thermohaline properties of the LCDW across the entire study period between 1926 and 2004, whilst our study seems to confirm their initial assessment that there is no apparent temporal trend across the rest of the Southern Ocean either. This does not preclude a long-term trend from existing in the Southern Ocean wide deep salinity-maximum; however there is an insufficiently large hydrographic dataset at this time to judge circumpolar inter-decadal changes.

Observations of the repeatedly occupied SR1b section (referred to as SR01 in this study) in Drake Passage documented by Cunningham et al. (2003) show that the ACC has a remarkably steady volume transport over decadal timescales. However the exact position of the Polar Front and distribution of properties within Drake Passage are subject to rapid variation and therefore the small range of the mean salinity-maximum ($34.7196 < S_P < 34.7261$) in Drake Passage is to be expected owing to the meandering of fronts. This short-term variability was highlighted by Sudre et al. (2011) from the double occupation of a section in Drake Passage within 3 weeks, thus variability between any repeat sections should be expected over any timescale regardless of any long-term trends.

An earlier study by Bryden and Pillsbury (1977) using moorings at a depth of 2700m showed an overwhelmingly down-channel flow with a root mean square speed of ~ 2 cms^{-1} which is consistent with the ECCO estimates obtained for this study of ~ 4 cms^{-1} at a shallower mean LCDW depth of 1730m. Their study also showed an occasional reversal of flow lending credence to the short timescale redistribution of properties along isopycnals.

Observations of warming in the Southern Ocean suggest thermohaline changes are or were taking place. A prominent example is the 0.17 K warming between 1950 and 1980 at depths of 700-1100 m as detected by Gille (2002) and thought to be linked to the annually ventilated mode waters forced by atmospheric warming. As LCDW is predominantly deeper than this, it is entirely feasible that this temperature increase does not apply to the deeper ocean, as supported by the results of Williams et al. (2006).

The ACC in general is known to exhibit variability in flow regimes, transport and frontal positions. According to Turner and Overland (2009), certain parts of the Southern Ocean have changed rapidly in the last century, but there is a complex pattern of change, with multiple mechanisms and feedbacks implicated in the variability of the oceans characteristics. For instance, the variability of LCDW water mass characteristics could be accounted for by: an acceleration in the ACC effecting entrainment of source water masses; the southward shift of the ACC and its fronts as a result of changes to the Southern Annular Mode (SAM); or greater eddy activity resulting from increased westerly winds. Such variability could account for the small changes between repeat occupations.

Focus on the Weddell Gyre variability

Decadal scale variations in the characteristics of the Weddell Gyre have been observed across the Greenwich Meridian with the mean salinity of the WDW observed to vary between 34.677 and 34.681 by Fahrbach et al. (2004), although the variation is within the magnitude of the error. In agreement with the assessment of this study, they judge that minor variations are likely to be real. Interestingly, Whitworth and Nowlin (1987) note persistent subtle signals, such as a mid-depth silicate maximum which they identify as being sourced from the Indian Ocean. This suggests that despite mixing over long distances in the circumpolar path and across dynamic regime boundaries, variations in deep water mass properties can be conserved and have an observable presence in the Weddell Gyre, albeit as a weaker signal.

Such observed variability may be due to time-varying transports across the topographically restricted southern Weddell Gyre. Cisewski et al. (2011) calculate a westward transport of 23.9 ± 19.9 Sv in austral summer and 93.6 ± 20.1 Sv in austral winter from two separate cruises. This large variability in volume transport was thought to be linked to gyre-scale forcing by changes in the wind stress curl and manifests itself primarily in variations in the jet structures associated with the Maud Rise seamount and the Antarctic continental slope. Thus changes in transport could lead to a pulsating propagation of salinity signals from east to west.

The likely downstream impact of such variability is assessed by Robertson et al. (2002) as being the origin of variability across the southern and western Weddell Gyre, with their temperature-maximum trend matching our observed salinity-maximum trend. They suggest that internal processes should dampen the variability of inflow waters, but it is unclear whether they consider the inflow water variability to arise from the described characteristics about Maud Rise or to variations in LCDW entrainment. Fahrbach et al. (2011) present a supporting analysis of data over 24 years leading to the proposal that the Weddell Gyre acts as a heat buffer, with the WDW characteristics dominated by decadal scale variations induced by variability of inflowing CDW at the boundary. They also note the role of Maud Rise and atmospheric forcing and describe how changes to the circulation of the Weddell Gyre will not change overall heat/salt content, but would act to increase/decrease homogenisation depending on the conditions.

However, Fahrbach et al. (2006) – in response to Smedsrud (2005) – note that disentangling internal and external forcing is difficult as integrated properties in particular are subject to significant change due to mixing with overlying and underlying water masses. This justifies our approach at looking at the maximum-salinity as a key indicator of variability. The presence of Maud Rise on the Greenwich Meridian is a complicating factor as the topographic effects could have significant impact on the observations obtained along the Greenwich Meridian, without actually having a long-term impact on gyre-scale properties.

Another potential source of variability observed across the Greenwich Meridian is the potential for a transient two-cell structure as hypothesised by Fahrbach et al. (2004) and modelled by Beckmann et al. (1999). Transition between a single cell and two-cell structure would give rise to variations in the modification of the salinity signal within the Weddell Gyre, as well as affect the entrainment of LCDW, however our study does not offer evidence in support of this theory.

3.5.2 The exchange of water masses

Whilst at first consideration the entrainment calculations appear to be a rather simple technique, it nevertheless appears to offer a robust insight into deep water mass dynamics and supports the existing evidence regarding NADW and LCDW entrainment. Underlying the transport of the ACC are the strong zonal fronts, which according to Sokolov and Rintoul (2009a, 2009b) comprise numerous branches of the conventional ACC fronts associated with sea surface height gradients. However, whilst their analysis accounts for ~90% of the variability, the remaining variability speaks to the fact that these fronts are not always strong or continuous in time and space. This owes to the propagation of eddies across these fronts which drives entrainment from one regime to another. Paraphrasing Naveira Garabato et al. (2011), under these conditions the parallel jets lead to homogenisation of water masses between fronts, however in regions of greatest eddy transport and mixing, these fronts are 'leaky' and thus provide for cross-frontal exchange of water masses exceeding that which normally occurs along the path of the ACC.

On the topic of topographic steering of the ACC flow, Gille (2003a, 2003b) lends credence to this leaky front position, linking the coincidence of frontal positions and topographic features to the meandering of the fronts downstream of topography and resulting in enhanced eddy fluxes. Earlier work by Moore et al. (1999) provides an explanation for this phenomenon related to the variability of the PF. Over deep bathymetry the surface expression of the PF is weakened due to fields of quasi-constant planetary potential vorticity (PPV), whereas near shallow bathymetric features the PPV gradients are large, the PF is intensified and meandering is inhibited. In the lee of topography the intense fronts lead to greater meandering as the topographic control breaks down, producing increased

eddy formation and therefore greater cross-frontal transport. This lends support for Deacon (1979) regarding the position of the PF being related to the upwelling of CDW due to topographic barriers. As the sloping of isopycnals and the related ACC transport result from wind forcing and the hydrographic conditions, the surface expression of the ACC fronts are dynamic and regionally varying according to the underlying topography.

This concept is further reinforced by the work of Venables et al. (2007), Sallée et al. (2011), and Thompson and Sallée (2012) which examines along-stream property changes related to topographic features. High-levels of cross-stream particle movement are observed in the lee of major and moderate topography. This seems to hold with the pattern of the dominant entrainment of NADW into the ACC in the Argentine Basin and the entrainment of LCDW into the eastern Weddell Gyre in a region southeast of the Southwest Indian Ridge. Other regions of significant topography are notable such as at ~170^{o}E, however here any cross-frontal exchange that occurs would be difficult to observe due to the homogenous LCDW signature across the ACC in the eastern Indian and Pacific sectors of the Southern Ocean.

Reasons for entrainment/isolation of NADW into PFZ

The complex topography which results in the northward excursion of the ACC fronts into the Argentine Basin is the prime means by which NADW is entrained into the ACC. The meandering of the fronts and the associated eddy activity allow a higher cross-frontal transfer of water mass properties than along the rest of the SAF in the Atlantic sector. The importance of the Argentine basin in mixing has been previously noted (e.g. Peterson and Whitworth 1989, Arhan et al. 1999). The topographically driven mechanisms for the movement of these fronts within the Scotia Sea are well described by Naveira Garabato et al. (2002a).

Of less importance seems to be the more easterly sections of the SAF, and surprisingly the Agulhas Retroflection, despite carrying a deep salinity-maximum beneath it appears to make a low contribution based on entrainment estimates. This is likely due to this feature contributing directly to

the deep waters of Indian Ocean rather than being carried east by the ACC. We therefore conclude that the southwest Atlantic is the most important region for the entrainment of NADW.

Reasons for entrainment/isolation of WG

A number of authors have identified the eastern Weddell Gyre as a region dominated by eddy activity which is thought to contribute significantly to the entrainment of CDW (e.g. Deacon 1979, Orsi et al. 1993, Orsi et al. 1995, Gouretski and Danilov 1993). Gouretski and Danilov (1994) describe the impact of warm core eddies from the ACC moving south into the eastern Weddell Gyre and observed that they must lead to the transport of heat and salt as the eddies decay. Whilst the ACC is in an eddy-saturated state, there are regions of greater and lesser eddy activity.

Fahrbach et al. (1994) assert that the injection of LCDW can occur through the Weddell Front (the local Southern Boundary of the ACC generated by the influence of the Antarctic Peninsula) and thus cross frontal entrainment of LCDW can potentially occur west of the Greenwich Meridian. However, as the front is variable in intensity, injection of water masses into the northern Weddell Gyre must also be subject to variability. This factor is considered less important than the eastern Weddell Gyre region, and they assert that processes local to the gyre, either open-ocean or coastal, are likely to play a major controlling factor on the salinity signal of the WDW.

Garabato et al. (2004) identify that turbulent mixing is enhanced over topography and this plays a crucial role in closing the overturning circulation. A particular section of interest in this study is the 20E-NWG section in the north-eastern Weddell Gyre. The dynamic height contour we use to denote the Southern Boundary of the ACC is present only in the extreme north of the section at ~53.5^{o}S. The Southwest Indian Ridge underlies the front at this latitude and deepens further east, through which the ACC deflects southwards. Rough topography and a meandering ACC provide ideal conditions for turbulent mixing to act to modify the LCDW and entrain it into the eastern Weddell Gyre.

The estimate of LCDW entrainment to the WDW from the SR02 section at the Antarctic Zone to the SR02 section at the southern Weddell Gyre of 0.20 seems reasonable when considered alongside the total transport of the gyre. Whilst Weddell Gyre transport estimates vary, a transport of ~60 Sv across a double-cell structure for the Weddell Gyre at the Greenwich Meridian proposed by Beckmann et al. (1999) is a reasonable baseline, supported as it is by measurements across the Greenwich Meridian by Schröder and Fahrbach (1999) of 60 ± 10 Sv. As a significant bulk of the water mass in the Weddell Gyre is WDW, down to a depth of ~1000-1500 m, a significant bulk of the transport also lies within the WDW. This provides a potential of ~12 Sv of LCDW entrainment into the gyre based on the Weddell Gyre transport estimate of Beckmann et al. (1999). Garabato et al. (2003) estimates from a box-inverse model that ~9.7 Sv of AABW (WSBW and WSDW) are exported from the Weddell Gyre, which is comparable to our entraining LCDW estimate. Whilst the manner in which AABW forms is not as simple as a direct conversion of WDW to bottom water, there should be a balance between the incoming source water and out flowing AABW and AAIW components. This estimate gives reassurance to our bulk entrainment estimate.

Water Mass Summary

The frontal meridional barrier presented by the ACC outweighs the poleward transport of properties by eddies ensuring the downstream propagation of the deep salinity-maximum signature in the ACC dominates the deep pathway of the MOC. Meredith and Hogg (2006) describe how the eddy activity of the Southern Ocean changes with variations in the Southern Annual Mode (SAM) atmospheric index. During periods of strong winds the stress induces changes in intensity of the eddy field without accelerating the ACC transport as the system is in a state of eddy saturation. Instead, with increased winds, the eddy field increases in activity leading to increased cross-frontal transport of hydrographic properties, and the decreased insulation of the WG from direct contributions from NADW.

This view of the Southern Ocean circulation is reflected by the particle exchange experiments of DööS (1995) which contrasts various pathways of inter-basin exchange. Our study deals with the

indirect ventilated route of particles moving through the Southern Ocean, and subsequently upwelling south of the ACC. This route has a mean of six repeat circulations of Antarctica before exposure to the surface ocean, and this number is consistent with our estimated entrainment values which indicate 80% of the LCDW passing through Drake Passage continues through to I06S. This route is as opposed to the direct unventilated route whereby water moves from basin to basin without reaching the surface, such as the movement of CDW directly into the Pacific and Indian Oceans.

The indirect ventilated route described by Döös (1995) is essentially the upper overturning circulation branch of the MOC in the Southern Ocean as described by Marshall and Radko (2006), with the added twist that UCDW is simultaneously being advected around Antarctica. Whilst the former study is representative of the UCDW, the LCDW is subject to a similar dynamical regime and thus the particle experiment is still valid.

The entrainment estimates combined with these considerations suggest that the frontal system acts as a meridional barrier to the propagation of NADW properties, insulating the Weddell Gyre from fluctuations in the large-scale circulation, and thus negating a direct meridional pathway across the ACC for the MOC. From this we can surmise that the ACC system must act to mitigate the effect of climatic anomalies upon the high latitude Southern Ocean from latitudes north of the ACC.

3.5.3 Estimating Mixing Rates

The estimates of $\kappa_V = (2.39 \pm 0.73) \times 10^{-5}$ $m^2 s^{-1}$ for vertical mixing in the Weddell Gyre and $\kappa_V = (2.86 \pm 1.91) \times 10^{-4}$ $m^2 s^{-1}$ for the eastern Indian and Pacific sectors of the ACC are consistent with a range of other estimates for the world's oceans and the Southern Ocean in particular. Munk (1966) estimated a bulk κ_V of 1.3×10^{-4} m^2 s^{-1} for the Pacific interior which is lower than our ACC estimate and higher than our Weddell Gyre estimate. As rates vary with depth and topographic roughness this is understandable. An earlier estimate for horizontal mixing by Munk (1950) required $\kappa_H = 5 \times 10^3$ m^2 s^{-1} in order to obtain a realistic scale for the western boundary current of a wind driven gyre, over three times larger than our largest estimate of $\kappa_I = 8.97 \times 10^2$ $m^2 s^{-1}$.

An examination of the Brazil Basin by Polzin et al. (1997) demonstrates the spatial variability of mixing in the abyssal ocean, with $\kappa_D = 0.1 \times 10^{-4}$ m^2 s^{-1} over smooth topography, similar to this study's Weddell Gyre estimate under similarly low energy conditions. They obtain a higher estimate 5×10^{-4} m^2 s^{-1} within 150m of sea floor and over rougher topography, twice as large as our mid-depth estimate for the LCDW in the ACC.

Naveira Garabato et al. (2004) obtained a range of estimates for weakly stratified Nordic Seas, however at mid depths of 1500-2500m, $\kappa_V \approx 10^{-4}$ to 10^{-3} m^2 s^{-1} was dominant. Garabato et al. (2004) likewise obtained a range of mixing rates, with higher rates above rough topography of 10^{-4} m^2 s^{-1} at 500m to 10^{-3} to 10^{-2} m^2 s^{-1} near the sea floor at the bottom of Drake Passage. The lower estimate is consistent with our ACC estimate which tracks topography during its circumpolar path. Zika et al. (2009) obtain an isopycnal mixing rate of $\kappa_I = 300 \pm 150$ m^2 s^{-1} and diapycnal mixing rate of $\kappa_{D=} (1 \pm 0.5) \times 10^{-4}$ m^2 s^{-1} for the entire Southern Ocean, which are both broadly in agreement with this study's results.

In the Indian Ocean Sloyan (2006) calculates an abyssal diapycnal mixing rate, $\kappa_D = 13\text{-}15 \times 10^{-4}$ m^2 s^{-1} for the LCDW moving northward into the Perth Basin which is higher by a factor of 3 compared to our highest estimate. Likewise Heywood et al. (2002) provide evidence for enhanced mixing over topography with $\kappa_D = (39 \pm 10) \times 10^{-4}$ m^2 s^{-1} therefore also an order of magnitude larger than our estimate for the ACC. Both these studies do however focus on topographically constrained regions whereas the open ACC sits astride topographic obstacles and may provide a less turbulent regime.

Estimates for mixing in a mesoscale eddy include Cisewski et al.(2005, 2008) $K_V = 7 \times 10^{-4}\text{-}10^{-3}$ m^2 s^{-1} in the upper pycnocline in the ACC at ~20^{o}E. Hibbert et al. (2009) estimate a maximum $K_V = 3 \times 10^{-4}$ m^2 s^{-1} for a cold core eddy which is well within our own ACC estimate despite the different focus. They also estimate a $K_H = 30\text{-}100$ m^2 s^{-1} which is in good agreement with our own estimates of isopycnal mixing, $\kappa_i = (2.47\text{-}8.97) \times 10^2$ m^{2}s^{-2}. Leach et al. (2011) examined lateral mixing of the WDW entering the Weddell Sea and found an isopycnic diffusivity of 70-140 m^2 s^{-1} and

diapycnic diffusivity of 3×10^{-6} m^2 s^{-1}. The former is in general agreement with our own estimates, although the latter is an order of magnitude smaller than our Weddell Gyre estimates.

A more recent study by Ledwell et al. (2010) diagnosed a diapycnal diffusivity $\kappa_D = (1.3 \pm 0.2) \times 10^{-5}$ m^2 s^{-1} in the eastern Pacific sector of the ACC averaged over 1 year and thousands of kilometres: a value which is characteristic of the mid-latitude ocean interior. Given the less rough topography of the region this value fits well with our estimate for the relatively quiescent Weddell Gyre, and not our ACC estimate. However, as expected, higher values would be expected to the west of our Indian-Pacific region which lies over far more complex and shallower topography. This supports the notion that the background diapycnal mixing is too weak to support the MOC at mid-depth and must be offset by more intense mixing in sites generating turbulence.

With this range of studies and values for comparison, the estimates of isopycnal and vertical diffusivity derived in this study fit well into the understanding of oceanic mixing. Quiescent ocean environments with lower flow speeds and deeper, smoother bathymetry experience lower mixing rates due to the less turbulent and lower energy environment: such as the Weddell Gyre in the Weddell-Enderby Basin. Conversely, more dynamic ocean environments experiencing higher flow speeds over shallower, rougher bathymetry experience higher mixing rates due to greater turbulence and higher energy environment: such as the ACC which follows the mid-ocean ridges. Mixing is known to vary on fine time and spatial scales, however the approach taken in this study provides a bulk basin-scale estimate which is consistent with both other large-scale studies and the value of $\kappa_v = 5 \times 10^{-5}$ m^2 s^{-1} used in chapter 2 to demonstrate the circumpolar process which entrains LCDW into the Weddell Gyre. Indeed this value is between the lower estimate of $\kappa_V = (2.39 \pm 0.73) \times 10^{-5}$ $m^2 s^{-1}$ for vertical mixing in the Weddell Gyre and higher $\kappa_V = (2.86 \pm 1.91) \times 10^{-4}$ $m^2 s^{-1}$ for the eastern Indian and Pacific sectors of the ACC.

This is indicative of a system whereby the LCDW, which is repeatedly circumnavigating Antarctica in the ACC, is being vigorously mixed and thus the thermohaline signature of the NADW entraining into ACC in the Atlantic sector can be diluted through mixing before that signature reaches

higher latitudes. Whereas the weaker mixing in the Weddell Gyre more slowly moderates the characteristics of the WDW, suggesting thermohaline anomalies which penetrate into the gyre are less quickly diluted. Together this suggests that the ACC has a leading order control over the propagation of NADW thermohaline variability into the climatically sensitive regions of sea-ice formation in the south and southwestern Weddell Sea.

3.6 Conclusion

Building upon the work of Williams et al. (2006) this study quantifies the spatial trend of the deep salinity-maximum within the Southern Ocean. This is conducted within a framework of variable density regimes to the north of, within and to the south of the ACC owing to water mass modification during the process of entrainment from one regime to another. There is no observable temporal trend from the repeat occupations of sections; however there is a clear spatial trend in the salinity signature.

This signature originates from the NADW formed in the North Atlantic which is transported southwards and is subsequently entrained into the ACC as CDW. The salinity signature freshens as it is carried through the Indian and Pacific sectors of the Southern Ocean due to mixing with the intermediate and bottom water masses above and below, respectively. The signature is transported through Drake Passage and the Scotia Sea, after which it remixes to some extent with NADW in the Polar Front Zone of the ACC causing a temporary increase in salinity. The signature continues to freshen across the Greenwich Meridian and into the eastern and southern Weddell Gyre, before lateral mixing causes an increase in the northern Weddell Gyre. This spiralling trend suggests that the ACC insulates the Weddell Gyre from short-term fluctuations in the characteristics of NADW in the South Atlantic.

This assertion is supported by estimates of entrainment which indicate low-levels of cross-frontal mixing, particularly within the western Atlantic sector. The entrainment estimates also suggest that there are varying degrees of entrainment from the ACC into the Weddell Gyre at all of the observed longitudes in the Atlantic sector, but that the greatest entrainment occurs within the eastern limb of the Weddell Gyre.

Estimates of vertical and isopycnal mixing coefficients are in line with other estimates for the Southern Ocean, although they are only valid for the Indian and Pacific sectors, and the eastern and southern Weddell Gyre. Two separate estimates for these two regional sets produce differences which make sense: the ACC has higher mean transport velocities and flows over rougher topography than

the slower moving Weddell Gyre, corresponding to higher and lower rates of vertical mixing, respectively.

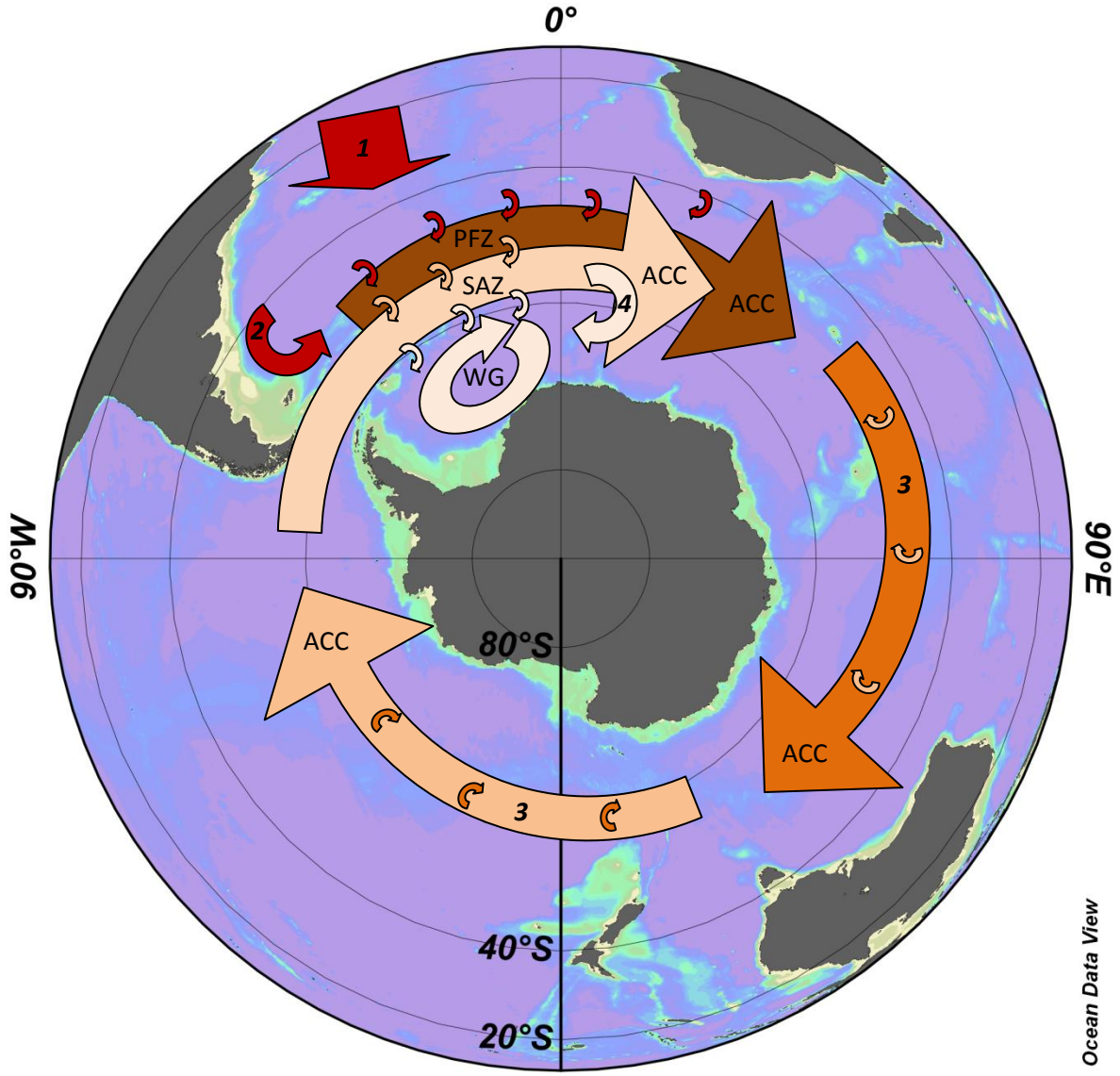

Figure 3.14 – Schematic of the propagation of the deep salinity-maximum through the Southern Ocean. NADW flows southwards into the South Atlantic [1] and is entrained into the Polar Front Zone (PFZ) of the Antarctic Circumpolar Front (ACC) in the Argentine Basin [2] as Lower Circumpolar Deep Water (LCDW). LCDW is advected eastwards by the ACC, with limited cross-frontal mixing with the Antarctic Zone (AZ) in the Atlantic sector. LCDW passes through the Pacific and Indian sectors [3], during which a gradual flux of salinity carried pole ward by eddies crosses the zonal fronts. The recirculating LCDW meets the entraining NADW east of Drake Passage in the north of the ACC, whilst the LCDW is slowly entrained into the northern limb of the Weddell Gyre to the south of the ACC [4]. The dominant entrainment of LCDW occurs in the eastern limb of the Weddell Gyre, where it is modified to Warm Deep Water (WDW) and repeatedly recirculated within the gyre until local water mass modification exports the WDW as Antarctic Intermediate Water or Antarctic Bottom Water.

It is proposed that the ACC in the Atlantic sector acts as a long-term 'oceanic blender', mediating the impact of variability in the global overturning circulation upon the high latitude Southern Ocean as summarised in Figure 3.14. This, along with observed variability within the Weddell Gyre, suggests that local processes – such as the wind-induced baroclinic control of gyre transport proposed by Jullion et al. (2010) – dominate changes to the characteristics of the WDW and may therefore be more significant on short timescales with respect to the formation of Antarctic Bottom Water. Long-term changes to the characteristics of the southward moving NADW would however eventually propagate to the Weddell Gyre, but this is a useful insight into the Southern Ocean's role in the climate system.

3.7 Special Acknowledgements

Our thanks go to the scientists and crews of the various cruises whose data we have used, and to the CLIVAR and Carbon Hydrographic Data Office for hosting the publicly available data.

The state estimates were provided by the ECCO Consortium for Estimating the Circulation and Climate of the Ocean funded by the National Oceanographic Partnership Program (NOPP).

This work has been greatly improved by the contributions of two anonymous reviewers.

Chapter 4

The Weddell Gateway: An Inverse Approach to Determining Volume Transport in the Lazarev Sea

4.0 Abstract

The four cruises of the Lazarev Sea Krill Study (LaKriS) undertaken during different seasons between 2004 and 2008 provide a rare set of semi-repeat gridded hydrographic data. The Inverse Multi-Box Adaptable Model (IMBAM) has been developed to diagnose the volume transport of such datasets. Using CTD data to formulate mass conservation and Margules equations, and vessel mounted ADCP data as a velocity reference, total transport is compared for a range of different model set-ups.

Variability is observed in both the total transport and the transport of different water masses in the Lazarev Sea from cruise to cruise. Whilst jet structures associated with the northern flank of the continental slope and the seamount Maud Rise are consistently observed in the solutions, there are large deviations of the lateral pattern of flow. This ranges from the dominance of zonal flow through to large southward meanders to the west of Maud Rise, as well as intermediate conditions.

The transport across the Lazarev Sea is dominated by the deep water flow (89-99%); however the total Antarctic Surface Water transport can be incongruous with this deeper flow when the mixed layer is deeper during winter. There is therefore a need to make use of the full range of ADCP reference layers to account for vertical changes in the flow field. A maximum transport of 107 Sv and 118 Sv are obtained across the 3°E section of the *ANT-XXIII/2* and *ANT-XXIII/6* cruises, respectively. These estimates are credible but raise interesting questions regarding the interpretation of hydrographic variability across this gateway to the Weddell Sea.

As the primary source water mass for the entire water column, variability of the transport of the Warm Deep Water directly impacts the transport of heat into the Weddell Sea, and therefore has the potential to effect water mass modification processes and the formation of Antarctic sea ice.

4.1 Introduction

The Weddell Gyre is a major cyclonic circulation feature of the Southern Ocean incorporating the broad scale circulation of the Weddell-Enderby Basin found south of the Antarctic Circumpolar Current (ACC). It is a region of climatic significance where inflowing warm and saline deep waters undergo water mass modification processes which ultimately drive the northward flowing intermediate and deep components of the global overturning circulation (Fahrbach et al. 1994).

The Lazarev Sea is a marginal sea of the Southern Ocean notable for the significant bathymetric features of the Maud Rise seamount (1098 m minimum depth) and Astrid Ridge extending from the Antarctic continent (Figure 4.1.15). Maud Rise in particular is known to have a significant impact on the flow of the Weddell Gyre and the characteristics of the water column (Bersch et al. 1992, Gordon and Huber 1995, de Steur et al. 2007), and thus affects the transport of heat and salt into the western Weddell Gyre where the broad continental shelf provides a significant formation area for deep and bottom waters (Gordon et al. 1993). To the west of this topography lies the Weddell Abyssal Plain and to the east the Enderby Abyssal Plain making the features of the Lazarev Sea a prominent bathymetric obstacle to the transport of the Weddell Gyre. Although the Lazarev Sea strictly extends only from the Greenwich Meridian to 14^{o}E, the four cruises of the Lazarev Sea Krill Study (LaKriS) variably surveyed a region extending from 6^{o}W to 3^{o}E between 2004 and 2008.

As part of the international Southern Ocean Global Ocean Ecosystems Dynamics (SO-GLOBEC) program, LAKRIS aimed (1) to quantify seasonal population dynamics and physiological condition of krill (Euphausia superba), a key species in the Southern Ocean food web and (2) to identify relationships between the physical environment and the abundance of zooplankton and especially krill (Meyer et al. 2009, Brandt et al. 2011, Flores et al. 2011, Pakhomov et al. 2011, Flores et al. 2012). However it also provided a unique set of high-density hydrographic measurements in this important gateway region. Two studies have already made use of some of the LaKriS data to specifically examine estimates of the transport (Cisewski et al. 2011) and lateral mixing (Leach et al. 2011). However, the full dataset has not been used in a comparative study despite the rarity of such

data in the Southern Ocean. In order to improve the examination of this hydrographic data, this study makes use of inverse methodology to develop the 3-dimensional box-model suited to the grids of CTD data provided by the LaKriS campaign.

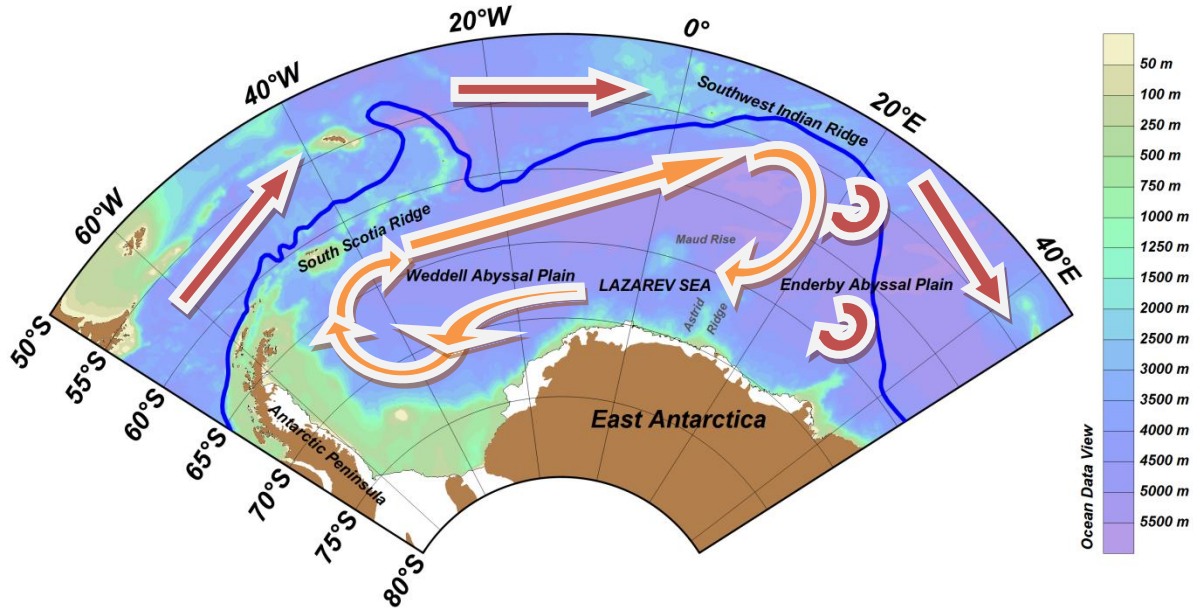

Figure 4.1.15 – Bathymetric chart of the Weddell-Enderby Basin with the Lazarev Sea region marked near the Greenwich Meridian. The Southern Boundary of the ACC (blue) from Orsi et al. (1995) is shown to indicate the northern extent of the Weddell Gyre. Straight red arrows indicate the direction of the ACC, curled red arrows indicate the entrainment of LCDW into the eastern Weddell Gyre, and orange arrows indicate the circulation of the Weddell Gyre.

As shown in Figure 4.1.15, the Weddell Gyre is bounded to the south and west by the Antarctic continent, to the northwest by the South Scotia Ridge and the ACC, to the northeast by the deeper topography of the Southwest Indian Ridge and the ACC, and to the east by the southward deflection of the ACC (Orsi et al. 1995). The extreme – although variable in position – northern and eastern limits of the Weddell Gyre are demarcated by the southernmost front of the ACC: the Southern Boundary. The transition from the ACC to the Weddell Gyre is complicated by the Weddell-Scotia Confluence arising from the interaction of Weddell Gyre water masses with ACC water masses from the tip of the Antarctic Peninsula eastwards through the southern Scotia Sea and beyond (Patterson and Sievers 1980, Heywood et al. 2004). The Southern Boundary is most pronounced in the lee of the Antarctic Peninsula, and becomes less pronounced in the eastern Weddell Gyre where the eddy field dominates the mean current (Gouretski and Danilov 1993).

Along the Greenwich Meridian the Weddell Gyre has a distinct eastward flowing northern limb and a westward flowing southern limb, although various studies have shown inter-annual variability in the hydrographic conditions and inferred volume transport (e.g.Fahrbach et al. 2004, Klatt et al. 2005, Fahrbach et al. 2011). At this longitude the central axis of the Weddell Gyre is located at ~60^{o}S with the bulk of the southern limb transport being formed by jet structures associated with the steep bathymetry of the Maud Rise seamount and Antarctic continental slope (Cisewski et al. 2011). The strength of the Weddell Gyre is thought to be largely controlled by atmospheric forcing leading to the doming of isopycnals (Beckmann et al. 1999, Wang and Meredith 2008, Jullion et al. 2010) where the variation closely corresponds with the area average wind stress curl leading to a minimum transport in January and a maximum in July. Maud Rise is known to periodically shed cyclonic and anticyclonic eddies into the mean current (Bersch et al. 1992, de Steur et al. 2007) which cut off isolated patches of WDW from the main body to the east of Maud Rise, moving southward along the western slope of the rise and perturbing the doming of isopycnals in this region.

Along the continental shelf slope there is a known enhancement of transport owing to the sloping of isopycnals down towards the continental shelf break. The Antarctic Slope Front (ASF) is a common oceanographic feature near the shelf break and is characterized by strong subsurface gradients in ocean temperature and salinity (Jacobs 1991) and accounts for ~50% of the transport of the Weddell Gyre in the south-eastern Weddell Sea. The ASF arises from the contrast of the cold relatively fresh waters filling the continental shelf and the warmer more saline waters father offshore. South of the ASF is the Antarctic Coastal Current which carries shelf waters westwards in the same direction as the deep basin gyre flow (Heywood et al. 2004, Núñez-Riboni and Fahrbach 2009).

With this knowledge of the broad hydrographic and transport conditions in the Weddell Gyre, it is practical to make use of quasi-synoptic in-situ physical oceanographic data and inverse methods to obtain a best estimate of the transport through the region. The LaKriS campaign includes CTD stations and underway acoustic Doppler current profilers (ADCPs) that span the abyssal plain, Maud Rise and the continental slope and shelf. The dataset therefore provides an interesting region in which to contribute to one of the major tasks of oceanography: estimating the mean ocean circulation.

Whilst the use of inverse methods in geophysics has a long history, Wunsch (1978) in particular laid the foundation for widespread use within oceanography through a box-model formulation for the North Atlantic using multiple intersecting sections. This demonstrated the utility of the technique in obtaining an estimate of the mean state of the ocean. Numerous other studies have made use of similar box-model techniques. A subsequent return to estimating the North Atlantic using a wider variety of parameters but a less complex collection of hydrographic data of two parallel sections was made by Rintoul and Wunsch (1991). A much broader study by Macdonald (1998) examining the global circulation based on 15 high-resolution sections across the globe concluded that whilst the study confirmed some existing knowledge and challenged other knowledge about ocean circulation, more hydrographic sections alone were insufficient in some regions to improve estimates of the detailed ocean circulation. At the scale of the global ocean the assumption of a steady-state/synoptic set of observations is identified as being the greatest limiting factor of their approach. This is reinforced in a similar global study by Ganachaud and Wunsch (2000) who conclude that the uncertainty in estimating the ocean circulation lies in the uncertainty introduced by real oceanic variability, and that effective temporal averaging from increased resolution of highly variable regions will be key to future progress. However, at smaller temporal scales across shorter time periods this is potentially less of an issue due to the reduced spread of observations in time and space.

A box-model of the Southern Ocean by Georgi and Toole (1982) investigates zonal heat and freshwater transports, noting the sensitivity of their solutions to the chosen reference level. The presence of baroclinic eddies is noted to also introduce uncertainties into the calculated heat and salt transports, with the cumulative errors preventing an assessment of freshwater exchanges although allowing the sign of the heat transports to be identified. This highlights the importance of having a robust method for setting a reference level in the ocean. A more conclusive study of South Atlantic exchange was undertaken by Rintoul (1991) requiring the closure of the deep overturning circulation primarily via the “cold water path” of circumpolar transports from the Atlantic and back via Drake Passage.

More recently studies of the Southern Ocean have included an examination of AABW export from the Weddell Sea into the Scotia Sea (Naveira Garabato et al. 2002b) and the net transport through the Scotia Sea (Garabato et al. 2003) using a series of cruises along the bathymetric boundaries of the Scotia Sea. Sloyan and Rintoul (2001) use a series of 9 hydrographic sections to diagnose the large-scale Southern Ocean circulation south of ~12^{o}S. These studies use an enclosure of an area of ocean by perimeter hydrographic sections to construct a box-model for transports across those perimeter boundaries at varying degrees of scale.

Casal et al. (2009) takes a similarly classical approach in the Agulhas Retroflection along the coast of South Africa, making use of lowered-ADCP for comparison with geostrophic model runs. They highlighted similarity in transports between the two model setups in the surface ocean but large differences at intermediate and deep levels demonstrating the need for the inclusion of in-situ measurements of the total transport. McDonagh et al. (2008) examine a single section across the Indian Ocean at 32^{o}S, making use of shipboard and lowered ADCP data to set the reference velocity for the initial geostrophic field. They also note the additional detail provided by making use of ADCP data in resolving the horizontal circulation. Earlier investigation by Losch et al. (2002) and Losch and Schroter (2004) made use of measurements of sea-surface height data by satellite altimetry to improve the estimates of ocean circulation. The inaccuracies of the geoid are included in their calculation of absolute sea surface height, however their experiments still reduce the error of flux estimates by up to 55%, although they conclude that the method is inconsistent with hydrographic estimates as a result of the formal errors of the geoid underestimating its true error. Nevertheless this demonstrates the value of introducing reference information even if it has (at that time) low accuracy compared to the hydrographic measurements.

An interesting approach to geophysical inverse problems is to place less importance on obtaining a single credible solution and instead use a *Monte Carlo* approach: undertake multiple inversions of a set of slightly perturbed data to generate a set of possible solutions for comparison as described by Press (1968). Such an approach has the benefit of explicitly recognising that the components of a system of equations defined by in-situ observations have potentially both procedural

error in the collection of the data, and statistical error from spatial distribution of that data which may fail to observe variability within the system. This study will also make use of this approach.

The high density hydrographic datasets provided by the LaKriS campaign are well suited to conducting a 3-dimensional assessment of the circulation, and the inverse technique is well suited for such an analysis. The Inverse Multi-Box Adaptable Model (IMBAM) has been created and developed to make such an estimation of the circulation and is described in this study.

4.2 Data

The Lazarev Sea Krill Study (LaKriS) consists of 4 cruises undertaken by the *RV Polarstern* from 2004 through to 2008 straddling the southern part of the Weddell Gyre from ~60°S to the Antarctic continent. For full details see the appropriate cruise reports: Smetacek et al. (2005); Strass (2007); Bathmann (2008) and Bathmann (2010). Each cruise covers an area extending westward from Maud Rise, although the exact coverage varies from cruise-to-cruise as detailed in Table 4.2.4.

The most extensive survey undertaken was ANT-XXIII/2 (Figure 4.2.16 b) which comprised 4 meridional sections with regular full-depth stations and good coverage of the continental slope. The next-most comprehensive survey was ANT-XXIII/6 (Figure 4.2.16 c) with 3 full meridional section and regular full-depth stations, although fewer stations over the continental slope. The repeat of the 6°W section was abandoned due to the severe winter sea ice conditions.

The other two cruises are less systematic with various strengths and weaknesses. Whilst comprising of 4 meridional sections, ANT-XXI/4 (Figure 4.2.16 a) has no station coverage in the northwest corner of the survey area and the station spacing is wider to the north and narrower to the south than with the other cruises, although this does afford it good coverage of the continental slope. Across the middle of the survey area there is a scarcity of full-depth stations except for along the Greenwich Meridian posing problems for examining the deep ocean.

Cruise	Cruise Dates	Austral Season	Section longitude	Domains	CTD	VM-ADCP
ANT-XXI/4	27/03/2004 - 06/06/2004	Autumn	6°W, 4°W, 2°W, 0°	F, D	Seabird-911 Plus	RDI Ocean Surveyor, 150/153.6 kHz
ANT-XXIII/2	19/11/2005 - 12/01/2006	Summer	6°W, 3°W, 0°, 3°E	F, D, S		
ANT-XXIII/6	17/06/2006 - 21/08/2006	Winter	3°W, 0°, 3°E	F, D		
ANT-XXIV/2	28/11/2007 - 04/01/2008	Summer	3°W, 0°, 3°E	F		

Table 4.2.4 – LaKriS cruise information including: cruise dates; austral season; the longitude of each section; whether the cruise was analysed using the full (F), duplicate (D) and subset (S) domain setups; and the CTD and ADCP equipment used to collect the data.

ANT-XXIV/2 (Figure 4.2.16 d) has poor coverage of the continental slope and gaps in the northwest and northeast of the survey area which renders the northern-most 4 stations of highly limited use for the purposes of box-modelling. In addition, unlike the other 3 cruises, none of the sections comprise predominantly full-depth stations. The Greenwich Meridian section is particularly scarce of full-depth stations, although the 3°W and 3°E sections actually have a higher density of full-

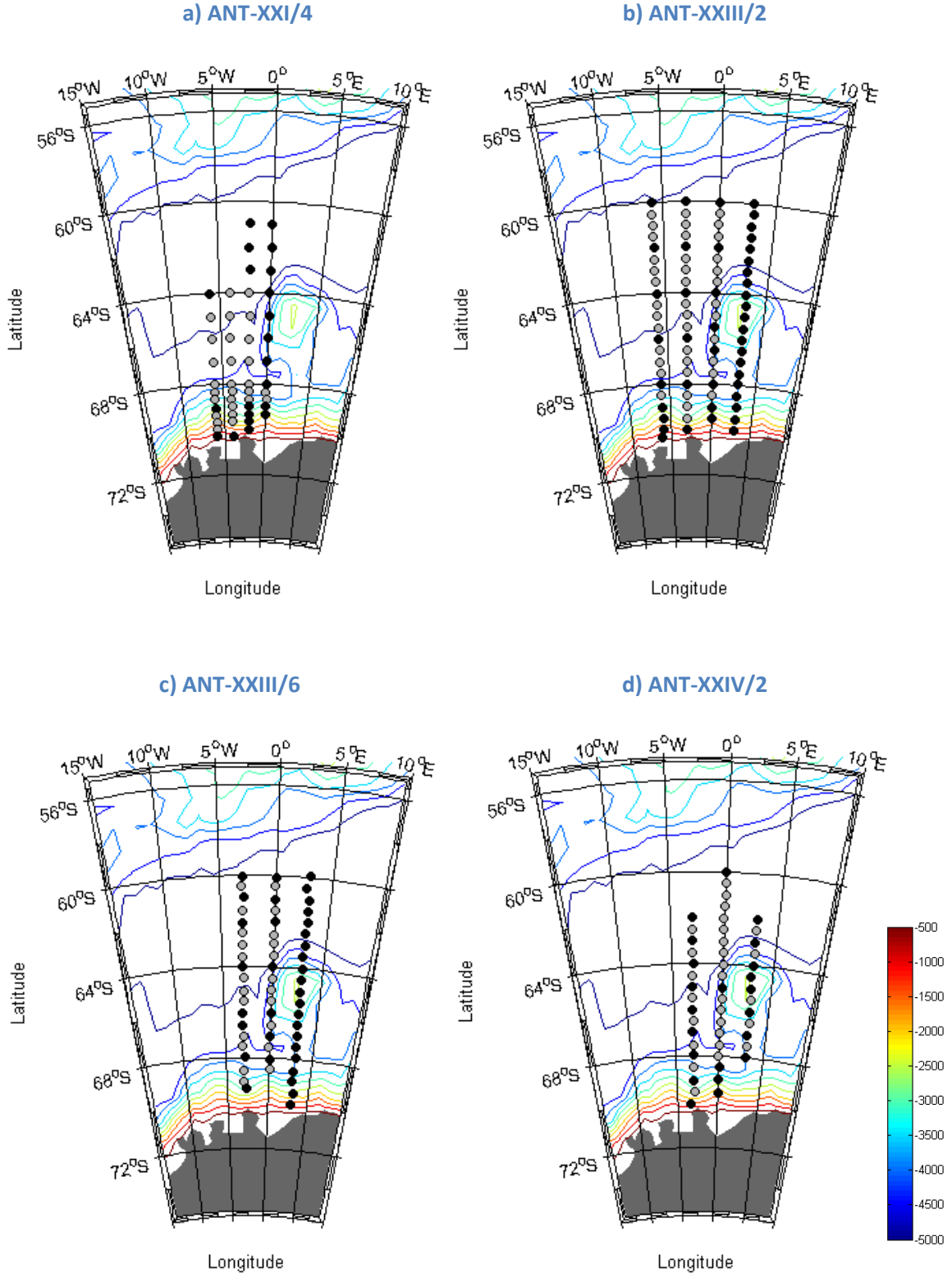

Figure 4.2.16 – The location of full-depth (black circles) and 1000m (grey circles) CTD station for the four Lazarev Sea Krill Study (LaKriS) cruises. The Antarctic continent in shown dark grey along with coloured bathymetric contours at 500 m intervals from 500m to 5000 m.

depth stations than any of the other cruises. The limitations of this data are largely due to *Polarstern* rendering ice breaking duties to a freighter carrying construction material for the Neumayer III Antarctic research station, losing ten days from the scientific programme.

Whilst it is always preferable to have a 'complete' dataset rather than having an 'incomplete' dataset, the preponderance of shallow stations does not preclude the use of the data in a box-model. It does however place limitations on the confidence of those results for the deep ocean. All non-full depth stations reach ~1000 m which includes the bulk of the WDW in the Weddell Gyre (Cisewski et al. 2011). As WDW is a key water mass for the propagation of temperature and salinity anomalies into the western Weddell Gyre, it is perhaps less of a concern within this focus than might otherwise be considered.

Different model domain set-ups are investigated in this study: the 'full' model domains use all of the available appropriate stations; the 'duplicate' domains use any single full-depth section which is then duplicated to test a 2-D model set-up; and a 'subset' domain of ANT-XXIII/2 using only the stations which were coincident with those surveyed during ANT-XXIV/2 in order to test the robustness of the solutions.

On each cruise *Polarstern* collected data from the vessel mounted acoustic Doppler current profiler (VM-ADCP) which was processed and de-tided in the manner outlined by Cisewski et al. (2011) as follows. The velocity components were averaged in 2 min ensembles in 4m thick depth bins between 19 and 335m depth and any near surface effects were avoided by setting the reference layer to bins 6-15. The ship's gyro platform was used to translate the ADCP velocities into earth coordinates and the ship's velocity was calculated from Global Positioning System fixes. The errors associated with the accuracy of the ship's position fixes, heading data and misalignment of the ADCP with ship's axis were reduced using standard watertrack calibration methods (Joyce 1989, Pollard and Read 1989); with further ADCP processing carried out using the CODAS3 software package developed by E. Firing and colleagues (Firing 1991); and barotropic tidal currents were removed using the Circum-Antarctic Tide Model CATS02.01 developed by Padman et al. (2002). The end result is a set of 5 useable ADCP layers: 18-50 m, 51 to 100 m, 101 to 150 m, 151 to 200 m, and 201 to 250 m.

In addition to this processing, the ADCP data was used as follows:

Firstly, the data was used in a format which we shall refer to as 'raw': full temporal resolution ADCP data from which an average ADCP layer velocity was calculated for all station pairs along *Polarstern's* cruise track within $\pm 0.3^{o}$ latitude or longitude depending on the orientation of the station pair. This allowance accounts for the natural drift of the ship whilst it is underway, an effect which can be more pronounced in heavy sea ice conditions, or any other minor diversions from a direct

cruise track. Where two station pairs are perpendicular to one another this has the effect of making use of some velocity vector positions for more than one station. This is not considered to introduce observational bias as firstly this includes relatively few vectors, and secondly the calculated vectors for two such station pairs are also perpendicular and thus there is no duplication of vector information. As this raw data only exists for the cruise track, the process creates a set of velocity references which does not include every possible adjacent station pair combination and, in the case of the LaKriS data, does not provide a fully referenced domain boundary.

Secondly, the ADCP data is processed to obtain a streamfunction from the ADCP data as described in Leach (1986). First the relative positions of the data are determined, followed by an objective analysis to map the raw data across the entire domain. A non-divergent flow is then imposed across the domain through solving the Poisson function. The solution to the Poisson function is then translated back to absolute positions. A stream function is obtained from this process which can then be differentiated to obtain mean velocity transports across each adjacent station pair in the grid.

Lastly, the stream function calculations are undertaken with 10 sets of randomly perturbed ADCP data. For each set of data perturbations a uniform distribution of random numbers, multiplied by the error of the raw ADCP velocities is used to generate a unique perturbation of the ADCP data. In the case of the LaKriS data the meridional error is 0.5 cm s^{-1} and the zonal error is 0.3 cm s^{-1} in accordance with the ADCP error calculations laid out by Cisewski et al. (2011). The same procedure as outlined earlier is then undertaken to obtain a stream function and subsequent differentiated mean velocity transport for each station pair.

As the ‘stream function’ technique relies on having data across the entire domain, for some cruises the ‘stream function’ ADCP solution does not include the entire CTD grid and instead just a subset of the domain to avoid introducing any erroneous reference values through irregular distribution of ADCP data. This has the unfortunate consequence of not providing a fully referenced domain (Figure 4.2.17).

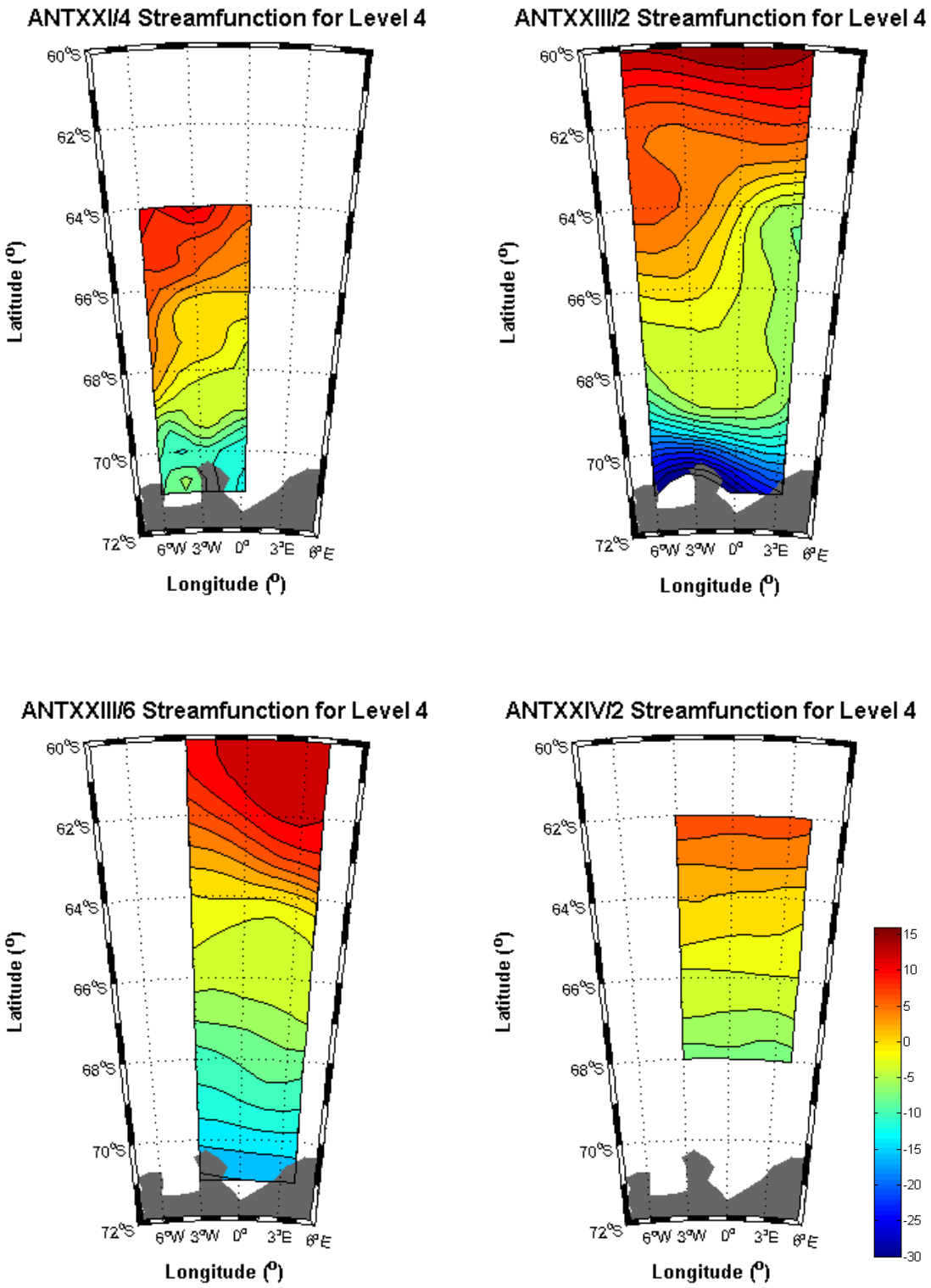

Figure 4.2.17 – Example VM-ADCP stream function plots for the 4 LaKriS cruises. Each stream function is for layer 4 covering a depth range of 150-200 m. Due to restrictions of the processing program some stream functions appear to extend onto the continent, but this is just an artefact of the processing and has little impact on the stream function output.

4.3 Methods

In the spirit of Wunsch (1978), this study aims to provide an estimate for the circulation in the Lazarev Sea using a box inverse method. Traditional box inverse methods involve using a set of CTD sections enclosing a part of the ocean, with the fluxes determined for that single large box or set of boxes. This study takes a different approach by using closely spaced hydrographic data to define a series of interconnected boxes defined by groups of four neighbouring CTD stations. Using this interconnection as a basis, the Inverse Multi-Box Adaptable Model (IMBAM) has been developed to make best use of the LaKriS physical oceanography dataset.

4.3.1 The inverse problem and the least squares solution

For an exactly determined system of equations with an invertible square matrix:

$$[1] \qquad Ax = b$$

Where A is the invertible $m\,x\,m$ square matrix; b is a vector of length m with information pertaining to matrix A; and x is a vector of length m which is the exact solution to a system of equations, such that:

$$[2] \qquad x = A^{-1}b$$

However, for a system of over or underdetermined equations whereby A is non-square and non-invertible, with $m\,x\,n$ dimensions, attempting to obtain a solution for x will necessarily involve a residual error, n, associated with calculating a non-exact system:

$$[3] \qquad Ax = b + n$$

An approximation of such an inverse solution, known as the Moore-Penrose Pseudo-Inverse (M-P) or as simply a 'general inverse', is given by:

$$[4] \qquad A^{+} = A^{T}(AA^{T})^{-1}$$

The M-P inverse provides for the calculation of one specific solution to the over-determined formulation of the inverse problem [3] presented by the IMBAM model, in a least squares sense:

$$[5] \qquad x = A^{T}(AA^{T})^{-1}(b)$$

Rather than attempting to infer anything physical about the value of x, it is best to interpret it in an operational sense as a solution of maximum simplicity as it provides a specific solution with minimum norm for $Ax - b$.

For the purposes of computational efficiency this study makes use of the left matrix division operator provided by MATLAB which computes a least squares solution for an overdetermined system of equations.

4.3.2 Model set-up

The least squares framework is used to construct a system of equations to provide potential solutions for volume transport through the Lazarev Sea. In order to obtain an estimate of transport through the Lazarev Sea based on the LaKriS surveys, it is necessary to assume that each individual survey is a quasi-synoptic snapshot of the hydrographic conditions. To begin, imagine two density layers (see Figure 4.3.18), one above the other; the flow in the upper layer is related to the flow in the lower by:

$$[6] \qquad u_{\iota\iota+1,JJ} = u_{\iota\iota,JJ} + b_{\iota,JJ}$$

Where $u_{\iota\iota,JJ}$ is the normal velocity across the lower density layer ($\iota\iota$) between a station pair (JJ), and $u_{\iota\iota+1,JJ}$ is the normal velocity for the upper density layer ($\iota\iota$+1) between the same pair of stations (JJ); and $b_{\iota,JJ}$ is the velocity difference between the two layers (ι) related to the thermal wind equation, and often called the Margules equation (Margules 1906):

$$[7a] \qquad b_{\iota,JJ} = \frac{g\Delta\bar{\rho}}{fL\rho_{\iota,JJ}}\,\Delta h$$

The density difference between the layers can be represented numerically as:

$$[7b] \qquad \Delta\bar{\rho} = \frac{\left(\overline{\rho_{\iota\iota,J}} + \overline{\rho_{\iota\iota,J+1}}\right)}{2} - \frac{\left(\overline{\rho_{\iota\iota+1,J}} + \overline{\rho_{\iota\iota+1,J+1}}\right)}{2}$$

Where g is the gravitational constant; $\Delta\bar{\rho}$ is the difference in the mean density of the two layers ($\iota\iota$ & $\iota\iota+1$) between the two stations (J & $J+1$) defined in equation [7b]; f is the Coriolis Parameter calculated at the half-way point between the station pair; L is the spherical distance between the station pair; $\rho_{\iota,JJ}$ is the density of the interface between the layers; and Δh is the change in depth of the density surface from one station to the next, as shown in Figure 4.3.18.

The next consideration is the conservation of mass. Owing to the assumption of the LaKriS surveys being synoptic, consideration of mixing and diapycnal velocities can be reasonably neglected, leaving only isopycnal conservation of mass (see Figure 4.3.19), which for a single density layer box is:

$$[8] \qquad -(ua\bar{\rho})_{\iota\iota,1} - (ua\bar{\rho})_{\iota\iota,2} + (ua\bar{\rho})_{\iota\iota,3} + (ua\bar{\rho})_{\iota\iota,4} = 0$$

Where u, as before, is the normal velocity for a density layer; $\bar{\rho}$ is the mean density of the layer as earlier explained by Figure 4.3.18; and a is the cross-sectional area of the density layer faces. The sign of each term relates to the orientation convention in Figure 4.3.19.

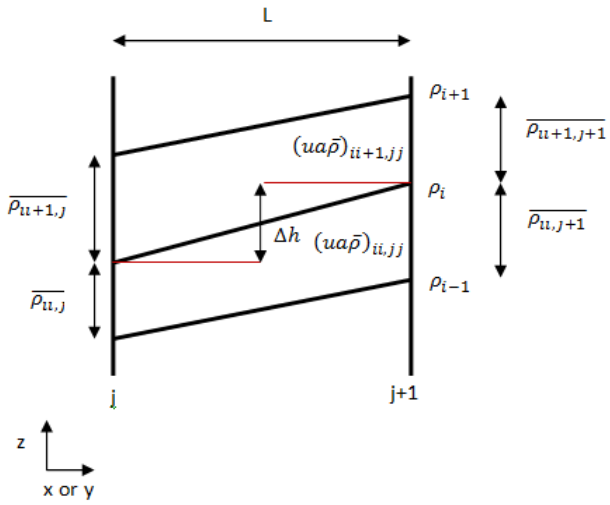

Figure 4.3.18 – Thermal wind terms for a simple two layer example. Stations are referred to as j and j+1, with density referred to as ρ relative to i, the middle density surface. The mean layer densities $\overline{\rho}$ are relative to the density layer at ii and station pair jj.

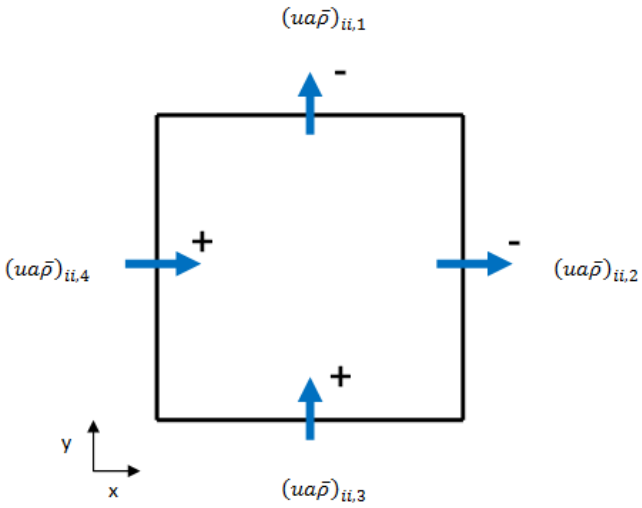

Figure 4.3.19 – Sign convention of mass conservation equations. The northern (1) and eastern (2) faces are negative whilst the southern (3) and western (4) faces are positive reflecting positive values for u and v through y and x, respectively. This is simply a convention applied to the orientation of data grids and does not restrict the use of IMBAM to irregularly spaced data or angled grids.

A classical issue with ocean circulation inverse problems is determining or setting a level about which the motion is known. Sometimes this is resolved with merely setting a level of no

motion, either at the bottom or at some intermediate depth, or by undertaking some iterative improvement process. Instead, this study adopts the use of ADCP data to provide reference velocities in the upper water column in a similar manner to the dynamical method outlined by Cisewski et al. (2011), so that:

$$[9] \qquad u_{\iota\iota,JJ} = r_{\iota\iota,JJ}$$

Where $u_{\iota\iota,JJ}$, as before, is the normal velocity for a density layer face; and $r_{\iota\iota,JJ}$ is a reference velocity specified for that same density layer face. In order to bring this information together, the system of equations is combined by relating them to [1] such that a series of sparse linear matrices are combined:

$$[10] \qquad \begin{Bmatrix} A_1 \\ A_2 \\ A_3 \end{Bmatrix} U = \begin{Bmatrix} b_1 \\ b_2 \\ b_3 \end{Bmatrix}$$

Where A_1 and b_1 relate to thermal wind [7]; A_2 and b_2 relate to mass conservation [8]; A_3 and b_3 relate to reference velocities [9]; and U is the unknown solution for the normal velocity to each vertical density layer face. Expressed individually:

$$[11] \qquad \begin{Bmatrix} 1 & -1 & \cdots & 0 \\ \vdots & \ddots & \ddots & \vdots \\ 0 & \cdots & 1 & -1 \end{Bmatrix} U = \begin{Bmatrix} b_{1,1} \\ \vdots \\ b_{\iota,JJ} \end{Bmatrix}$$

$$[12] \qquad \{-a\bar{\rho}_{\iota\iota,1} \quad -a\bar{\rho}_{\iota\iota,2} \quad a\bar{\rho}_{\iota\iota,3} \quad a\bar{\rho}_{\iota\iota,4}\}\, U = \{0\}$$

$$[13] \qquad \{1\}\, U = \{r_{\iota\iota,JJ}\}$$

When considering the full matrix for a 1-box (4 station pairs), 2-layer example with the surface layer referenced to known velocities, a concatenated matrix is formed. Equation [14] is highlighted with the relationship between the upper and lower layers on the first face (red), the inflow and outflow from the bottom layer (blue); and the velocity referencing of the surface layer (green) as defined by matrix equation [14] and illustrated by Figure 4.3.20:

$$[14] \qquad \begin{Bmatrix} -1 & 1 & \cdots & \cdots & \cdots & \cdots & \cdots & 0 \\ \vdots & \vdots & -1 & 1 & \cdots & \cdots & 0 & \vdots \\ \vdots & 0 & \cdots & \cdots & -1 & 1 & \vdots & \vdots \\ 0 & \cdots & \cdots & \cdots & \cdots & \cdots & -1 & 1 \\ -a\bar{\rho}_{1,1} & 0 & -a\bar{\rho}_{1,2} & 0 & a\bar{\rho}_{1,3} & 0 & a\bar{\rho}_{1,4} & 0 \\ 0 & -a\bar{\rho}_{2,1} & 0 & -a\bar{\rho}_{2,2} & 0 & a\bar{\rho}_{2,3} & 0 & a\bar{\rho}_{2,4} \\ \vdots & 1 & \cdots & \cdots & \cdots & \cdots & \cdots & 0 \\ \vdots & \vdots & 0 & 1 & \cdots & \cdots & 0 & \vdots \\ \vdots & 0 & \cdots & \cdots & \cdots & 1 & \vdots & \vdots \\ 0 & \cdots & \cdots & \cdots & \cdots & \cdots & \cdots & 1 \end{Bmatrix} \begin{Bmatrix} u_{1,1} \\ u_{2,1} \\ u_{1,2} \\ u_{2,2} \\ u_{1,3} \\ u_{2,3} \\ u_{1,4} \\ u_{2,4} \end{Bmatrix} = \begin{Bmatrix} b_{1,1} \\ b_{1,2} \\ b_{1,3} \\ b_{1,4} \\ 0 \\ 0 \\ r_{2,1} \\ r_{2,2} \\ r_{2,3} \\ r_{2,4} \end{Bmatrix}$$

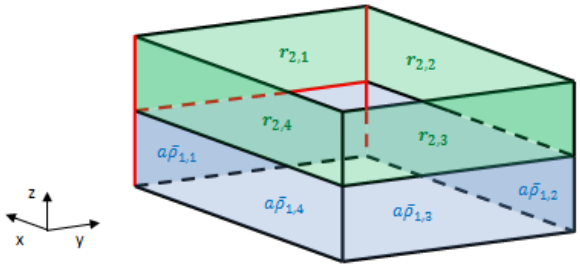

Figure 4.3.20 – Basic box-model set-up for the 2-layer, 4-face, 1-box example.

When combined for a simple 2-parallel-face, 3-layer example, again with the surface layer referenced to known velocities, the concatenated matrix has increasing complexity within the A_1 and b_1 sub-matrices as shown in equation [15]. Here it is highlighted with the interaction of the mid-layer with the layers above and below (red); the inflow and outflow from the mid-layer (blue); and, again, velocity referencing of the surface layer (green) as defined by matrix equation [15] and illustrated by Figure 4.3.21:

$$[15] \quad \begin{Bmatrix} -1 & 1 & \cdots & \cdots & \cdots & 0 \\ \vdots & -1 & 1 & \cdots & 0 & \vdots \\ \vdots & 0 & \cdots & -1 & 1 & \vdots \\ 0 & \cdots & \cdots & \cdots & -1 & 1 \\ a\bar{\rho}_{1,1} & 0 & 0 & -a\bar{\rho}_{1,2} & \cdots & 0 \\ \vdots & a\bar{\rho}_{2,1} & 0 & 0 & -a\bar{\rho}_{2,2} & \vdots \\ 0 & \cdots & a\bar{\rho}_{3,1} & 0 & 0 & -a\bar{\rho}_{3,2} \\ 0 & \cdots & 1 & \cdots & \cdots & 0 \\ 0 & \cdots & \cdots & \cdots & \cdots & 1 \end{Bmatrix} \begin{Bmatrix} u_{1,1} \\ u_{2,1} \\ u_{3,1} \\ u_{1,2} \\ u_{2,2} \\ u_{3,2} \end{Bmatrix} = \begin{Bmatrix} b_{1,1} \\ b_{2,1} \\ b_{1,2} \\ b_{2,2} \\ 0 \\ 0 \\ 0 \\ r_{3,1} \\ r_{3,2} \end{Bmatrix}$$

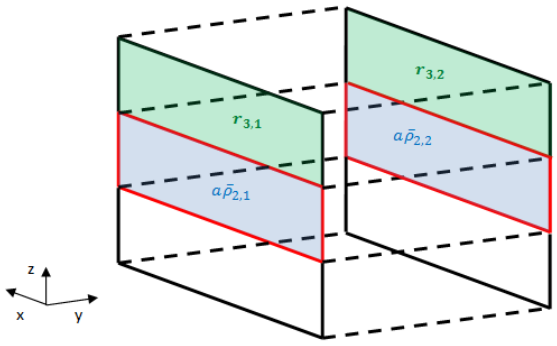

Figure 4.3.21 – Basic box model set-up for the 3-layer, 2-parallel face example.

Finally, by way of example of interconnection, a 3-parallel-faces, 2-layer example with surface referencing demonstrates another element of the complexity of the matrix construction in equation [16]. The connection of mass conservation is highlighted with the centre face layers (red), the differing signs of the mass fluxes into and out of that same set of layer faces (blue) and a single surface reference (green) as defined by matrix equation [16] and figure illustrated by Figure 4.3.22:

$$\begin{Bmatrix} -1 & 1 & \cdots & \cdots & \cdots & \cdots & \cdots & \cdots & 0 \\ \vdots & -1 & 1 & \cdots & \cdots & \cdots & \cdots & 0 & \vdots \\ \vdots & \vdots & \vdots & -1 & 1 & \cdots & 0 & \vdots & \vdots \\ \vdots & \vdots & 0 & \cdots & -1 & 1 & \vdots & \vdots & \vdots \\ \vdots & 0 & \cdots & \cdots & \cdots & \cdots & -1 & 1 & \vdots \\ 0 & \cdots & \cdots & \cdots & \cdots & \cdots & \cdots & -1 & 1 \\ a\bar{\rho}_{1,1} & 0 & 0 & -a\bar{\rho}_{1,2} & \cdots & \cdots & \cdots & \cdots & 0 \\ \vdots & a\bar{\rho}_{2,1} & 0 & 0 & -a\bar{\rho}_{2,2} & \cdots & \cdots & 0 & \vdots \\ \vdots & \vdots & a\bar{\rho}_{3,1} & 0 & 0 & -a\bar{\rho}_{3,2} & 0 & \vdots & \vdots \\ \vdots & \vdots & 0 & a\bar{\rho}_{1,2} & 0 & 0 & -a\bar{\rho}_{1,3} & \vdots & \vdots \\ \vdots & 0 & \cdots & \cdots & a\bar{\rho}_{2,2} & 0 & 0 & -a\bar{\rho}_{2,3} & \vdots \\ 0 & \cdots & \cdots & \cdots & \cdots & a\bar{\rho}_{3,2} & 0 & 0 & -a\bar{\rho}_{3,3} \\ 0 & \cdots & 1 & \cdots & \cdots & \cdots & \cdots & \cdots & 0 \\ 0 & \cdots & \cdots & \cdots & \cdots & 1 & \cdots & \cdots & 0 \\ 0 & \cdots & \cdots & \cdots & \cdots & \cdots & \cdots & \cdots & 1 \end{Bmatrix} \begin{Bmatrix} u_{1,1} \\ u_{2,1} \\ u_{3,1} \\ u_{1,2} \\ u_{2,2} \\ u_{3,2} \\ u_{1,3} \\ u_{2,3} \\ u_{3,3} \end{Bmatrix} = \begin{Bmatrix} b_{1,1} \\ b_{2,1} \\ b_{1,2} \\ b_{2,2} \\ b_{1,3} \\ b_{2,3} \\ 0 \\ 0 \\ 0 \\ 0 \\ 0 \\ 0 \\ r_{3,1} \\ r_{3,2} \\ r_{3,3} \end{Bmatrix}$$

[16]

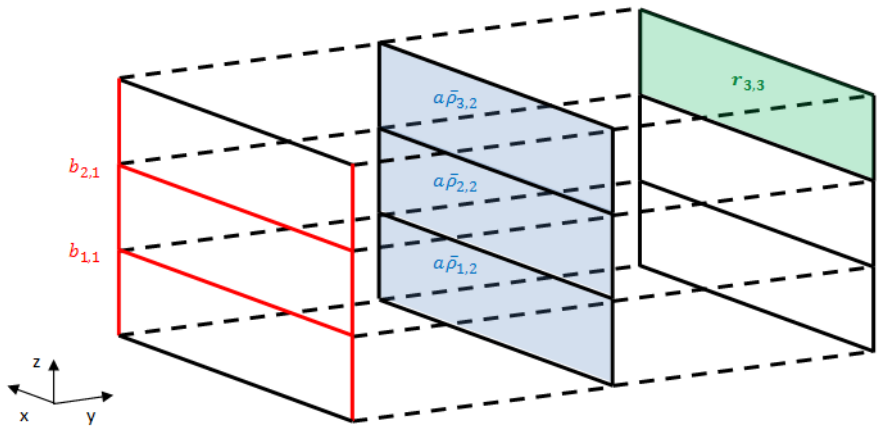

Figure 4.3.22 – Basic box model set-up for the 3-layer, 3-parallel face example.

From the three examples given in equations [14], [15] and [16] it can be seen that the complexity of the sparse linear matrix grows rapidly with additional dimensions, layers and layer referencing. For an interconnected domain of 3 columns by 20 rows of boxes with 21 density layers and one reference value per section produces a sparse linear matrix of size 4380 x 3003. The non-zero elements of the *A*-matrix for this example are shown as blue dots in Figure 4.3.23, highlighting the relationship of the thermal wind terms with the mass conservation and velocity referencing, and the multiple-interconnections of the mass conservation terms.

Whilst this demonstrates the complexity and size of the *A*-matrix, it is also necessary to consider that given the nature of the data, not all columns and rows will have non-zero elements due to the absence of density layers at some stations. Therefore the matrices generated by IMBAM are formally rank deficient as there are redundant row and columns. However the matrices are not structurally rank deficient as those empty columns and rows pertain to non-existent layer flows for which the solution generates a corresponding zero answer. Whilst they could be removed for the computational efficiency of obtaining the least squares solution, it is beneficial to maintain these rows for ease of mapping the solution back into the appropriate spatial distribution.

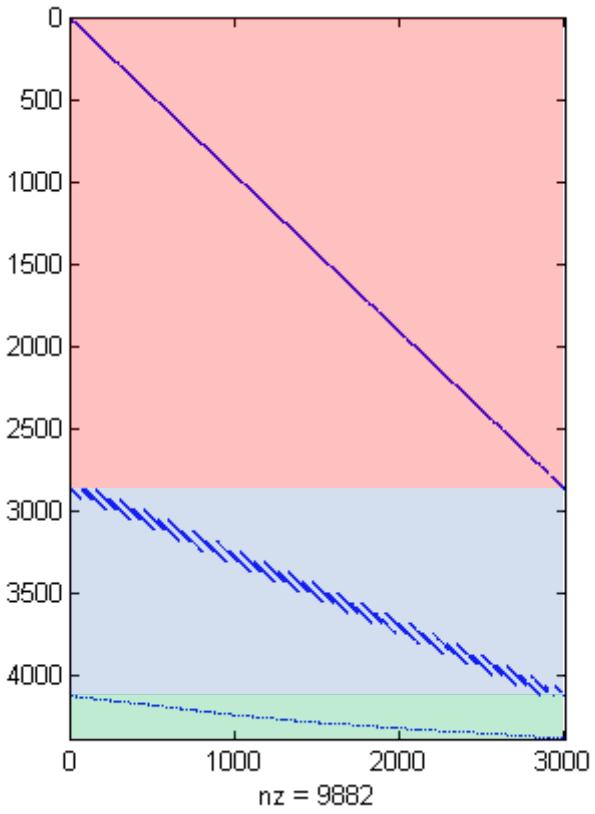

Figure 4.3.23 – Plot of all non-zero *A*-matrix elements (blue dots) for a 3 column, 20 row (therefore 60 box), and 21 density layers with one reference level per section, as for one of the full domain model runs of ANT-XXIII/2. Shaded according to thermal wind (red), mass conservation (blue) and velocity reference (green).

The IMBAM model is designed to be adaptable to the domain size of the data, generating an *A* matrix to represent the interconnected nature of the neighbouring CTD-defined boxes.

4.3.3 Density considerations

A fundamental consideration for a box model with vertical structure is the definition of the surfaces that define this vertical structure. As density is the controlling factor in the baroclinic component of transport clearly density surfaces are the variable of choice. Meaningful qualitative results can be achieved using potential density referenced to the sea surface, but this is a poor choice in the deep ocean due to the pressure effect. The use of potential density referenced to other depths is undesirable due to the discontinuity that would be introduced into mass conservation when density layers cross reference depths. The current optimal choice is Neutral Density, which has inherent pressure dependence and is an attempt to represent neutral surfaces along which a particle requires no energy for work to be done (Jackett and McDougall 1997).

The ideal scenario for examining transport through the Lazarev Sea would be to do so in direct relation to the properties of the local water masses defined by their potential temperature and practical salinity. However it is clear that an exact match cannot be obtained with Neutral Density when both temperature and salinity play important roles in determining the density structure in this region of the ocean. Figure 4.3.24 shows an attempt to approximate the domains of the water masses with Neutral Density surfaces, where there are clear but tolerable deviations of the surfaces about the isotherms and isohalines of interest. The equivalent water mass definitions for the 21 layer model set-up used in this study with IMBAM are outlined in Table 4.3.5.

The allocation of density layers is biased towards surface waters where greater variability is evident and thus a higher resolution is justified. Conversely in the deep and bottom waters, a greater number of density layers would offer minimal additional value, especially considering that a significant number of stations are surveyed to only 1000m depth.

4.3.4 Handling data irregularities

Due to the nature of the CTD data and the hydrographic conditions, there are a number of considerations for handling irregular data and isopycnal outcropping.

Firstly, it is necessary to make a choice on how to handle non-full depth station profiles, of which almost all are restricted to 1000m. The initial options seem to fall into two categories: accommodate the absence of data by redefining the equations to create bigger boxes where CTD data

a)

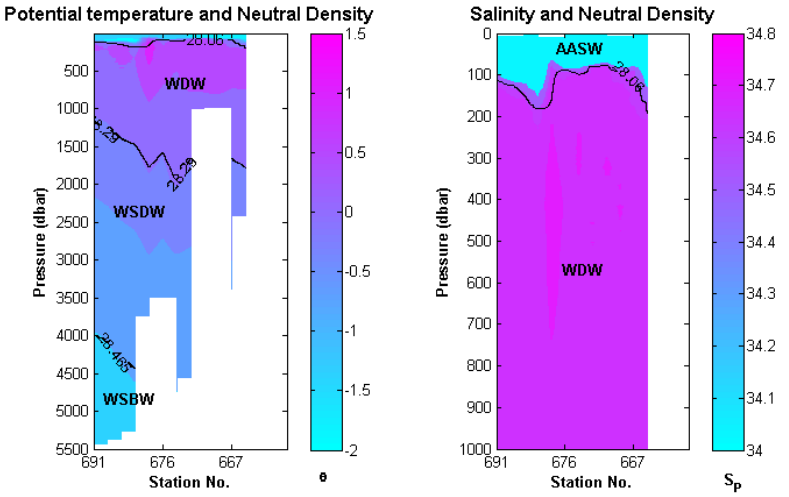

b)

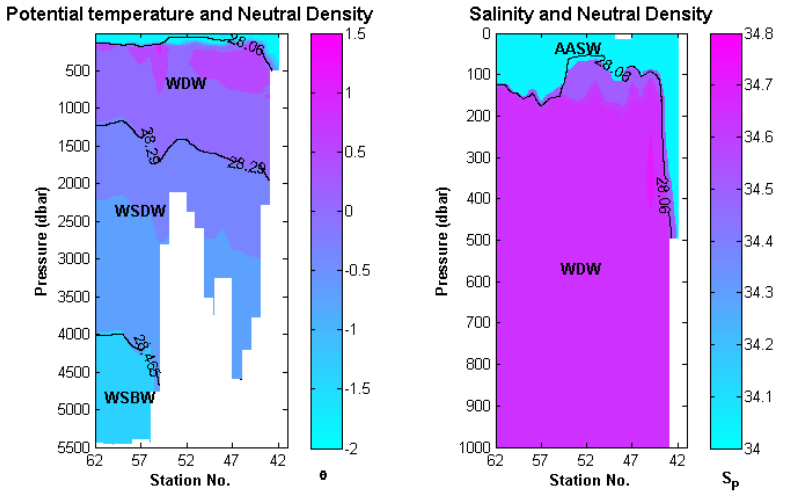

c)

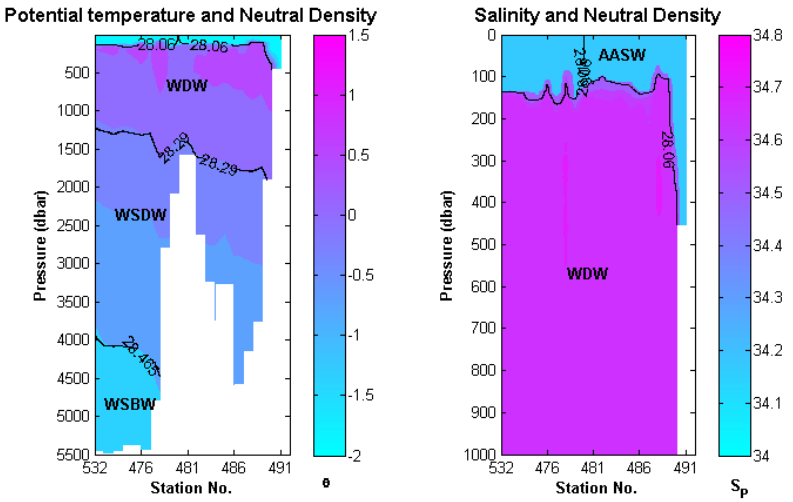

Figure 4.3.24 – Contour plots for sections of a) ANT-XXI/4 at the Greenwich Meridian, b) ANT-XXIII/2 at 3°E and c) ANT-XXIII/6 at 3°E. Colour contours are of full-depth potential temperature (left panel) and practical salinity to 1000 m (right panel). Black contour lines are the density surfaces related to the approximated boundary between water masses. There is good agreement between these approximations for all cruises.

Water Mass	Thermohaline definition	Neutral Density equivalent range	Other Inclusive Neutral Density surfaces
AASW	$S_P > 34.6$	$27.000 \leq \gamma_n < 28.060$	27.660; 27.720; 27.780; 27.840; 27.900; 27.960
WDW	$\theta < 0^oC$, $S_P > 34.6$	$28.060 \leq \gamma_n < 28.290$	28.085; 28.110; 28.135; 28.160; 28.185; 28.210; 28.235; 28.260
WSDW	$0^oC < \theta < -0.7^oC$	$28.290 \leq \gamma_n < 28.465$	28.325; 28.365; 28.410
WSBW	$\theta < -0.7^oC$	$28.465 \leq \gamma_n < 28.530$	None

Table 4.3.5 – Allocation of Neutral Density to approximate thermohaline definitions of Weddell Sea water masses.

is absent; or attempt to interpolate the missing CTD values by some scheme in order to maintain a less complicated formulation of the IMBAM model.

The solution used was a combination of both. As the choice of an interpolation scheme is largely subjective it is reasonable to avoid doing so if possible. Instead the known density layers for full-depth stations are laterally interpolated onto the profile of non-full depth stations to replicate the effect of including larger boxes (Figure 4.3.25). A simple linear interpolation is then used from the base of the existing profile to fill out the non-full depth profiles between those interpolated density surfaces to enable a straightforward processing of a 'full' dataset.

An undesirable result of having an original dataset which is incomplete at depth is the uncertainty introduced into examining the near-bottom layers. Whilst the actual water depth recorded at a station or data from a bathymetric product could be used to define the seabed depth, this does not resolve the issue of extrapolating density beyond the laterally interpolated density layers. IMBAM treats this problem by simply assuming a linear topographic interpolation in order to avoid introducing unnecessary complexity. Realistic topography would not necessarily add any useful information for the calculation of transports in either interpolated or non-interpolated layers, although it would result in some fraction of mass transport being omitted. This poses the greatest issue with respect to the representation of WSBW in the IMBAM solutions as it is only found to the north of the LaKriS domain and is poorly represented by sparse deep stations.

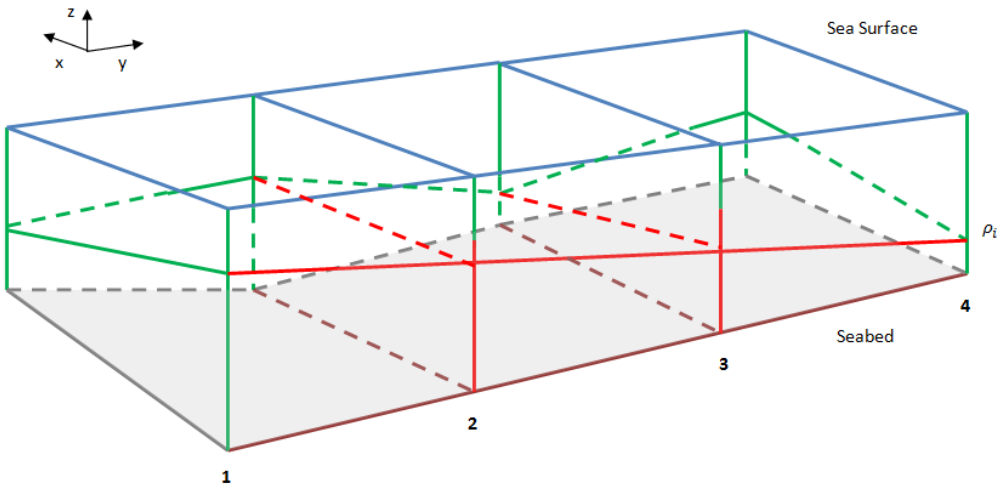

Figure 4.3.25 – Schematic of density surface and sea bed interpolation: sea surface (blue), existing CTD station profiles (vertical-green), existing sea bed depth (lateral-grey) and existing isopycnal surface ρ_i (lateral-green). Isopycnal surface ρ_i (lateral-red) and the sea bed depth (lateral-dark red) at station 2 and station 3 are linearly interpolated between the nearest straddling pair of stations 1 & 4. The density profile is then linearly interpolated in the vertical to provide a 'full' dataset.

However, the distribution of full depth stations in all the cruises tends to favour the areas of greatest topographic complexity. Specifically there is greater resolution across Maud Rise than further to the west where the topography deepens into abyssal plain, and the continental slope is reasonably well represented in all the cruises. The least favourable cruise in this respect is ANT-XXIV/2 which has many non-full depth stations along the Greenwich Meridian.

The remaining issue is that of isopycnals which outcrop at the surface or intersect with the seabed. The cross-sectional areas of these density layers are geometrically calculated according to the manner of the outcropping or intersection. For surface and seabed triangles, the difference in mean layer density and density layer height differences are estimated according to density surface interface values for outcropping surfaces, rather than through mean values of the density profile as used for all other density layer comparisons, including surface and seabed pentagons.

4.3.5 Integrating reference velocities

The IMBAM model approaches the issue of a level of known motion by using specified values from in-situ measurements as a point of reference. This can nominally be undertaken using any reference value at any depth or across a range of depths. Integration is achieved by binning reference data according to the nearest station pair and calculating the normal velocity to the plane of that station pair at the relevant density layer. It is then possible to weight the importance of these velocities depending upon the degree of confidence that the measurement is representative of the entire density layer face.

For instance, a single point current meter mooring would have a low weighting as it would represent only the velocity at that single point and may not be representative of an entire density surface face between two stations. Furthermore, a temporal integration would be required for a statistically meaningful value to be obtained and this could undermine the synoptic assumption required for this inverse approach.

A far more representative, and thus more heavily weighted example, would be a VM-ADCP: as mounted on *Polarstern* during the LaKriS cruises, and described in the section 4.2. This ADCP data has been pre-processed into a 'raw', 'stream function' and 'perturbed' format before being introduced into various IMBAM model runs. For the purposes of investigation the different calculated ADCP layers are used both separately and combined to compare the results of referencing to different levels of the water column. This is done by simply allowing every density layer which falls within the depth range of the ADCP layer to be assigned the relevant velocity, regardless of whether it is partially or fully within the ADCP layer depth range (Figure 4.3.26).

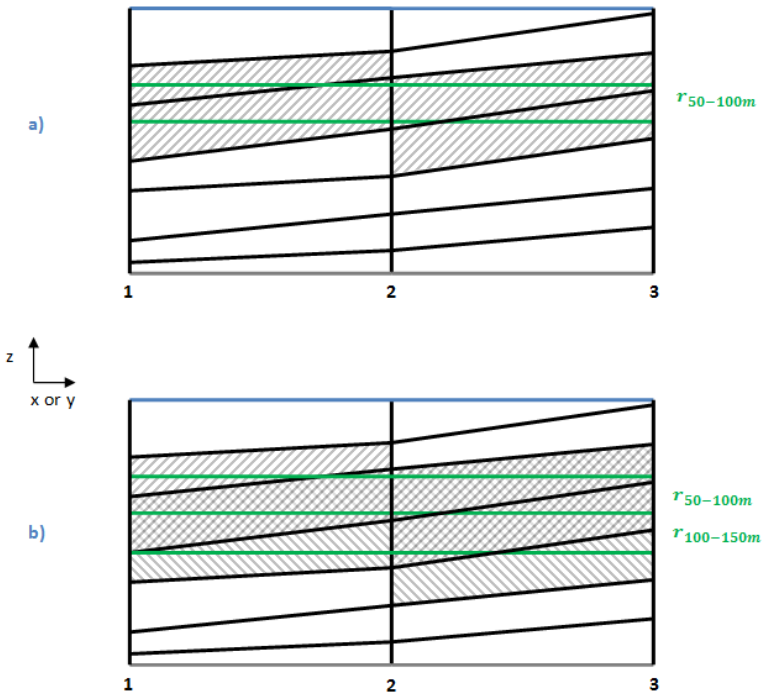

Figure 4.3.26 – Schematic of method for assigning velocity references to density layers. Stations 1,2 & 3 (black-vertical) with six density layers (black-lateral) between the sea surface (blue) and seabed (grey). Density layers (grey hatched) are referenced to ADCP layers (green); a) four density-layer faces are included within and referenced to the 50-100m ADCP layer; b) a single face is referenced solely to the 50-100m ADCP layer (forward hatch), whilst two faces are referenced only to the 100-150m ADCP layer (backward hatch), and three faces are referenced to both ADCP layers (cross-hatched).

In the case of using some or all of the layers, the same procedure applies resulting in some density layers having more than one velocity reference. The option exists to introduce weighting into this assignment of reference values, however as the ADCP data has already been binned and extensively processed prior to inclusion in the model, it seemed inappropriate to assign weights to averaged values which could just as equally apply to a partial layer as to a full layer.

4.3.6 Discounting wind forcing

Consideration was given to the inclusion of a surface reference velocity derived from the local wind field. The arising Ekman transport could be applied to the upper water column defined by the mixed layer depth. However there are good reasons not to do so.

Firstly, as detailed in chapter 1, the Weddell Gyre experiences large seasonal variability in sea-ice cover, reflected in the sea-ice conditions during the four LaKriS cruises. Variability in sea ice concentration combined with changes in atmospheric forcing over the duration of the cruises make calculation of a representative wind stress upon the ocean difficult and unreliable, especially within the quasi-synoptic framework required for this inverse method.

Secondly, the use of VM-ADCP data from the surface ocean is inclusive of the wind driven Ekman transport on the mean flow, regardless of the actual atmospheric forcing. This negates the need to explicitly include a wind forcing, particularly as this study compares referencing to different ADCP layers, above and below the mixed layer depth.

4.4 Results

Examination of the IMBAM results focuses on considering the robustness of the different solution formulations before proceeding to assess the solutions deemed to be most appropriate. Firstly, a comparison of velocity reference levels demonstrates the importance of using appropriate reference depth levels, and the even greater importance of making the most extensive practical use of the reference data. A brief comparison of IMBAM solutions for potential density and Neutral Density formulations show the large difference in volume transport resulting from different density definitions. Solutions from the raw format of ADCP data are contrasted with the stream function format of ADCP data to demonstrate differences in solution flow patterns. Next, the total transport of solutions from the raw, stream function and perturbed ADCP setups are compared to demonstrate the overall impact of the different referencing formulations. Consideration is then given to the results of a quasi-2-dimensional set-up of IMBAM to consider the impact of duplicating information within the model. These considerations are then summarised in advance of examining in detail the full domain solutions for *ANT-XXI/4, ANT-XXIII/2, ANT-XXIII/6* & *ANT-XXIV/2*, along with a subset domain solution for *ANT-XXIII/2*. These solutions are then compared like-for-like and then finally the results are summarised.

4.4.1 Comparison of reference levels

A key issue for examination is the appropriateness of the reference levels used to account for the barotropic component of transport. A reference level must provide a representative estimate of velocity or the reference will lead to a misleading solution. This is of concern particularly in boundary layers as the hydrographic conditions inside of the boundary layer may be sufficiently different to those outside the boundary layer to provide varying results.

Using a reference depth which is near the surface and within the active mixed layer influenced by Ekman transport would provide little certainty that the reference would have a useful relationship with the deep waters, whilst a deep reference level would be poorly representative of the surface flow. In each case the problem owes to the variability of the interface between the weakly

stratified surface layer and the more stably stratified deep waters. Therefore, providing velocity references for the surface and deeper waters is more productive. This is shown in Figure 4.4.27: the stream function of total volume transport divided by water column depth is shown to depict the streamlines of flow for solutions referenced to different ADCP layers (a-e) and all the ADCP layers together (f). Larger transports are achieved with deeper reference levels, whilst retaining the near surface reference layers contributes additional information about the more complex surface circulation, which is driven predominantly by Ekman transport and not the thermal wind which dominates in the deeper ocean.

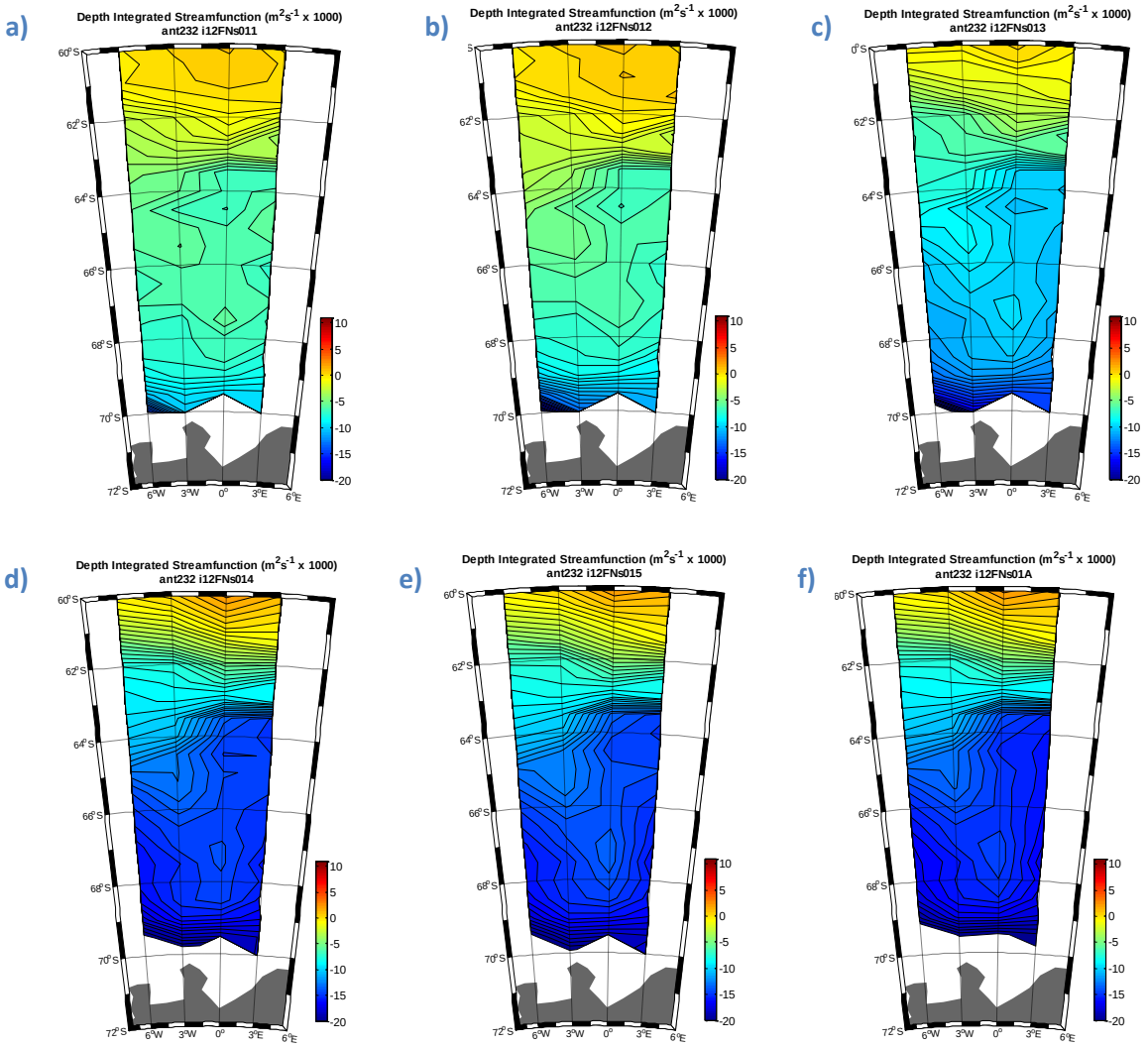

Figure 4.4.27 – Stream functions of IMBAM solutions showing full-depth volume transport divided by the total station-by-station depth of the water column for the *ANT-XXIII/2* cruise using the Neutral Density set-up for the full domain with stream function ADCP references levels of: a) 15-50m; b) 51-100m; c) 101-150m; d) 151-201m; e) 201-250m; f) all five references levels together.

Whilst the broad circulation of westward flow steered by the presence of Maud Rise at ~62°S and the continental slope south of 68°S is consistently present, Figure 4.4.27a has a significantly lower overall transport than Figure 4.4.27e and there are notable differences in stream lines: in the far north of the domain (potential recirculation vs. westward flow) and notable differences in the meandering in the middle of the domain (strong meandering vs. weaker meandering). Figure 4.4.27c-d are transitional states, whilst the solution in Figure 4.4.27f uses all of the reference levels and offers the best possible use of the available ADCP data.

4.4.2 Comparison of Neutral Density with potential density

Although not a focus of the main results, it is worthwhile to compare the operation of IMBAM in two different setups: using potential density referenced to the sea surface and Neutral Density to define the density layers. Figure 4.4.28 shows how both density surface definitions produce generally similar flow patterns, however a lower transport is calculated using potential density (Figure 4.4.28a) compared to the greater transport using Neutral Density (Figure 4.4.28b). Apart from the lower overall transport, there are obvious local variations in transport such as the recirculation at ~67°S using Neutral Density which is absent for the potential density set-up, and the anti-cyclonic flow around 66°S along 6°W using potential density but which is absent for the Neutral Density set-up.

A section of westward velocity for each of the potential density and Neutral Density model solutions along the Greenwich Meridian are presented in Figure 4.4.28c and Figure 4.4.28d, respectively. The general flow pattern is comparable: westward flow dominates north of Maud Rise, with low flow or eastward flow to the immediate south of Maud Rise, and an increased westward flow along the continental slope. However, the intensity of transport can be seen to noticeably vary. Comparing Figure 4.4.28d to Figure 4.4.28c: there is notably more intense westward flow on the northern flank of Maud Rise; an apparent counter current at ~4000m on the northern slope of Maud Rise, less intense eastward flow to the south of Maud Rise, and notably more intense flow over the continental slope – in both eastward and westward directions.

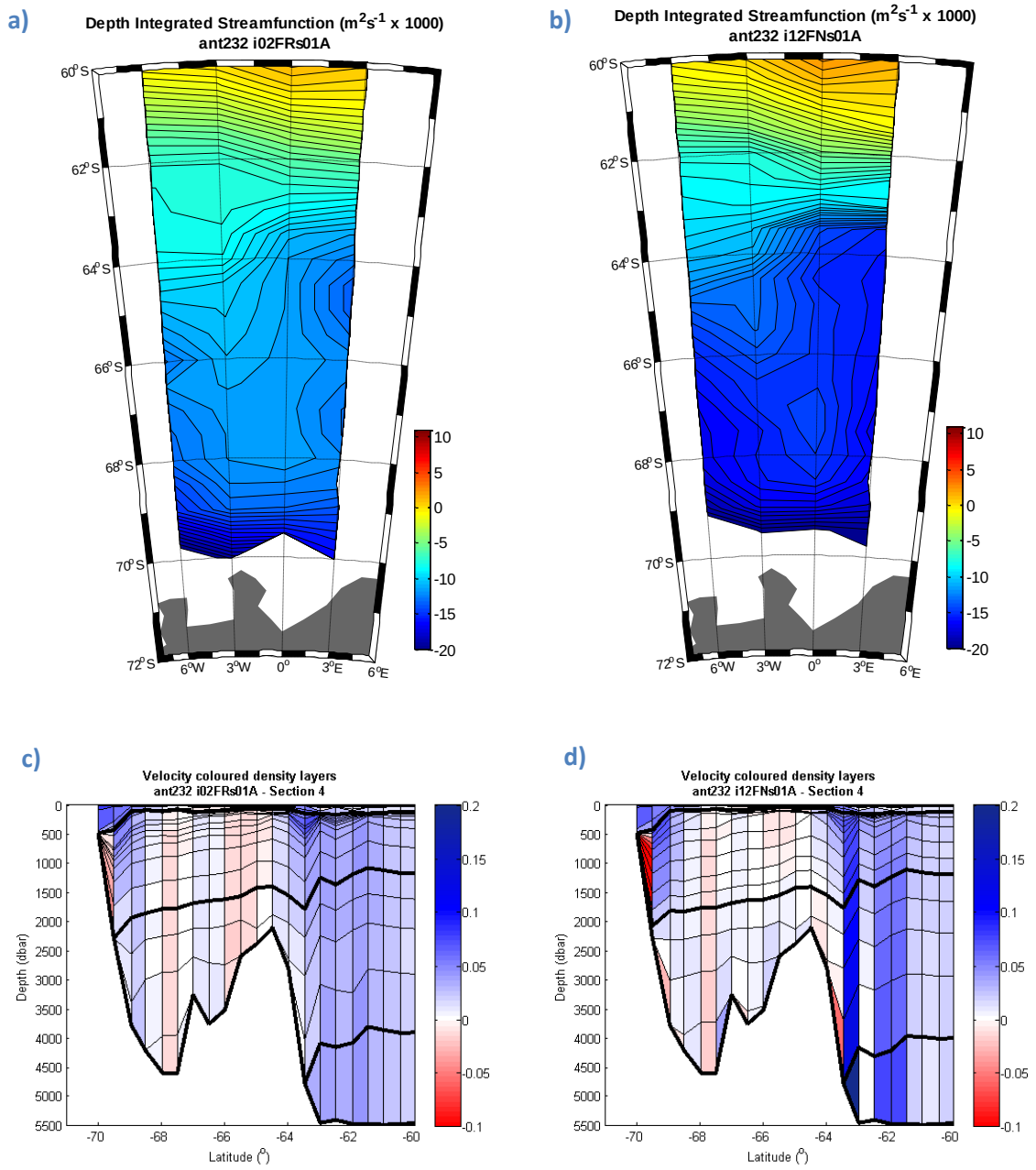

Figure 4.4.28 – Top: Stream functions of IMBAM solutions as in figure 4.4.1f for the *ANT-XXIII/2* cruise. Bottom: Corresponding velocity normal to each density layer face as calculated from IMBAM along the Greenwich Meridian. Density surfaces are defined by potential density a) & c) and Neutral Density b) & d).

4.4.3 Comparison of raw ADCP with stream function ADCP reference formats

As earlier described, the ADCP data was processed in two primary ways: a raw format which averages between stations along the cruise track and a stream function format which imposes a non-divergent flow based on the ADCP data and computes a velocity field accordingly. The latter additionally being used for examination of perturbed ADCP data. The raw format offers a more direct application of the ADCP data, however as can be seen in Figure 4.4.29 this produces a solution with extensive small-scale variability around individual stations and large transports between station pairs which are not covered by the VM-ADCP track. This gives rise to a flow pattern which is significantly different to the stream function format. It is therefore judged most appropriate to examine the stream function results (e.g. as in Figure 4.4.28) in detail and acknowledge the limitations of using the 'raw' ADCP data in this manner.

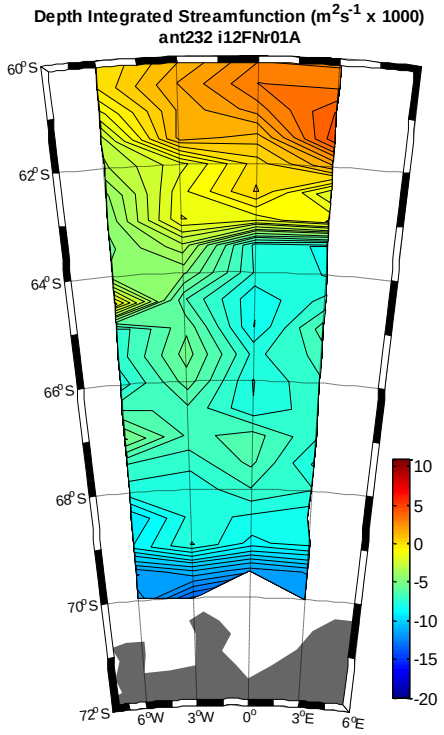

Figure 4.4.29 – Stream function of IMBAM solution as in Figure 4.4.27f for the *ANT-XXIII/2* cruise, using all five raw ADCP references levels together.

Nevertheless, the raw ADCP format does provide a solution with the key features of the jets to the north of Maud Rise and along the continental slope and decreased transport to the southwest of Maud Rise. Importantly, the raw format does seem to preserve some of the more rugged features that the stream function format processing smoothes. Thus it is worthwhile to consider that the smoothed solutions considered for further analysis may not fully account for variability between station pairs sufficiently to resolve small features at the scale of the station spacing.

4.4.4 Comparing total transports of the different VM-ADCP setups

In order to examine in detail the different solutions provided by using raw, stream function and perturbed VM-ADCP data, the westward total volume transports observed across the meridional sections for all cruises are shown in Figure 4.4.30. The first point to note is that whilst similar total transports for raw and stream function solutions are obtained for some sections in some cruises (e.g. *ANT-XXI/4* at 6^{o}W, 4^{o}W, 2^{o}W and the GM and deeper reference levels for *ANT-XXIII/6*), there are large discrepancies across most of the sections. As earlier indicated, this seems to be partially due to the lack of VM-ADCP coverage for many of the east-west orientated station pairs, and the effect appears most pronounced where there is the greatest absence of east-west station pairs along the domain boundary. However other factors may be at work, particularly within the Ekman layer, whereby variation in the atmospheric forcing over the duration of a cruise could lead to an overall VM-ADCP dataset which poorly represents the mean state of the ocean. This further justifies using a stream function approach for further analysis.

The next major observation is that the perturbed data – represented by blue circles in Figure 4.4.30 - result in solutions which are consistently similar with the non-perturbed stream functions. The non-perturbed stream function solutions are therefore considered reliable within the context of being only marginally influenced by ADCP error, although this likely reflects the result of processing the ADCP to obtain a divergence free reference stream function, rather than a reflection on the inverse solution itself.

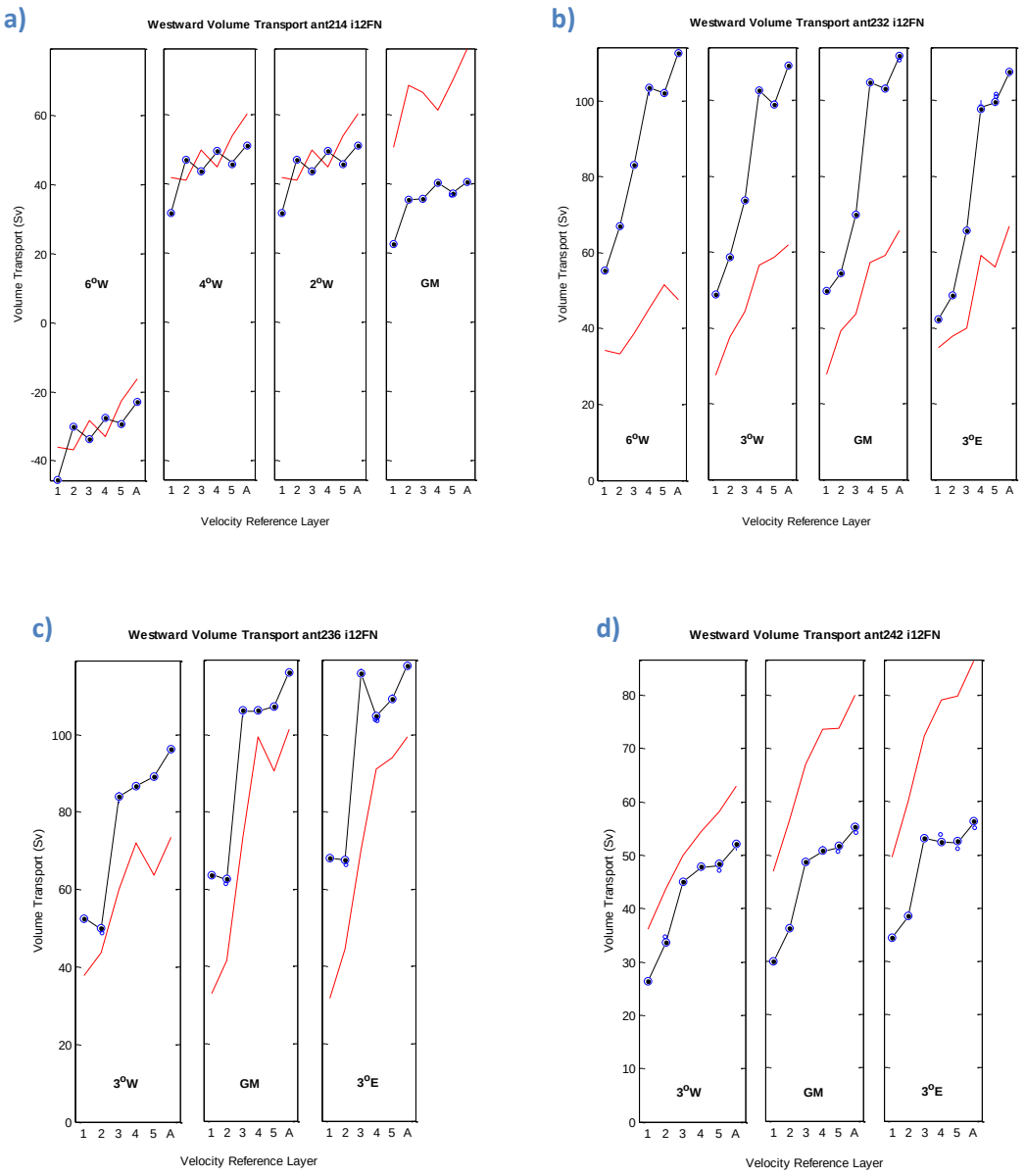

Figure 4.4.30 – Westward total volume transport for the full domain of a) ANT-XXI/4, b) ANT-XXIII/2, c) ANT-XXIII/6 & d) ANT-XXIV/2. Labels on the x-axis represent ADCP reference layers 1-5, and a model solution using all ADCP layers simultaneously (A). This is a summary of all model results using the raw ADCP data (red), stream function ADCP data (black) and variability associated with the perturbed ADCP stream functions (blue markers). Note the different scales for each subplot.

With respect to using different reference levels, total transport is consistently underestimated by up to 100% using only near surface ADCP layers, which is true of the raw and stream function ADCP data. The difference for ADCP reference layer 1 is easily explained as always being within the mixed layer and thus subject to the direct effect of atmospheric forcing. However, *ANT-XXIII/6* has the deepest mixed layer (mean depth 114m) which accounts for the low transport values provided by

using layers 1 and 2. In contrast, *ANT-XXIII/2* and *ANT-XXIV/2* have much shallower mixed layers (mean depth 23m and 19m respectively) and demonstrate a more gradual change from the lower estimates generated from layer 1 reference solutions through to the higher estimates generated from the layer 5 reference. Further detailed consideration of these results is discussed later in part 4.5.

4.4.5 Duplicate domains

To examine the impact of duplicating data, IMBAM was run in a quasi-2-dimensional set-up whereby single full-depth sections for each cruise – or near full depth in the case of *ANT-XXI/4* – are duplicated within the inverse matrix to enforce mass conservation. This also provides insight into the relationship of the results of the 3-dimensional set-up of IMBAM so far considered to estimates by other authors using only single-section techniques. The results shown in Figure 4.4.31 provide significantly different results to the full domain 3-dimensional set-up. For *ANT-XXI/4* the duplicate domain produces a transport using all reference levels which is 4 times larger than for the full domain; for *ANT-XXIII/2* the transport is ~60% larger; and for *ANT-XXIII/6* the transport is only ~15% larger.

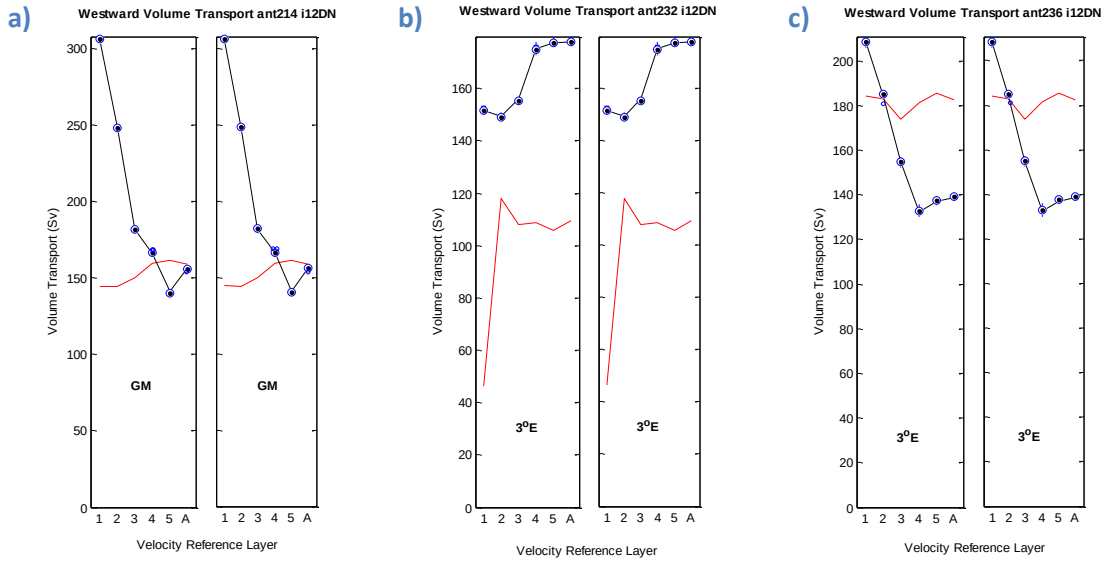

Figure 4.4.31 – Westward total volume transport for the duplicate domain of a) ANT-XXI/4, b) ANT-XXIII/2 and c) ANT-XXIII/6, as in Figure 4.4.30.

There are two broad ways to consider these results. Firstly, that the IMBAM technique is inappropriate in the 2-dimensional set-up without further assessing the weighting of using duplicated data. To fill gaps in the CTD grid, some stations were also duplicated in the full domain set-ups, and thus this leads to concern that this approach may apportion too much importance to the duplicated data. When comparing the level 1 reference solutions of *ANT-XXI/4* and *ANT-XXIII/6* in Figure 4.4.30 and Figure 4.4.31, which produce transports in excess of 200 Sv for the duplicate domain, it is clear that there is no apparent consistency between the 2-dimensional and 3-dimensional solutions. Secondly that using a 2-dimensional single section approach fails – by definition – to consider the 3-dimensional impacts of the isopycnal structure of the ocean and that the IMBAM 2-dimensional solutions reflect this, resulting from the available hydrographic data.

4.4.6 Summary of model development

The Inverse Multi-Box Adaptable Model (IMBAM) was developed to obtain solutions for the volume transport across the Lazarev Sea using isopycnal surfaces and VM-ADCP velocity referencing. From the results examined so far the preferred options for examining model solutions in detail were established. Firstly, the evidence supports the logical inference that making use of all available reference levels produces the most credible results without any apparent weighting bias from multiple reference values. Next, although already presumed, the density classes are best represented by Neutral Density, and not potential density, owing to significantly different total volume transports despite similar patterns of flow.

The VM-ADCP data could seemingly be used to obtain a valid solution in either a raw or stream function format, however the absence of a fully closed domain boundary seems to present a problem with the raw format in allowing transport through non-referenced and thus non-constrained open boundaries. The raw ADCP data also suffers from points being close in space but far apart in time leading to excessive divergences. Therefore using the stream function ADCP reference velocities is preferred. Perturbing the ADCP data by a random fraction of the associated error for this

purpose has a minimal effect on the model solutions and can therefore be considered a minimal source of error within the context of the model inversion.

Lastly, the examination of the 2-dimensional duplicate domain solutions cast doubt on the validity of duplicating data, and the 2-dimensional set-up in particular has little value for direct comparison with the methods of other authors. However, these considerations do not suggest that the 3-dimensional full domain solutions are invalid, merely that the model has demonstrated a low level of skills with respect to the quasi-2-dimensional problem without further development.

4.4.7 Examining the results of the model output

ANT-XXI/4

The total volume transport for the solution for *ANT-XXI/4* in Figure 4.4.32 shows a south-westerward flow south of 63°S in the northeast corner of the domain, whilst further south there is a region of high westward transport between 64°S and 66°S. Both features are co-located with the northern flank of Maud Rise which is to the east of the cruise domain. Further south, between 68°S and the Antarctic continent dominates another area of westward transport, although this is weaker than the flow further to the north. Between these two regions there is southward flow between the Greenwich Meridian and 2°W, with an area of slack flow to the west of 2°W. At the extreme south-west of the domain near the continental slope a region of intense eastward flow exists. This apparent oddity is associated with the complicated flow over the continental slope shown in Figure 4.2.17.

The same broad patterns of flow are evident in the water mass transport stream functions shown in Figure 4.4.33 although there are some noticeable differences. In the AASW there is a meander in the flow between 67°S and 69°S in the area of slack flow and there is evidence of off-shelf transport near the Antarctic continent in the southwest of the domain due to the opposing flows to the west and east of 4°W.

In the WDW layer (Figure 4.4.33b) there is an absence of an obvious slack region between 66°S and 68°S. The origin of the strong easterward transport is evident along the continental shelf.

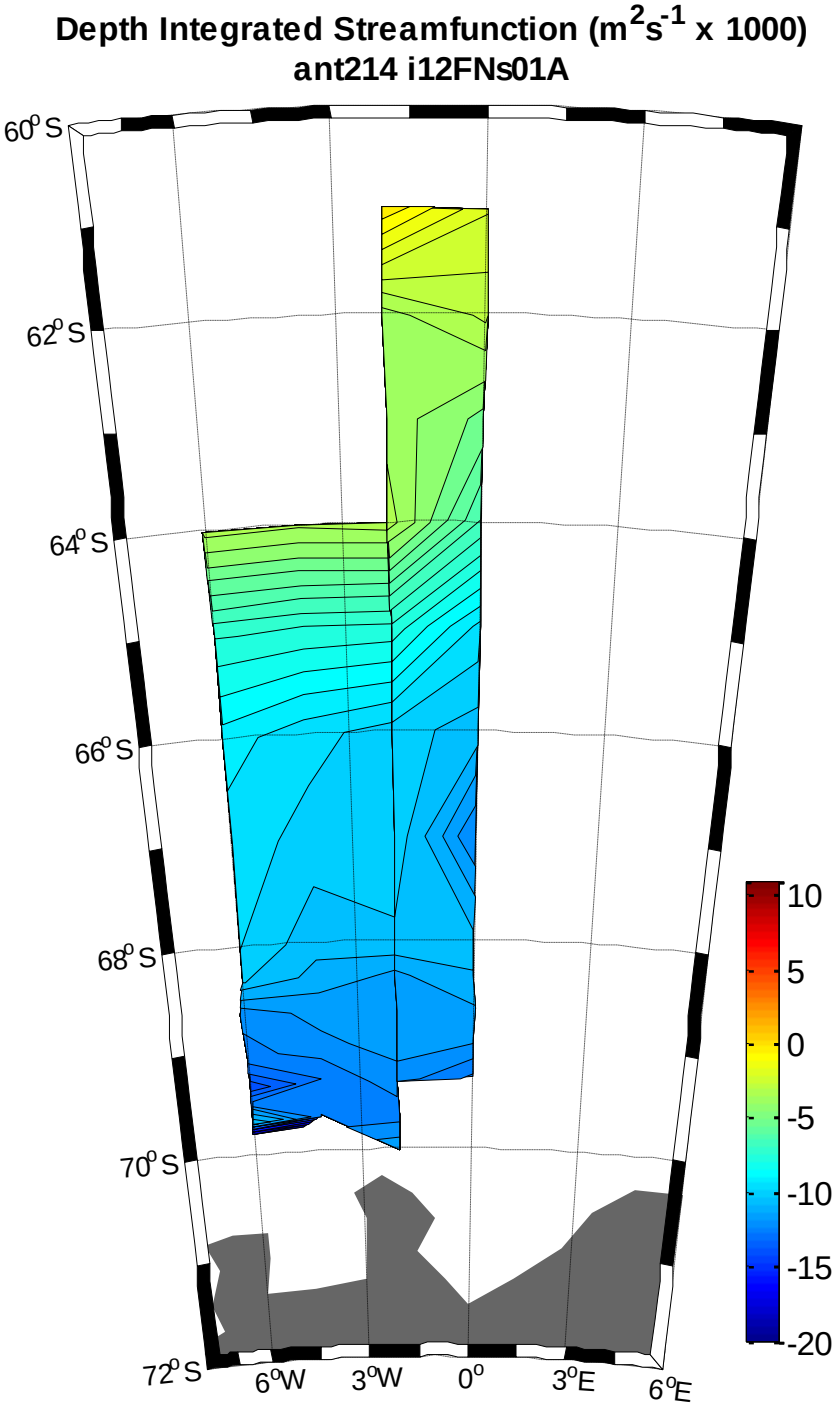

Figure 4.4.32 – Full-depth stream function of the full-domain IMBAM solution for the *ANT-XXI/4* cruise, as in Figure 4.4.27f.

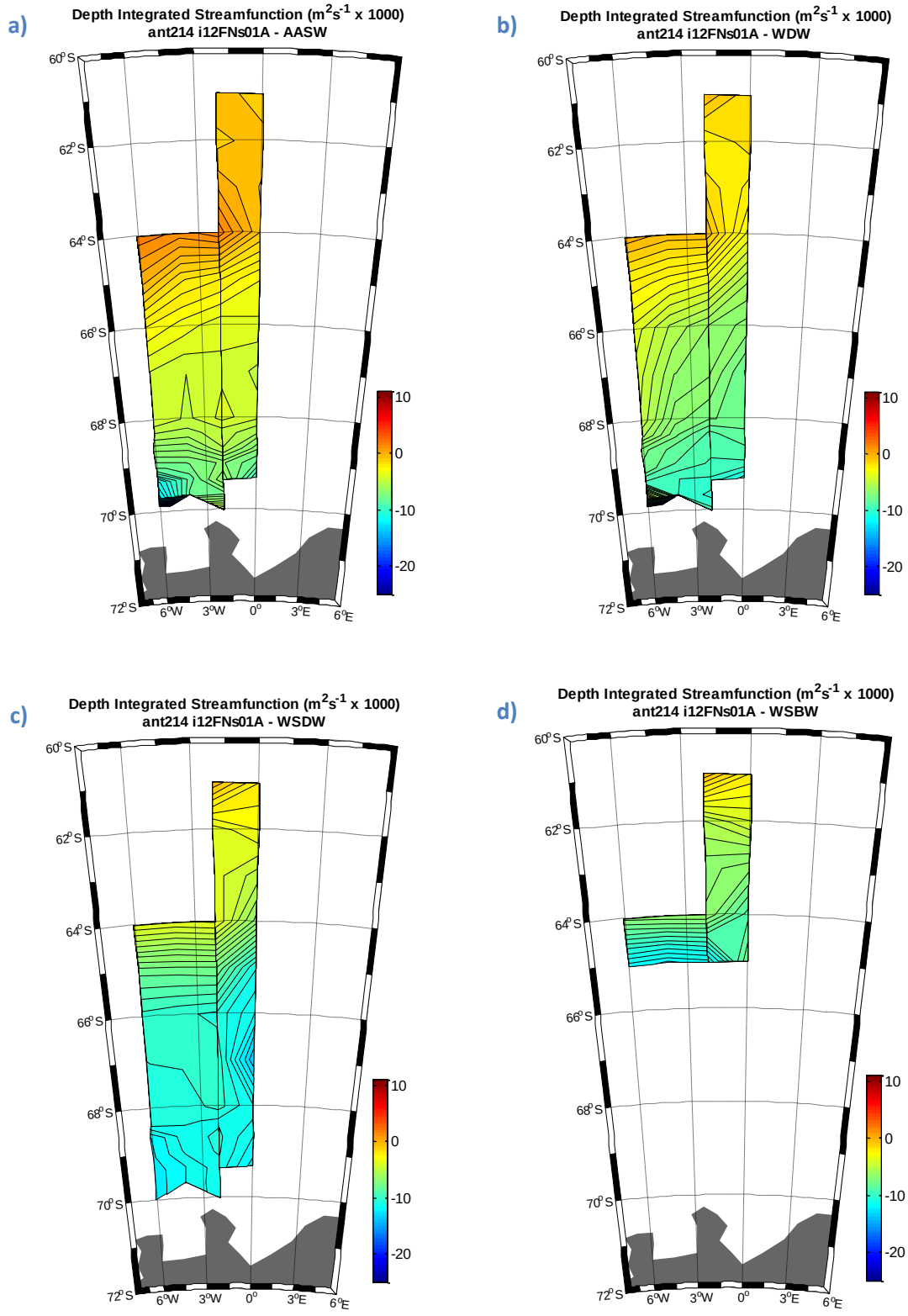

Figure 4.4.33 – Water mass specific stream functions of full-domain IMBAM solution for the *ANT-XXI/4* cruise. The individual water mass volume transport is divided by the corresponding station-by-station water mass layer thickness for a) AASW, b) WDW, c) WSDW and d) WSBW. Computed using the Neutral Density set-up and all the stream function ADCP reference levels together.

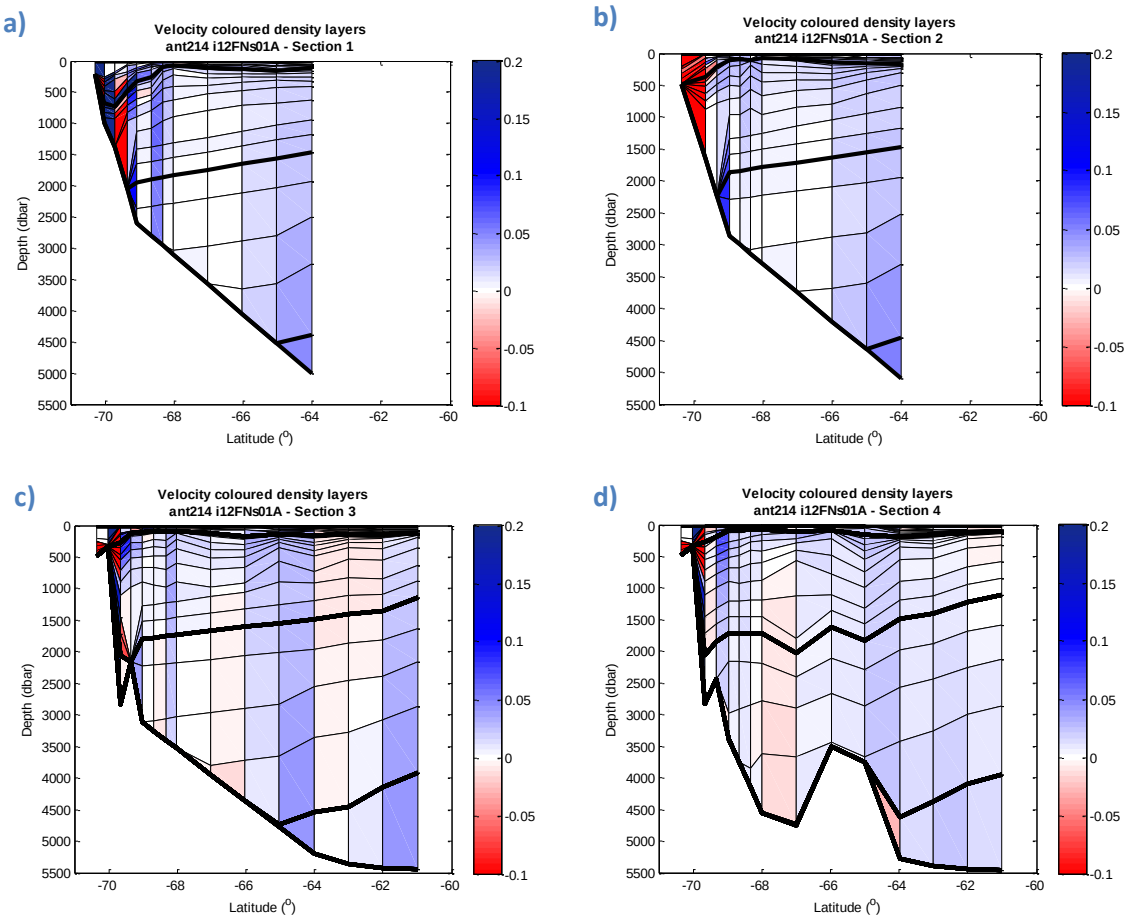

Figure 4.4.34 – Sections of velocity for IMBAM solution for the ANT-XXI/4 cruise, as in Figure 4.4.32, along a) 6°W, b) 4°W, c) 2°W d) the Greenwich Meridian. Westward transport is positive (blue) and eastward transport is negative (red).

Table 4.4.6 – Westward volume transport contributions from the different water masses across each north-south section for ANT-XXI/4 full domain as in Figure 4.4.32

Transport (Sv)	***Section 1: 6°W***	***Section 2: 4°W***	***Section 3: 2°W***	***Section 4: 0°***
Full Depth	32.9	37.9	56.9	46.3
AASW	3.5	1.1	1.1	1.0
WDW	7.4	14.4	15.0	13.5
WSDW	20.5	20.6	30.3	24.6
WSBW	1.5	1.8	10.4	7.2

The slack region is evident in the WSDW (Figure 4.4.33c) with the feature centred on 67°S, 4°W. Also in the WSDW, centred on 68.6°S, 2°W exists a small cyclonic recirculation which is masked in the total volume stream function in Figure 4.4.32. The WSBW transport is limited to westward transport north of Maud Rise, with any further detail to the west omitted due to the scarcity of full-depth CTD stations.

The sections of westward velocity in Figure 4.4.34 show that westward flow dominates in all the sections with the highest westward velocities on the northern flank of Maud Rise and over the continental slope. However, eastward flow does occur north of Maud Rise between 62°S and 64°S along 2°W, whilst there is a strong eastward flow in the WSBW in contact with the northern flank along the Greenwich Meridian. Weaker eastward flows occur south of the rise between 66°S and 67°S along 2°W and between 67°S and 68°S on the Greenwich Meridian. There is a consistently complicated set of reversing eastward and westward flows over the continental slope at all longitudes.

Table 4.4.6 summarised the total westward transports for each water mass, showing a net westward transport for each. The WSDW accounts for between 53-62% of the total transport for each section, with a more variable contribution from the WDW of 22-38%, whilst the WSBW accounts for 5-18% and the AASW accounts for just 2-11%. The breadth of this variability is linked to the absence of data in the northwest of the domain.

ANT-XXIII/2

Westward transport dominates most of the *ANT-XXIII/2* full-domain solution shown in Figure 4.4.35. Starting from the north of the domain, there is a strong westward flow extending to about 62°S, with an intervening lower transport up to ~63°S, where the flow then re-intensifies along the northern slope of Maud Rise and meanders further south in the western sections. South of Maud Rise the flow meanders in a southward direction before turning westwards again, parallel with the strong flows associated with the continental slope at around 69°S. The region of slack flow between Maud Rise and the continent includes an apparent recirculation centred on 67°S on the Greenwich Meridian.

The stream functions in Figure 4.4.36 shows that each water mass has a noticeably varying flow structure to each of other water masses. The AASW (Figure 4.4.36a) follows the same broad structure of flow as the full depth stream function, although the aforementioned recirculation at 67°S is not evident whilst the eastern edge of a recirculation feature – either an eddy of a meander – can be seen between 63°S and 64°S along 6°W. Flow is particularly strong along the continental slope.

The WDW (Figure 4.4.36b) exhibits a structure largely identical to the full depth stream function, with evidence of a recirculation or very low flow region centred on 67°S on the Greenwich Meridian. This feature is clearly seen in the WSDW (Figure 4.4.36c). A pair of recirculation features are also present along the northern slope of Maud Rise centred on 62°S, 1.5°E and atop of Maud Rise between 64.5°S and 65°S, along 3°E. In the WSDW the Maud Rise flow is comparatively more intense than that associated with the continental slope.

Figure 4.4.36d shows the WSBW for *ANT-XXIII/2* demonstrating how the deep bathymetry allows for the existence of WSBW flow to the west of Maud Rise, which meanders first south, then west, then north around 65°S, 3°W. Intense flow is present at the base of the rise.

These patterns are well reflected in Figure 4.4.37 where strong westward flows are observed to the north (c & d) and to the west (a & b) of Maud Rise, whilst there is a consistent strong flow along the continental slope. Three notable eastward transports can be identified: at the base of the WSDW on the northern flank of Maud Rise along 3°E; the general minor eastward flow between ~64.5°S and 68°S associated with the southward meandering of the flow; and a strong counter-current in the WDW on the continental slope along 3°E.

Across the four sections the WSDW accounts for 45-51% of the total zonal transport, with the WDW accounting for 25-31%, WSBW accounting for 14-20% and the AASW for 3-8% of the transport (see Table 4.4.7). These are broadly similar to those estimates for *ANT-XXI/4*, although overall percentage contribution of the WSDW is less dominant.

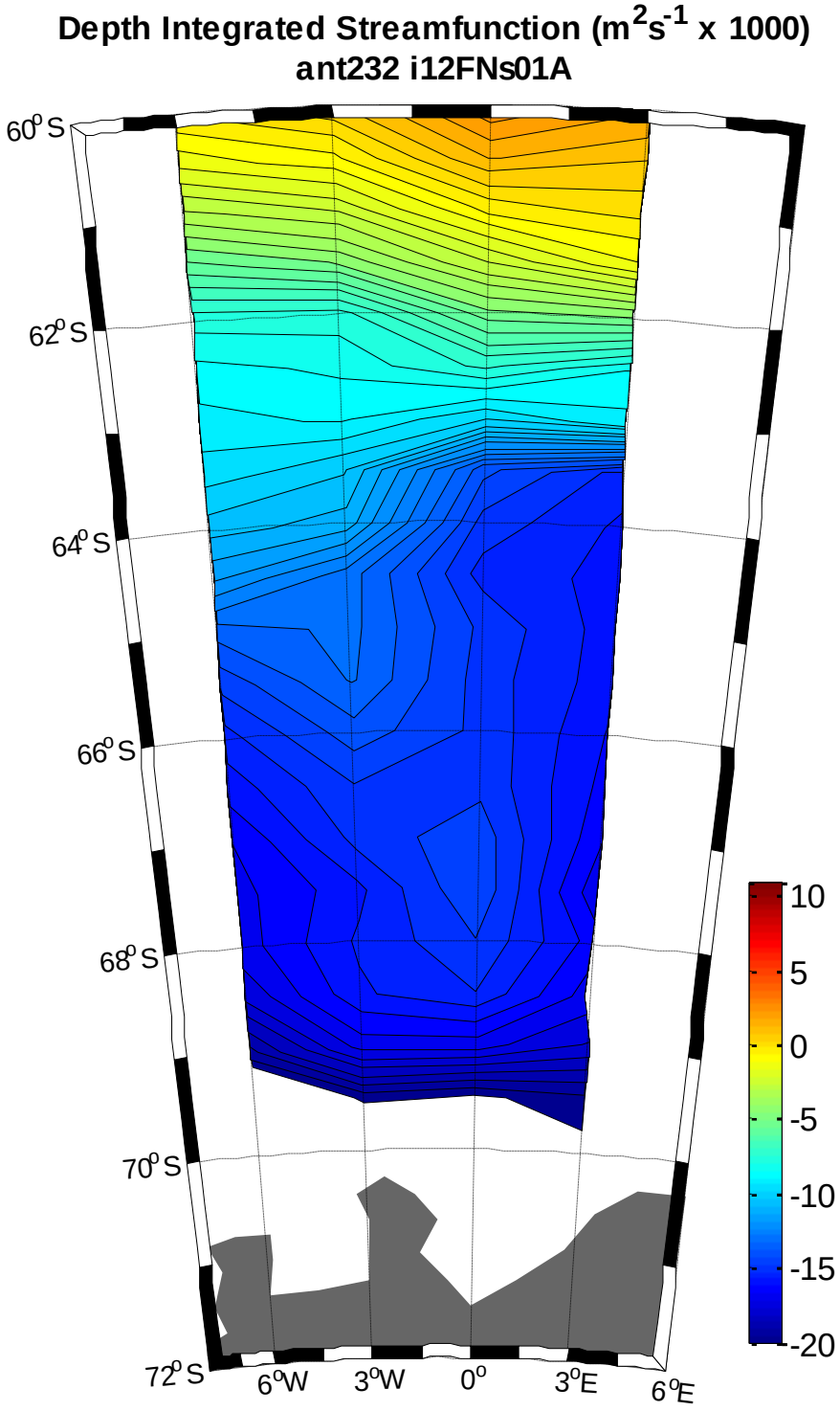

Figure 4.4.35 - Full-depth stream function of the full-domain IMBAM solution for the *ANT-XXIII/2* cruise, as in Figure 4.4.27f.

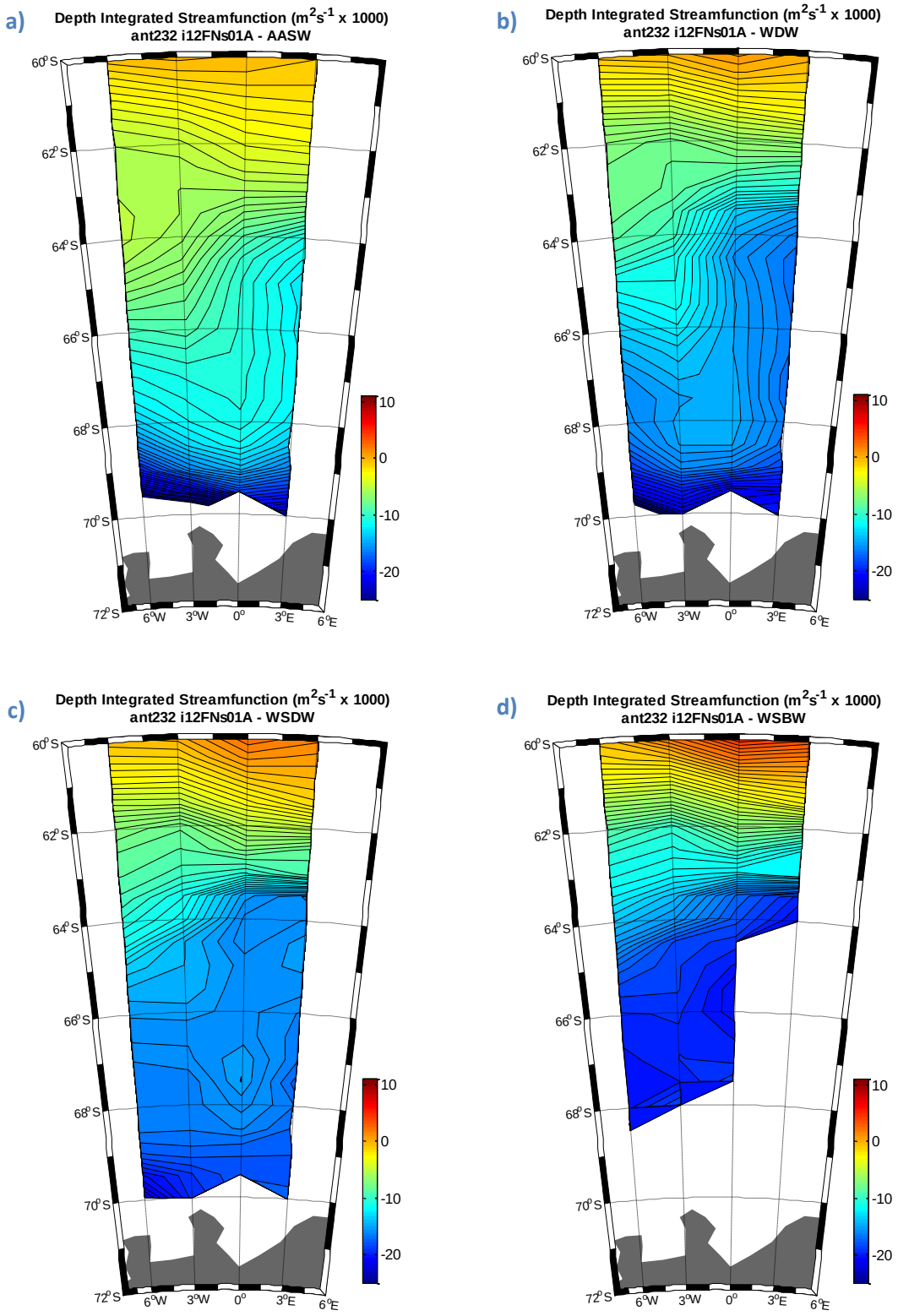

Figure 4.4.36 – Water mass specific stream functions of full-domain IMBAM solution for the *ANT-XXIII/2* cruise, as in Figure 4.4.33

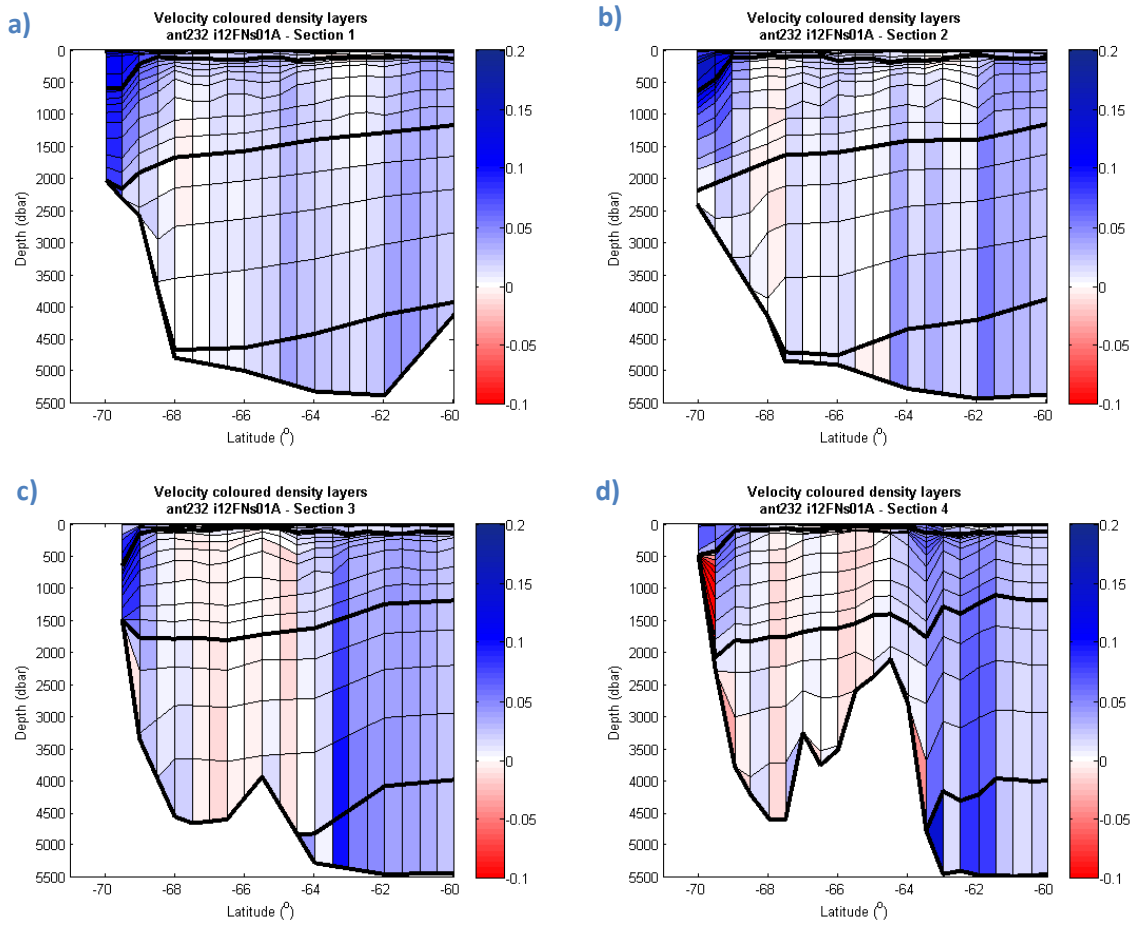

Figure 4.4.37 – Sections of velocity for IMBAM solution for the ANT-XXIII/2 cruise, as in Figure 4.4.35, along a) 6°W, b) 3°W, c) the Greenwich Meridian and d) 3°E. Westward transport is positive (blue) and eastward transport is negative (red).

Table 4.4.7 – Westward volume transport contributions from the different water masses across each north-south section for ANT-XXIII/2 full domain as in Figure 4.4.35

Transport (Sv)	***Section 1: 6°W***	***Section 2: 3°W***	***Section 3: 0°***	***Section 4: 3°E***
Full Depth	112.7	109.3	111.6	107.3
AASW	8.2	8.2	3.7	4.6
WDW	38.5	32.0	28.3	27.3
WSDW	50.2	51.0	57.1	54.6
WSBW	15.9	18.1	22.5	20.9

ANT-XXIII/6

The *ANT-XXIII/6* domain covers only 6° of longitude, but a near identical latitudinal range to *ANT-XXIII/2* as well as a co-located full-depth section along 3°E, and the two therefore offer the best source of comparison of the LaKriS cruises. Westward flow is again dominating (Figure 4.4.38), with a west-north-westward flow north of 63°S culminating in a notable flow out of the north of the

domain. A region of high transport corresponds to the northern flank of Maud Rise at ~63°S, whilst further south there is a sizeable meander with a recirculation in the middle centred on 65°S on the Greenwich Meridian. Observations of the water masses will show this to be an artefact of the full depth transport calculation and not a coherent feature present at any of the different layers. To the southwest of this is a region of southward flow which links up with the westward flow associated with the continental slope between 67°S and 69.3°S. There is a meandering of this slope current in the southeast of the domain.

Unlike the two previous cruises, *ANT-XXIII/6* has a markedly different circulation of AASW compared to the deeper water masses. Figure 4.4.39a shows a north-westward transport north of 64°S, 3°E and 62°S, 3°W. There is an anti-cyclonic flow centred on 62.5°S, 3°W and a cyclonic flow to the south centred on 64.5°S, 3°W. A region of slack flow exists centred on 64°S on the Greenwich Meridian, which is to the immediate west of Maud Rise. This structure may be the result of eddies being shed from atop Maud Rise akin to that described by de Steur et al. (2007). Further south the pattern of flow is again westward, but in the case of this cruise westward flow dominates between 66°S and 68°S with an absence of largely southward flow near 3°E, which is observed for *ANT-XXIII/2*. The pattern is instead south-westward. This reinforces the observations made in section 4.4.4 about the solution obtained using only one or the other of the upper two ADCP reference levels for this cruise being unrepresentative of the deep ocean: the surface circulation may be largely disconnected from the deep circulation.

The WDW also shows a very different pattern of flow in Figure 4.4.39b, where a north-westward flow dominates in the north of the domain, which is intensified near the northern flank of Maud Rise. Between 64°S and 67°S there is a region of slack flow, with evidence of a long meander centred around 65°S on the Greenwich Meridian. Further south, strong westward flow resumes. This pattern is largely replicated in the WSDW (Figure 4.4.39c) although the central region of slack flow includes a small but relatively intense anti-cyclonic recirculation around the top of Maud Rise centred on 65°S, 3°E; as well as weaker cyclonic circulation further to the south centred on 66°S, 3°E.

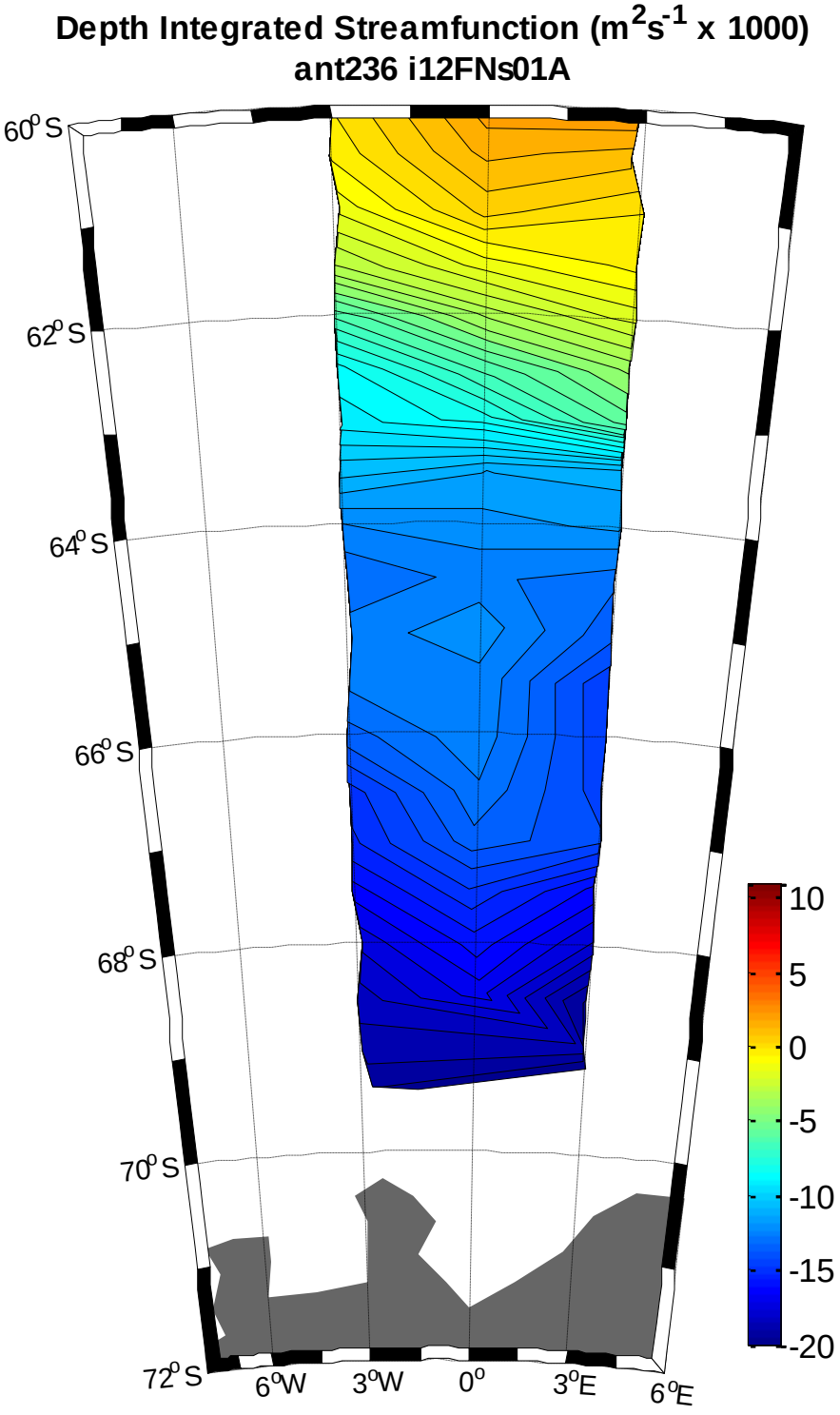

Figure 4.4.38 - Full-depth stream function of the full-domain IMBAM solution for the *ANT-XXIII/6* cruise, as in Figure 4.4.27f.

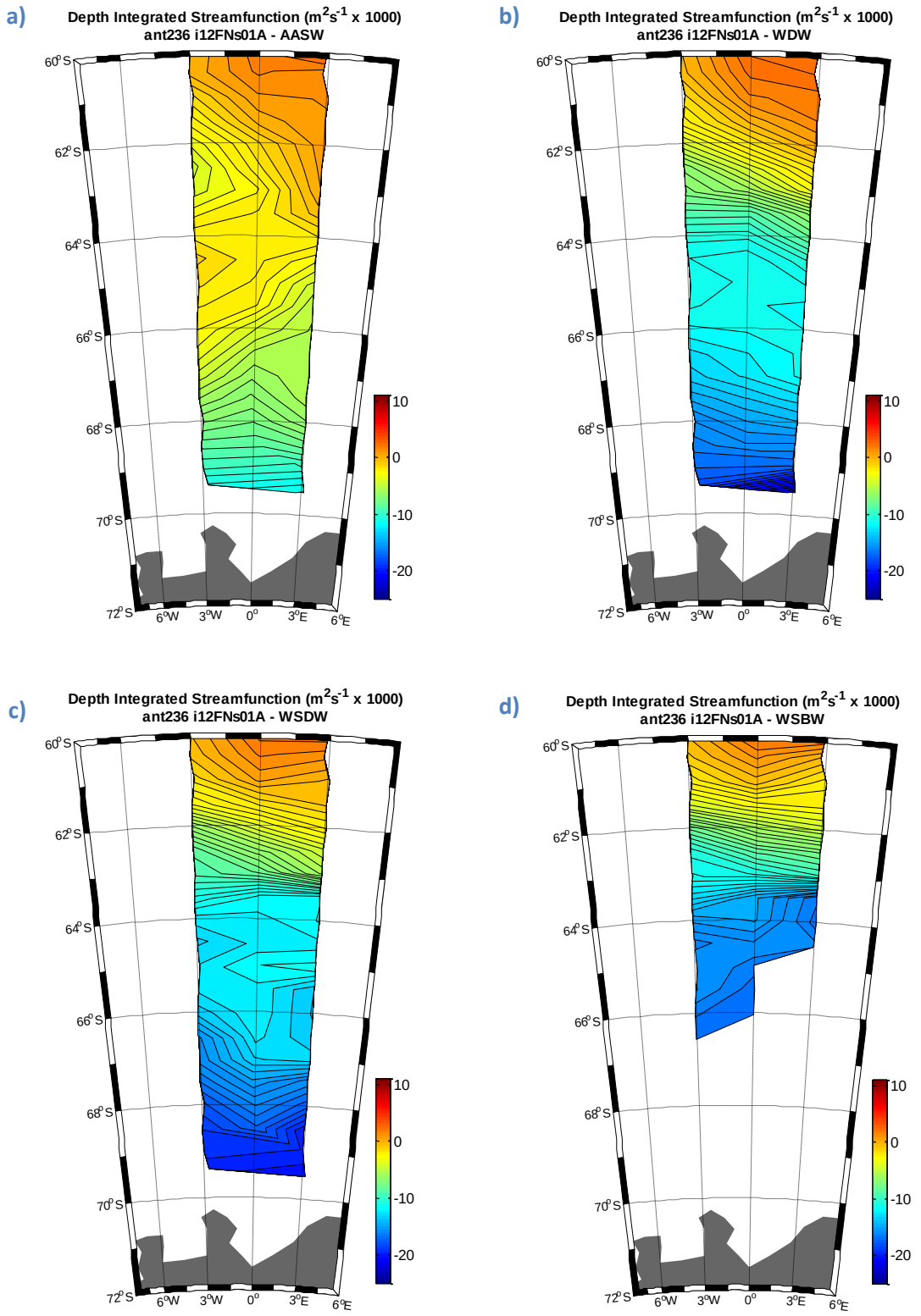

Figure 4.4.39 – Water mass specific stream functions of full-domain IMBAM solution for the *ANT-XXIII/6* cruise, as in Figure 4.4.33

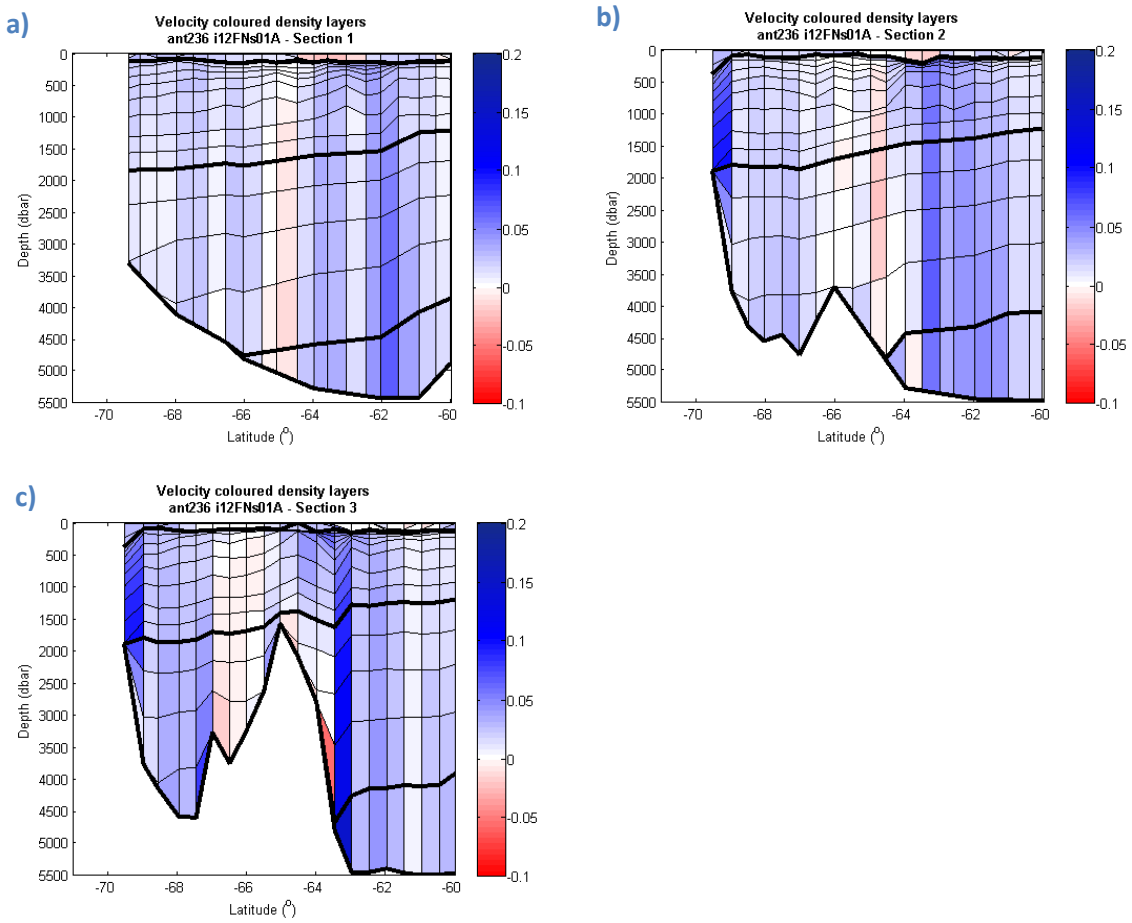

Figure 4.4.40 – Sections of velocity for IMBAM solution for the ANT-XXIII/6 cruise, as in Figure 4.4.38, along a) 3°W, b) the Greenwich Meridian and c) 3°E. Westward transport is positive (blue) and eastward transport is negative (red).

Table 4.4.8 – Westward volume transport contributions from the different water masses across each north-south section for ANT-XXIII/6 full domain as in Figure 4.4.38

Transport (Sv)	***Section 1: 3°W***	***Section 2: 0°***	***Section 3: 3°E***
Full Depth	96.3	116.2	118.0
AASW	1.4	1.7	1.9
WDW	26.2	36.7	37.4
WSDW	53.2	59.8	60.5
WSBW	15.5	18.0	18.3

The meandering of the slope current observed in Figure 4.4.38 appears to originate from the WSDW flow. The WSBW is largely dominated by westward flow, although a recirculation along the deep northern flank of Maud Rise is observed.

The velocity sections in Figure 4.4.40 illustrate this broad westward flow, with the only eastward reversals associated with the meander to the west of Maud Rise. The aforementioned

WSBW reversal on the northern flank of Maud Rise is not evident in the figure as it is a very thin layer; however the overlying WSDW illustrates the impact of the bathymetry in Figure 4.4.39c.

Owing to the seemingly more zonally dominated flow during this cruise, the variability of the water mass transport from section to section is lower with WSDW dominating 51-55% of the transport, WDW contributing 27-32%, WSBW 15-16% and AASW just 1-2% of the transport.

ANT-XXIV/2

The final LaKriS cruise, *ANT-XXIV/2*, is the least extensively surveyed of the four cruises. The total transport stream function solution shown in Figure 4.4.41 is similar in some respects to that of *ANT-XXIII/6* in that it has a predominantly east-west flow with a mid-latitude region of slack flow. The poor sampling in the south of the domain presents challenges for interpreting the circulation in this area.

The circulation of the AASW shown in Figure 4.4.42a is dominated by westward flow in the north of the domain with a heavily meandering structure in the south of the domain and a strong eastward flow around 70^{o}S. The WDW stands in contrast, with strong westward flow in the extreme north of the domain, a meandering slack region of flow between 63.5^{o}S and 65^{o}S, and a return to westward flow further to the south. Again, the south of the domain presents a difficult picture to interpret, but seems to suggest transport of WDW towards the continental slope south of 69.5^{o}S.

The WSDW is more complicated. Again, in Figure 4.4.42c, westward flow dominates in the extreme north of the domain, with a counter current apparent along 63.5^{o}S and a cyclonic circulation centred over Maud Rise at 64.5^{o}S, 3^{o}E. Further west there is a hint of a cyclonic feature centred on 64^{o}S, 3^{o}W, possibly the edge of an eddy shed from the rise. Between 65^{-o}S and 67.5^{o}S the flow meanders first south-westward and then north-westward, and south of this is a band of westward flow. There appears to be some small features between 68^{o}S and 68.5^{o}S deflecting the flow further southward. The WSBW moves westward (Figure 4.4.42d), with a meander to the southwest of the

rise following the bathymetry.

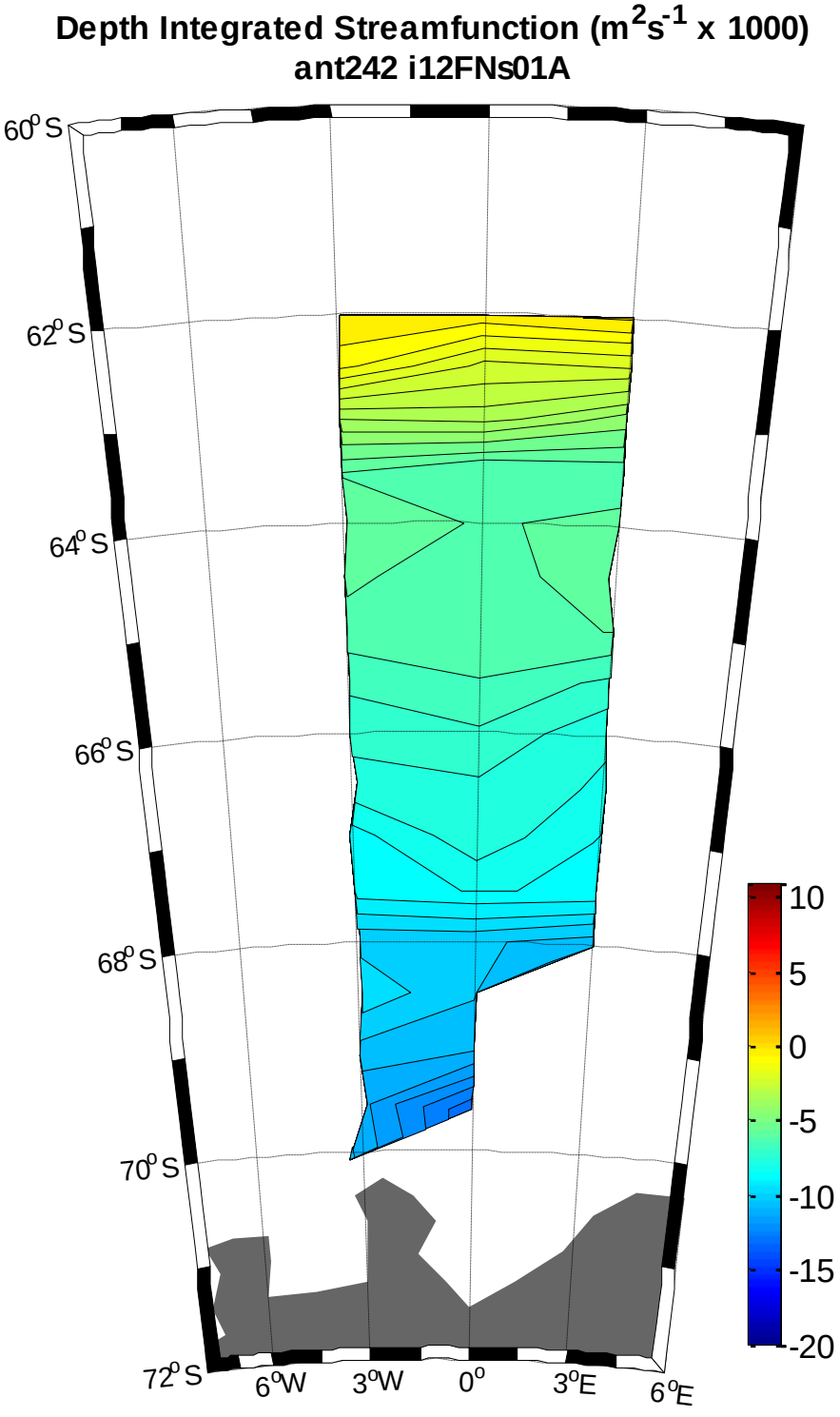

Figure 4.4.41 - Full-depth stream function of the full-domain IMBAM solution for the *ANT-XXIV/2* cruise, as in Figure 4.4.27f.

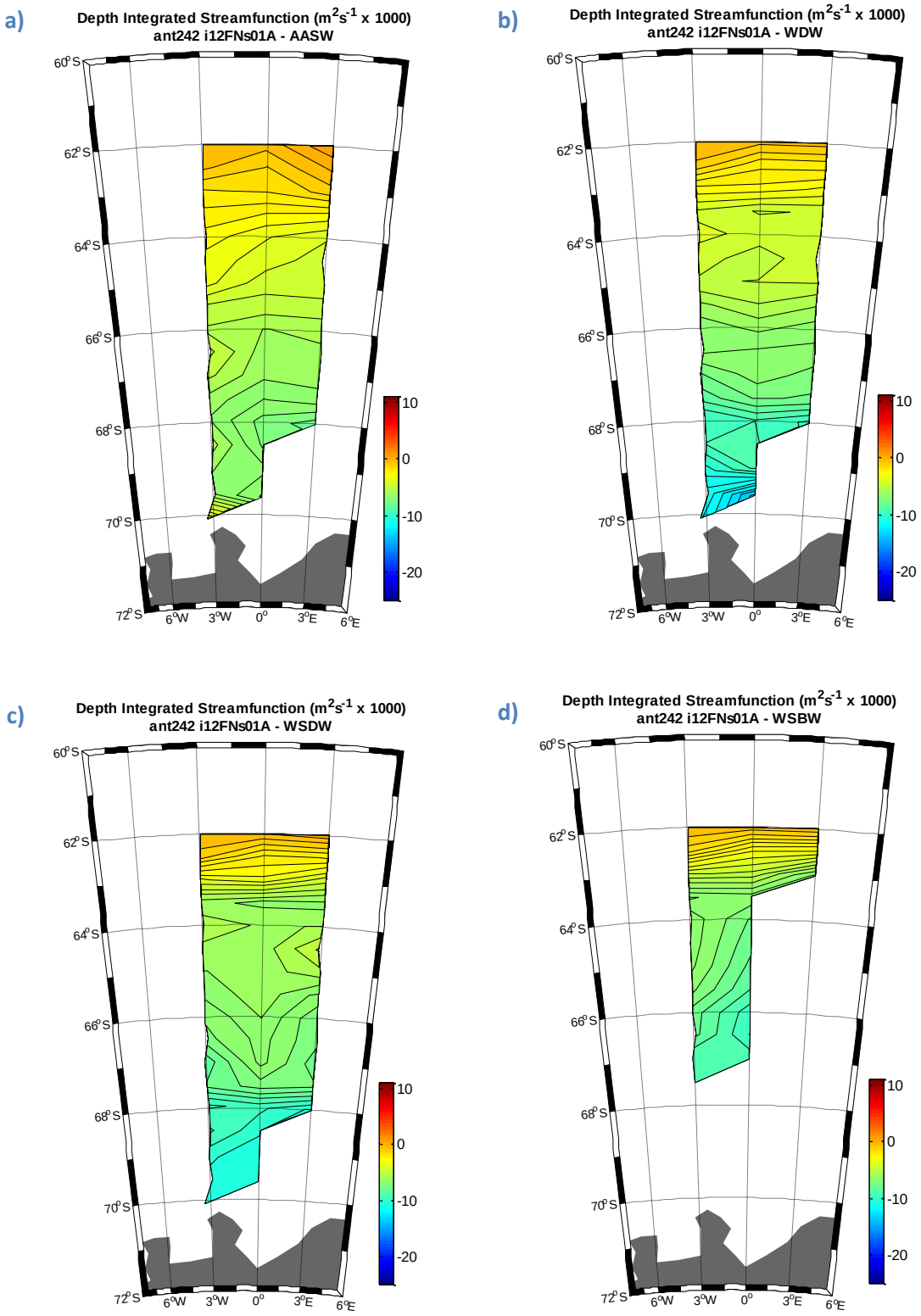

Figure 4.4.42 – Water mass specific stream functions of full-domain IMBAM solution for the *ANT-XXIV/2* cruise, as in Figure 4.4.33

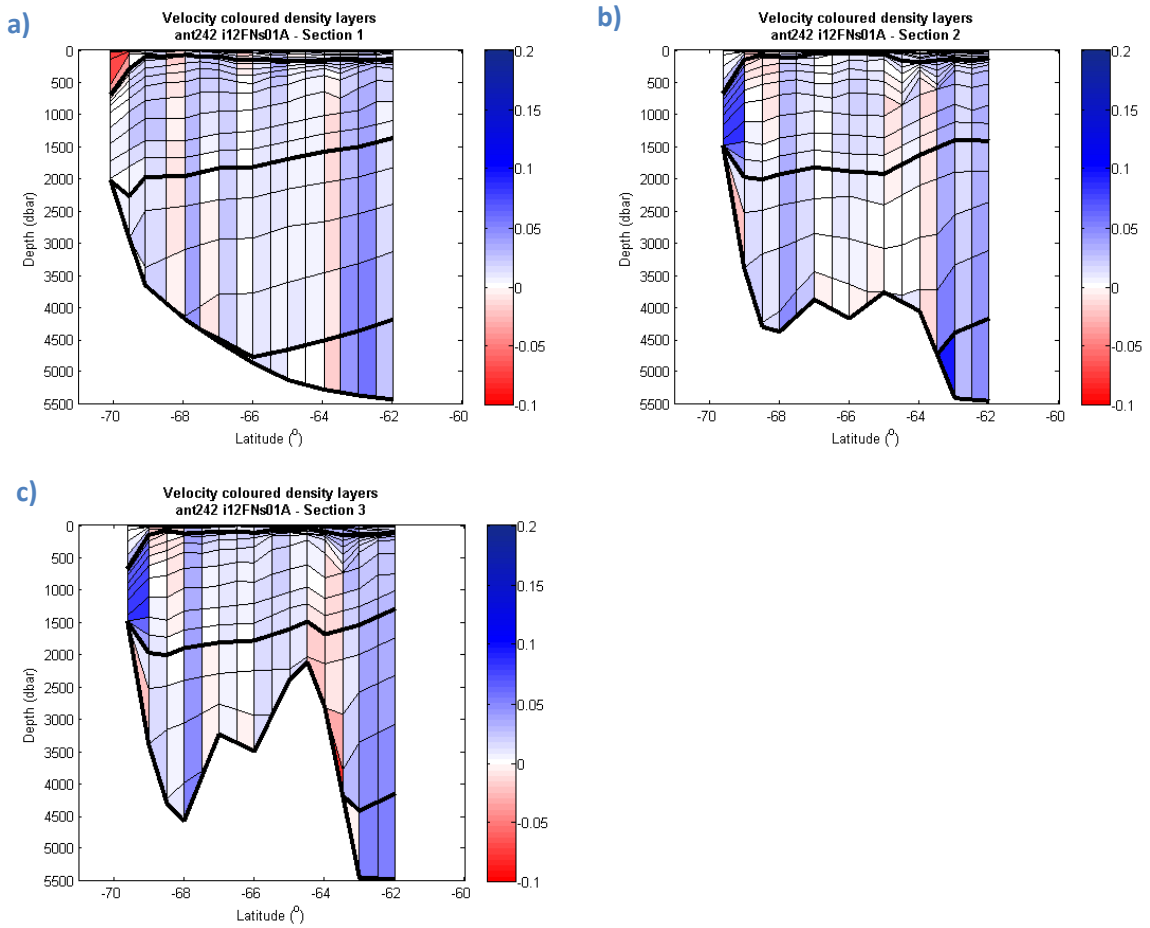

Figure 4.4.43 – Sections of velocity for IMBAM solution for the ANT-XXIV/2 cruise, as in Figure 4.4.35, along a) 3°W, b) the Greenwich Meridian and c) 3°E. Westward transport is positive (blue) and eastward transport is negative (red).

Table 4.4.9 - Westward volume transport contributions from the different water masses across each north-south section for ANT-XXIV/2 full domain as in Figure 4.4.41

Transport (Sv)	***Section 1: 3°W***	***Section 2: 0°***	***Section 3: 3°E***
Full Depth	51.8	54.9	56.0
AASW	-0.7	1.1	1.3
WDW	18.0	19.6	19.6
WSDW	27.4	27.3	28.1
WSBW	7.1	6.9	7.1

The velocity sections are patchier than in the other cruises (Figure 4.4.43). The westward flow north of Maud Rise is evident in all the sections, whilst the reversal of flow along the northern slope of the rise is evident to varying extents across different density ranges. South of the latitude of Maud Rise, eastward or slack flow appears to dominate at depth whilst westward flow is more prominent in the AASW and WDW. The slope currents at the Greenwich Meridian (Figure 4.4.43b) and 3°E (Figure 4.4.43c) are prominent within the WDW, whilst the AASW has low westward flow.

The situation is different along 3°W (Figure 4.4.43a) where the AASW flow strongly eastward, and the WDW experiences a much weaker westward flow.

ANT-XXIV/6 is similar to *ANT-XXIII/2* in another respect: the range of percentage contributions from water masses to the overall transport is also small. The WSDW dominates at a consistent 50-53%, the WDW a slim range of 35-36%, the WSBW 13-14% and the AASW 1-2% of the overall transport. This reflects the dominance of the westward flow and the minimal northward or southward transport out of the domain. However, given that the Greenwich Meridian was surveyed last out of the three sections, it is possible that this temporal discontinuity is responsible for the calculated flow fields.

ANT-XXIII/2 – subset domain

To examine the robustness of the model with respect to data coverage and thus the validity of the solutions for less well populated domains a model solution was obtained for *ANT-XXIII/2* using only those stations sampled in the same approximate positions as *ANT-XXIV/2*. The total transport of the solution for this set-up shown in Figure 4.4.44 is remarkably similar to that shown in Figure 4.4.35, with strong westward flow north of 63.5°S, a strong southward meander of the flow between 64°S and 69°S and a recirculation feature centred on 67°S on the Greenwich Meridian. Notably the strong westward flow along the continental slope is absent.

Interestingly this pattern is similarly present in all the water mass stream functions in Figure 4.4.45: other than in the WDW, the strong westward flow along the continental slope is mostly absent. At this point it should be noted that not only were the CTD stations restricted to the *ANT-XXIV/2* domain, but so were the ADCP reference stream functions which were calculated only as far south as 68°S. This suggests that the ADCP reference velocities have a leading role in determining the velocity structure which is insufficiently resolved by links to the rest of the domain by mass conservation alone. This has consequences for the solutions which will be later discussed. The impacts of this lack of southern referencing can be seen in decreased velocities (Figure 4.4.46) particularly in the south of the domain, although differences in intensity are noticeable as far north as

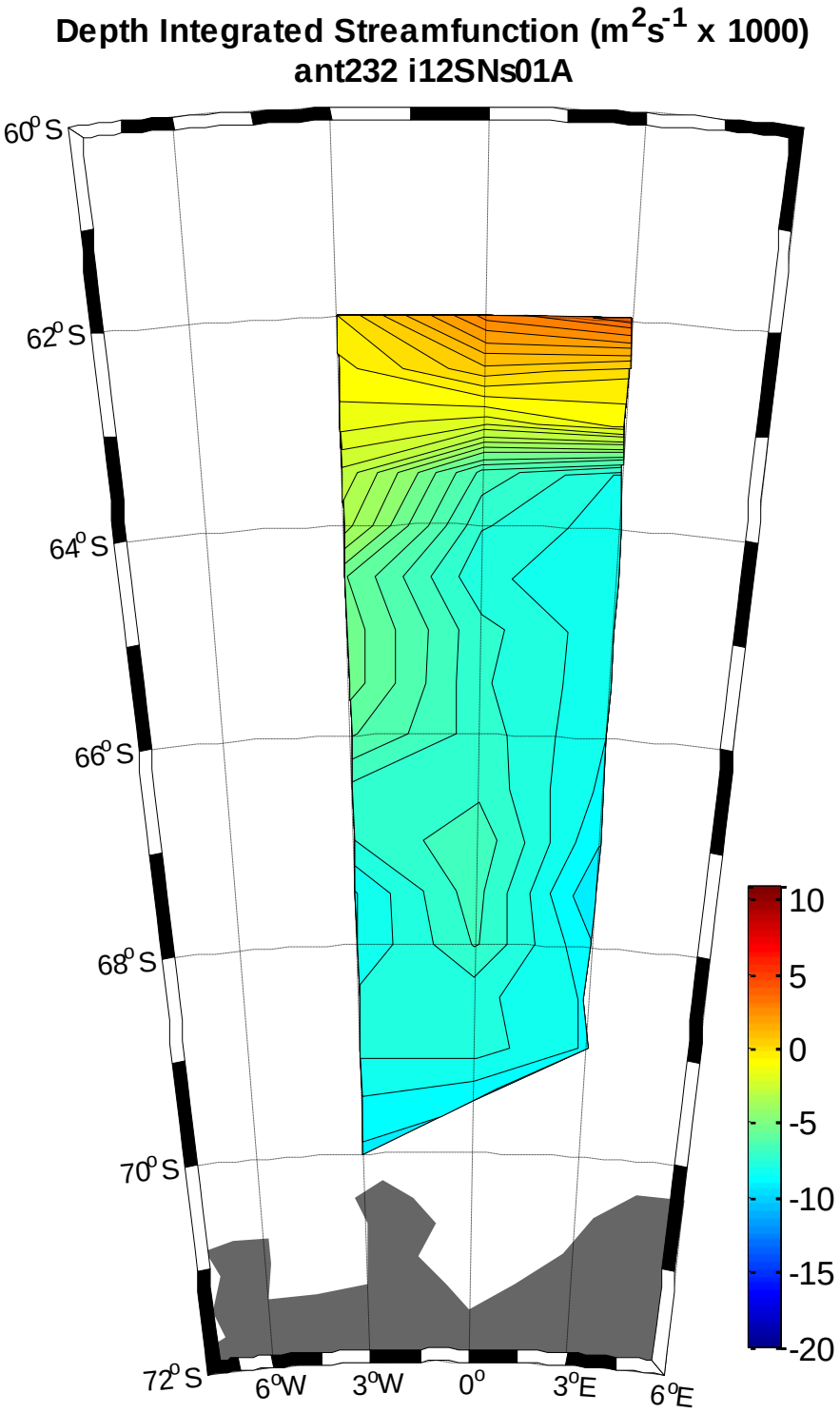

Figure 4.4.44 - Full-depth stream function of the subset-domain IMBAM solution for the *ANT-XXIII/2* cruise, as in Figure 4.4.27f.

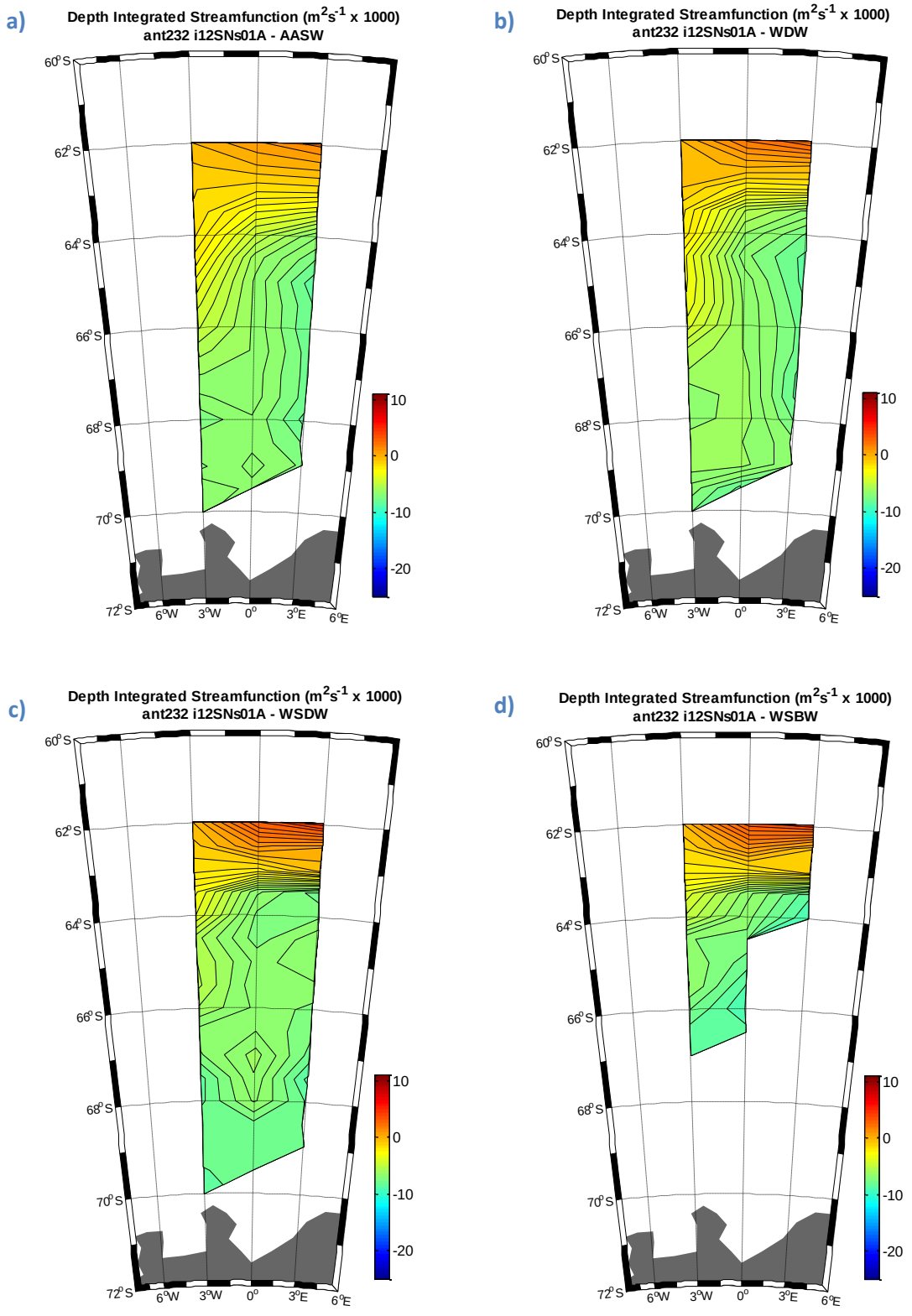

Figure 4.4.45 – Water mass specific stream functions of subset-domain IMBAM solution for the *ANT-XXIII/2* cruise, as in Figure 4.4.33

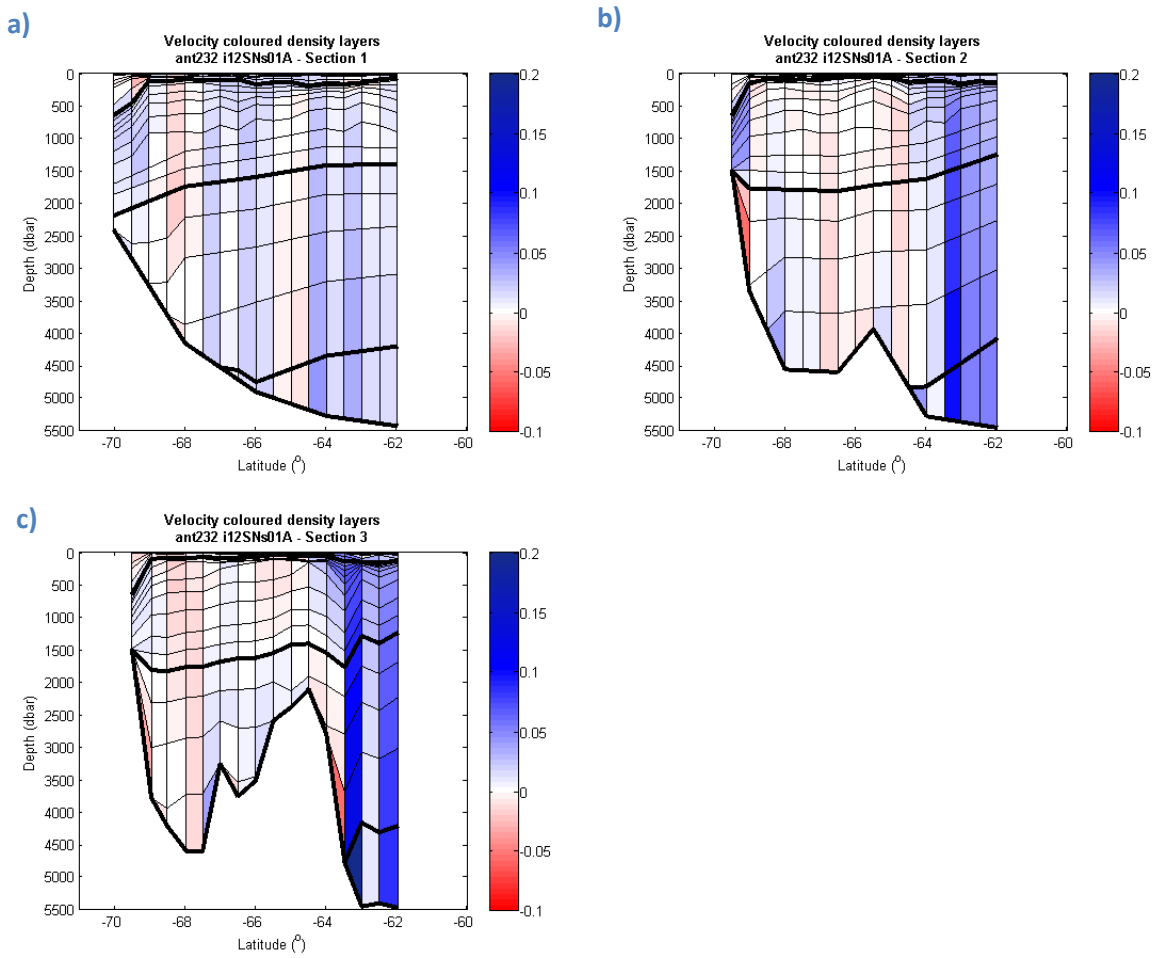

Figure 4.4.46 – Sections of velocity for IMBAM solution for the ANT-XXIII/2 cruise, as in Figure 4.4.44, along a) 3°W, b) the Greenwich Meridian and c) 3°E. Westward transport is positive (blue) and eastward transport is negative (red).

Table 4.4.10 – Westward volume transport contributions from the different water masses across each north-south section for ANT-XXIII/2 subset domain as in Figure 4.4.44

Transport (Sv)	***Section 1: 3°W***	***Section 2: 0°***	***Section 3: 3°E***
Full Depth	41.7	59.0	64.6
AASW	0.9	1.2	1.3
WDW	10.8	12.9	13.9
WSDW	23.1	33.1	36.9
WSBW	6.9	11.9	12.6

the northern slope of Maud Rise (see Figure 4.4.46c at ~2000m in particular). This is despite the overall pattern of flow being maintained.

The consequence for transport contributions is that the WSDW dominates with a higher 55-57% of the transport, WDW with a lower 21-26% of the transport, WSBW at a largely unchanged 17-

20% of the transport and AASW with just 2% of the transport, compared to up to 8% in the *ANT-XXIII/2* full domain solution.

4.4.8 Comparison & Summary

The sections of westward transport for each cruise show a broadly columnar flow field (Figure 4.4.34, Figure 4.4.37, Figure 4.4.40, Figure 4.4.43, and Figure 4.4.46), with station pairs frequently exhibiting no level of no-motion. However, there are also numerous reversals in the direction of flow across the whole of the depth range, showing that despite the interlinking of multi-box set-up there is a significant dependence on the local hydrographic conditions.

The tables of total transport and water mass transport, whilst useful for examining the cruises individually, do not provide spatially equivalent values yet a direct comparison of cruise transports is essential for assessing the variability of the transport across the Lazarev Sea. To this end the cumulative westward transport for each cruise along all the coincident meridional sections are shown in Figure 4.4.47 (omitting the 2°W and 4°W *ANT-XXI/4* sections). These transports are normalised to zero at 68°S as at this latitude there are regions of relatively slack flow covered by all the cruises.

Starting in the east of the domain along 3°E, it is clear that *ANT-XXII/6* and *ANT-XXIV/2* have similar transports from 68°S up to the latitude of Maud Rise at 63°S, although further north total transport diverges significantly by as much as 22 Sv. Whilst *ANT-XXIII/2* reaches a similar total transport to *ANT-XXIII/6* by 60°S, the transport to the south of Maud Rise is radically different owing to the earlier described dominance of southward flow. South of 68°S the westward trend is common between the two cruises, although with a difference of 13 Sv.

The same pattern is replicated along the Greenwich Meridian, with the addition of an intermediate profile from *ANT-XXI/4* where, moving north from 68°S, eastward transport first dominates followed by a continuous westward transport across the area south of Maud Rise. A much lower transport of 40 Sv is evident by 62°S compared to the higher transport of 59 Sv and 70 Sv for *ANT-XXIII/2* and *ANT-XXIII/6* respectively. This difference may well arise from the absence of

ADCP reference data for the extreme north of the domain and so may not be representative of the transport at this latitude.

The comparisons of the latter three cruises across 3°W show a broadly similar pattern north of 68°S, and again the transport estimates merge to the north of the latitude of Maud Rise. In between there is a range of as much as 10 Sv at ~65°S. At the northern boundary of the domains of *ANT-XXIII/2* and *ANT-XXIII/6* the total transport are 84 Sv and 89 Sv respectively. South of 68°S the transport estimates are much broader with a minimum of 3 Sv and a maximum of 29 Sv.

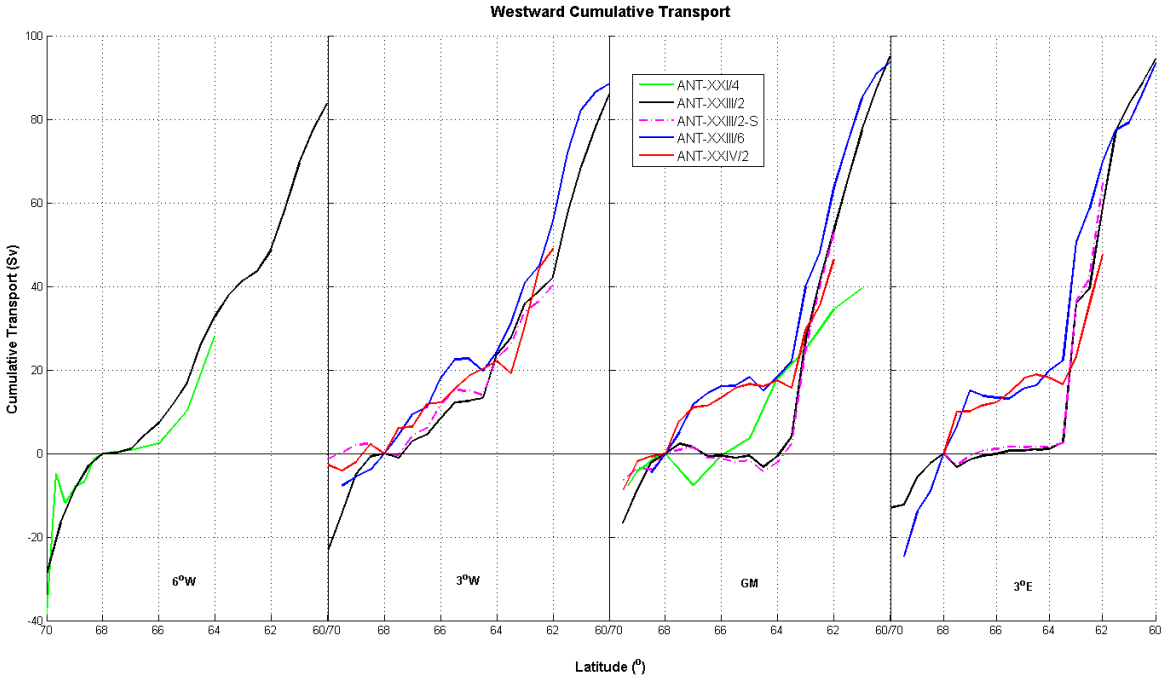

Figure 4.4.47 – Westward cumulative volume transport normalised to 68°S for all full domain LaKriS cruises, plus the ANT-XXIII/2 subset domain solution as highlighted in the key. Westward (eastward) transport is denoted by positive (negative) slope.

Along 6°W there is a similar positive trend in the transport to the north of 68°S, with the northern-most comparable transport for *ANT-XXI/4* and *ANT-XXII/2* being 28 Sv and 33 Sv respectively. To the south the trend is in lesser agreement, with a reversal in flow for *ANT-XXI/4*, although still a higher transport of 38 Sv versus a lower transport of 29 Sv for *ANT-XXII/2*.

Supporting the validity of the solutions for the smaller domain cruises, the grey-dashed line representing the subset domain covering *ANT-XXIII/2* for 3°W, the Greenwich Meridian and 3°E is reassuringly similar to the full domain solution. The exception to this similarity is the transport along 3°W south of 68°S which, as earlier described, is accounted for by the absence of the ADCP reference data.

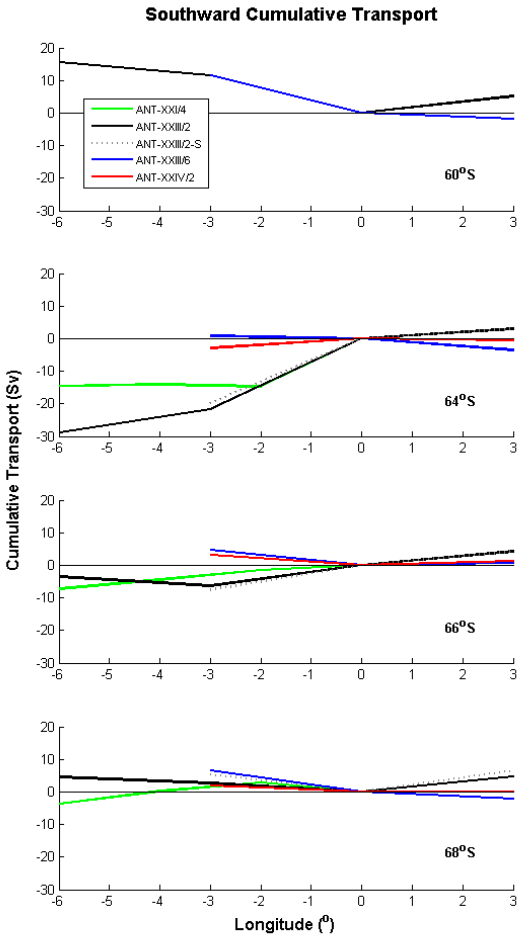

Figure 4.4.48 – Southward cumulative transport normalised to the Greenwich Meridian for all full domain LaKriS cruises, plus the ANT-XXIII/2 subset domain solution as highlighted in the key. Southward (northward) transport is denoted by positive (negative) slope.

Southward transport across four selected latitudes across the model domains are shown in Figure 4.4.48. Across 60°S the two cruises have a similar transport between the Greenwich Meridian and 3°W, although opposing transports to the east. There is a more pronounced contrast across 64°S with a notable difference between the larger southward transport of *ANT-XXI/4 & ANT-XXIII/2*

compared with the much smaller transports of *ANT-XXII/6 & ANT-XXIV/2*. Across 66°S and 68°S, there is a range of transport patterns reflecting the different orientation of the variably meandering flows in the south of the cruise domains.

The broad patterns of flow indicate that two conditions seem to prevail. Firstly, the zonal transport across the 3°E and the Greenwich Meridian in the Lazarev Sea can be confined largely to the northern flank of Maud Rise and along the continental slope as seen in *ANT-XXIII/2*, whilst the flow diverts southward linking the northern and southern latitudes of strong zonal transport. The alternative situation is that the transport is less constricted and flow between Maud Rise and the continental slope can be more prominent, as for *ANT-XXIII/6* and *ANT-XXIV/2*. The remaining cruise, *ANT-XXI/4*, shows a notable south-westward flow between 66°S and 68°S which seem transitional between the other two states. However, the water mass stream functions have shown that the patterns of transport vary with both depth and position. Comparison of these results with other estimates, and the mechanism leading to these differences are now discussed.

4.5 Discussion

4.5.1 Validity of the IMBAM solutions

A clear feature of the model solutions is that the total transports mask the detail of the different water mass transports. This provides reassurance that the relationship between mass conservation, Margules equations and velocity references allows for local variability between individual station pairs within the overall solution. It is further reflected in the detailed variability shown in the velocity section plots which includes both broad flows and single density face deviations from the surrounding field based on specific local values.

However, despite the internal consistency of the results, there are some aspects of the solutions that cause concern regarding the representativeness of the results for the actual Lazarev Sea transport. Firstly, there are areas of unexpectedly low transport in unexpected directions in the north-east of the *ANT-XXI/4* domain, and the south of the *ANT-XXIV/2* and *ANT-XXIII/2* subset domains. These areas correspond to missing ADCP stream function coverage, which appears to have a detrimental effect on the robustness of some solutions due to the reliance on mass conservation and Margules equations alone.

The presence of small-scale features within the ADCP stream function can also produce results which are otherwise inconsistent with the known general circulation. A notable instance of this is the south-west corner of the *ANT-XXI/4* domain whereby the stream function (see Figure 4.4.33 for layer 4) includes a recirculation near the shelf break and accounts for the strong eastwards transport near 70^{o}S.

A final concern with using the ADCP stream function approach is that the process of obtaining a reference velocity involves imposing a non-divergent flow on a depth layer. However the presumption in the inverse model is that the transport is along isopycnals which are known to slope, vary in depth and outcrop across the domain. Therefore there is a mismatch in the approach. This is partially overcome by using all the velocity reference levels, and therefore any density layer falling

within an ADCP reference depth range makes use of the value. This does not however address the initial imposed depth-dependent non-divergent flow, which is a limitation of the solutions.

The VM-ADCP data only covers less than 10% of the total water column, and thus whilst it offers the best available reference level for the LaKriS cruises, could be improved upon. Other studies (e.g. McDonagh et al. 2008) have included the use of lowered-ADCP data as a further source of velocity reference. Future applications of IMBAM could include such data.

A further limitation arises from the variably large number of 1000m depth CTD stations. The velocity sections show how the station-to-station variability in Neutral Density surfaces is evident within the upper 1000m and over the whole depth of bottom reaching stations. However, by definition the deep profiles of Neutral Density surfaces for shallow stations result in smooth profiles. The result is the loss of any interplay between surfaces which, if observed, might vary in gradient and/or oppose in sign. In terms of net transport this may have a minimal impact at mid-depths, as it is congruous with calculating the geostrophic transport between two distantly spaced stations, as opposed to a series a calculations at each intermediate station between them. However, the limitation of the CTD data is clearly evident due to the absence of WSBW in the west of the *ANT-XXI/4* domain. In the absence of a more comprehensive dataset, the solutions are as valid as the method allows.

The surface circulation varies between the cruises, with the broad flow pattern being in alignment with the deep circulation for *ANT-XXI/4, ANT-XXIII/2* and, to a lesser degree, *ANT-XXIV/2*. *ANT-XXIII/6* was the only cruise undertaken during the Austral winter and shows a surface circulation which is markedly different to the deep circulation. This may be the result of the deeper mixed layer dominating the AASW circulation, with a lower contribution by the underlying stratified water column which dominates in the summer and autumn. That the surface circulation is different in the winter – corresponding to a very different velocity reference response as detailed for Figure 4.4.39 – than in the summer helps to explain why other cruises have a more gradual transition between ADCP reference levels. In summer months, more of the upper water column is influenced by the sloping of isopycnals and less so by surface forcing on the mixed layer.

There is a consistently high contribution of transport from the WSDW, with percentage contributions ranging from 45-62% of the total transport across a north-south section, equating to actual transports of between 20.5 Sv and 60.5 Sv, albeit over different latitudinal ranges. There are also surprisingly large WSBW transport estimates, as high as 20.9 Sv, with both the WSBW and the WSDW showing instances of bottom intensified flow.

The final general observation is that the barotropic component of transport dominates the baroclinic component. This is demonstrated by the presence of westward (eastward) flow where the slope of the neutral surfaces would result in an eastward (westward) flow if baroclinic transport were to dominate. This can be observed particularly well along the northern and southern flanks of Maud Rise, where the strong circulations are often counter to the isopycnal slope. This is not to say that the slope of the isopycnals does not act to enhance or reduce that transport – indeed the baroclinic component leads to reversals of flow at various latitudes across the whole depth range – but that the barotropic component which is included by the velocity referencing has a first order effect leading to often columnar flow.

4.5.2 Comparison with the other estimates of the circulation in the Lazarev Sea

There is clear variability in the distribution of the volume transport amongst the LaKriS cruises, as evidenced by Figure 4.4.48. Whilst the details of transport have already been described, what is less clear due to the variable domain size is the total volume transport of the southern limb of the Weddell Gyre. The two most extensive domains, *ANT-XXIII/2* and *ANT-XXIII/6* have solutions with total transports of 107.3 Sv and 118.0 Sv respectively across the full depth sections at 3°E. The best comparison for these results is Cisewski et al. (2011) which presents a total transport of 23.9 ± 19.9 Sv for *ANT-XXIII/2* and 93.6 ± 20.1 Sv for *ANT-XXIII/6*. The latter is a good match for the IMBAM solution, being well within the range of their error. The former is dramatically smaller than the IMBAM solution. This is problematic as both estimates use the same CTD data and the same original ADCP data. The discrepancy seems to primarily result from the use of a raw ADCP format in Cisewski et al. (2011) whereas the final IMBAM solutions utilise ADCP velocities derived from a stream function. As can be seen in Figure 4.4.30c the solutions using the raw ADCP data for *ANT-*

XXIII/6 are similar to the solutions using the stream function ADCP data. The raw ADCP solution, at 99.4 Sv, is an even closer match to the Cisewski et al. (2011) estimate. The raw ADCP referenced IMBAM solution for *ANT-XXIII/2* is 66.8 Sv westward across 3^{o}W, which is closer to the Cisewski estimate, although still beyond their upper error.

The stream function ADCP was favoured in this study for a number of reasons. Firstly, the technique provides a set of velocity references for the entire domain, regardless of whether or not the ship's track covered a particular station pair. Secondly, despite concerns over imposing divergence free flow over a depth range rather than an isopycnal range, the stream function provides an internally consistent flow field which smoothes out inconsistencies arising from ADCP measurements being close in space but far apart in time. This is particularly pronounced during *ANT-XXIV/2* where the central Greenwich Meridian section was undertaken last. Finally, the stream function ADCP referenced solutions retain small-scale circulation features, which are particularly pronounced in individual water mass circulations. Thus the imposition of smoothed divergence free flow does not have an overriding effect on local hydrographic conditions.

In addition, the Cisewski et al. (2011) transport estimates are based on the deepest common level between station pairs, whereas the solutions presented in this study are inclusive of the topographic effects upon mass conservation and outcropping isopycnal surfaces. Therefore higher transports are to be expected from estimates which are inclusive of the entire water column and which are inclusive of bottom geometry, although this factor is unlikely to be sufficient to account for the noted discrepancy.

The central axis of the Weddell Gyre cannot be definitively identified from the LaKriS data as the grid does not extend sufficiently far north. However the axis is known to be present near 60^{o}S, and this is well demonstrated by the repeat observations of the geopotential anomaly along the Greenwich Meridian detailed by Fahrbach et al. (2011). Thus the dominance of westward transport in the IMBAM solutions is consistent with the northward extent of the southern limb of the Weddell Gyre, however the strength of the westward flows in the northern part of the domain solutions appear excessively large if the central axis lies near 60^{o}S. This may potentially arise from ADCP reference

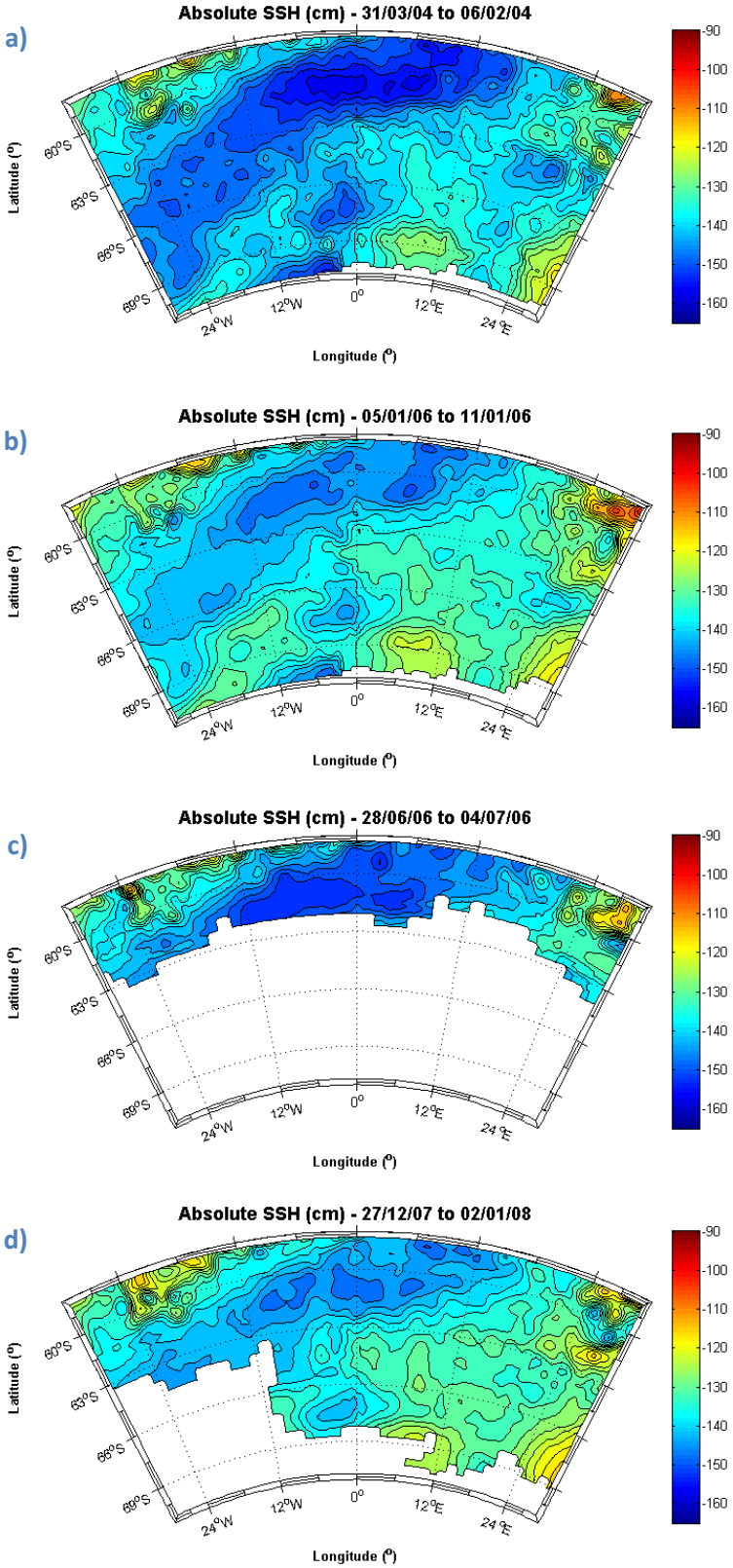

Figure 4.4.49 – Merged absolute dynamic topography in centimetres from AVISO altimetry uniform product using TOPEX of Jason, and ERS or Envisat data. Product is inverse-barometer corrected sea level and detided. Each plot presents a single-week snapshot during each of the four LaKriS cruises: a) for the early part of ANT-XXI/4, b) for late part of ANT-XXIII/2, c) for the early part of ANT-XXIII/6 and d) for the late part of ANT-XXIV/2 to make best use of data at minimum sea ice extent.

stream functions where the ADCP data may be sufficiently non-synoptic to result in large northward transports out of the northern domain boundary.

For comparison with the ADCP reference stream functions, the absolute sea surface height (SSH) displayed in Figure 4.4.49 for each of the 4 LaKriS cruises show the surface expression of the Weddell Gyre circulation. Notably the SSH contours include the broad pattern of meandering features co-located with the major bathymetric features of the region and are observed to persist throughout each of the cruises – where observable due to sea-ice cover – with varying intensities and differences in the detail due to mesoscale features. Additionally, the SSH suggests a central axis of the Weddell Gyre at ~61^{o}S on the Greenwich Meridian, however, as already noted the SSH is the surface expression of the circulation and may not reflect the deeper circulation. Weaker westward flow is consistently observed in the IMBAM solutions for the AASW and stronger flow below, suggesting a non-uniform location of the central axis with depth.

Earlier attempts to quantify the transport of the gyre provide reassurance regarding the magnitude of our results. Carmack and Foster (1975) use geostrophy and current measurements across a cruise line extending from the Scotia Ridge to Cape Norvegia to estimate the eastward transport of the Weddell Gyre, arriving at a total transport of 96.9 Sv, with ~70% of this transport accounted for by the combined WSDW (53.1 Sv) and WSBW (15.6Sv). Furthermore they estimate a 23.8 Sv transport of the WDW and 4.4 Sv in the AASW classes. These values are in good agreement with our own estimates of the relative contributions of the different water masses, albeit for the northern limb rather than the southern. They note that there must be an assumption that short-term current measurements represent the long-term conditions. As our results show, however, it is rather that they need to be representative of the cruise duration as the total transport and transport distribution of the Weddell Gyre does not appear to be constant.

Across the Greenwich Meridian, Whitworth and Nowlin (1987) calculate a westward baroclinic transport of 17 Sv, although they recognise a significant barotropic transport is likely to exist. Based on wind-driven Sverdrup transport, Gordon et al. (1981) estimate a total Weddell Gyre

transport of 76 Sv, equating to ~65 Sv across the Greenwich Meridian. Like this study, they observe the need to have representative current measurements to produce robust estimates of transport and note the absence of a level of no motion in the Weddell Sea. Importantly they describe how the transport of WDW near the continental shelf will contribute to a greater degree to the water mass characteristics in the southwest embayment of the Weddell Sea more so than flow north of Maud Rise. This northern jet would have a greater impact on the central waters of the Weddell Gyre. However, whilst there is no doubt general merit in this observation, the occurrence of large southward transports would allow thermohaline signals north of Maud Rise to have a greater effect in the southwest Weddell Sea, and thus impact on sea-ice and water mass modification processes.

Schröder and Fahrbach (1999) make use of CTD and ADCP data in a conceptually similar manner to Cisewski et al. (2011) to calculate transport between the Scotia Ridge and Cape Norvegia, estimating a 33 Sv westward without referencing to ADCP data for cruises undertaken between 1989 and 1994, and 66 Sv westward across the Greenwich Meridian using ADCP referenced transport for a cruise in 1996. In the former example, they diagnose flow over the northern and southern flanks of Maud Rise, and in the latter example only flow along the northern flank of Maud Rise. They suggest the presence of a two-cell structure in the deep ocean, however we observe no evidence of this and propose this may relate to the quasi-stationary warm water pools formed to the southwest of the rise first noted by Muench et al. (2001) and clearly indicated by the solution for *ANT-XXIII/2*.

Klatt et al. (2005) assess the transport of the Weddell Gyre and diagnose a 56 Sv westward transport using 5 repeat CTD sections along the Greenwich Meridian in combination with time series data from 5 unevenly spaced moorings along the Greenwich Meridian south of 60^{o}S. However, whilst their transport estimates and zonal velocity section are in broad agreement with the IMBAM solutions, their approach is to use the repeat sections to construct a mean state upon which to calculate transport. Whilst described as necessary given the nature of the data, the approach obscures the inherent temporal variability of the distribution of the Weddell Gyre transport diagnosed using IMBAM.

The solutions presented in this study are not inconsistent with the broad range of previous transport estimates for the southern limb of the Weddell Gyre, although the two cruises which span the entire southern limb are in the higher range. However, with respect to Cisewski et al. (2011) the question as to which method is most representative is an open one with no obvious and practical course for resolution.

4.5.3 Implications of the IMBAM solutions

The warm water halo around Maud Rise described by de Steur et al. (2007) is related to the jet on the northern and western flank of Maud Rise which propagates the Warm Deep Water westward across the Lazarev Sea. This is observed by other authors and is produced by some IMBAM solutions. The solutions for *ANT-XXIII/6* and *ANT-XXIV/2* show a broader less bathymetrically constrained flow across the Lazarev Sea which would act to advect heat anomalies westward rather than deflecting the anomalies southward, therefore whilst the warm water halo is apparently a recurrent feature, it is unlikely to be permanent.

The discussions regarding the changes to observed Weddell Sea heat content variability, detailed well by exchanges of view in Smedsrud (2005), Fahrbach et al. (2006), Smedsrud (2006) highlight the uncertainty regarding internal forcing and external forcing to the Weddell Gyre. Our results suggest that internal variability of transport across the Lazarev Sea must influence the propagation of water mass characteristics. However there is a causal dilemma with the interpretation of these results. The transport and patterns of flow which act to propagate thermohaline signals in the ocean are significantly affected by the slope of neutral surfaces. However, as the density structure of the water column is determined by the distribution of temperature and salinity variations, there remains a question as to whether upstream variations of the inflowing LCDW/WDW may lead to the very changes in flow that lead to the variable density structure observed across the Lazarev Sea. Conceptually this ocean weather may be akin to the manner in which high-pressure systems in the atmosphere can be held over the topography of the land before being moved off with teleconnected

changes in the atmosphere. If this is the case over and around Maud Rise, then interpreting variability is even more challenging than currently understood.

The Weddell Gyre is proposed to act as a heat buffer by Fahrbach et al. (2011), with pronounced variability of properties of all water masses on multi-annual timescales resulting from the mismatch between the northern and southern limbs of the Weddell Gyre. The difference between the northern eastward flow and the southern westward flow is proposed to arise from variable forcing by the atmospheric wind fields, having the result of increasing (decreasing) the export of WSDW and decreasing (increasing) the import of CDW. Whilst the multi-annual observations of the Greenwich Meridian variability are compelling, the variability of the 3-dimensional transport fields presented in this study bring into question the degree to which the Greenwich Meridian provides a representative example of the Weddell Gyre transport due to the bathymetric control exerted over the flow by Maud Rise. Whilst the 8 repeat sections over 24 years they analyse represent a notably good temporal coverage for the sparsely sampled Southern Ocean, it is clear that significant variability can occur over much shorter time periods presenting an issue of potential aliasing of oceanic variability.

The dominance of horizontal mixing as a modifier of the Warm Deep Water characteristics is noted by Leach et al. (2011) whilst examining the downstream modification of potential temperature. There is a presumption of westward transport inherent in their technique which does not take account of the large southward transport and variable velocities observed in the IMBAM solution for *ANT-XXIII/2*. Whilst horizontal mixing undoubtedly does play a dominant role over vertical mixing in the southern limb of the Weddell Gyre, an element of the change in properties is likely to be due to lateral redistribution of hydrographic properties owing to the meandering flow field, which is included as 'eddy diffusivity' in their solution.

Our results address how variable observations by numerous authors over a range of longitudes in this region of the Weddell Gyre may have no real bearing on the observed variability of heat and salinity, and may in fact reflect lateral redistribution by variable flow fields. Given the clear impact of bathymetry on the flow through the western Lazarev Sea associated with Maud Rise and the

continental slope, it is logical to conclude that the transport across the region would also be affected by the interaction of the flow with the submarine peninsula of Astrid Ridge which has a central axis around 12^{o}E. It poses a significant bathymetric obstacle as far north as 65^{o}S (Leinweber and Jokat 2012), however, to date the only study to include Astrid Ridge by Schröder and Fahrbach (1999) includes only very sparse stations over the extreme western flank of the ridge. Despite it being of great potential importance to the flow of the southern limb of the Weddell Gyre, no other studies appear to have been published. Whilst hypothetical, variable interaction with Astrid Ridge up stream of Maud Rise may contribute to the variability of flow across and south of the rise.

4.6 Conclusion

This study attempts to fully utilise the hydrographic data from the Lazarev Sea Krill Study (LaKriS) to infer the total volume transport across the gateway to the Weddell Sea. The quasi-synoptic datasets are analysed using the Inverse Multi-Box Adaptable Model (IMBAM) producing internally consistent results within the broad range of other Weddell Gyre transport estimates, with a maximum westward total transport of 118 Sv occurring across 3^{o}E during the Austral winter of 2006. During Austral summer 2005/06 a similar but lower total transport of 107.3 Sv was observed across the same longitude, however there was a large southward transport across 9^{o} of longitude at 64^{o}S of nearly 30 Sv during this cruise representing a significant southward deflection of the flow around the western flank of Maud Rise.

What is clear from the solutions for the four cruises is that the Lazarev Sea – influenced by the presence of Maud Rise – plays a key role in the variability of transport through the southern limb of the Weddell Gyre. There are highly likely large scale deviations in the flow which will affect the propagation of thermohaline signals in the Weddell Gyre. This includes both variability in the pathway and volume of LCDW entrainment upstream of Maud Rise in the eastern gyre, and the distribution of the WDW downstream of the Lazarev Sea. Specifically, the southward meandering observed in some solutions would advect less dilute LCDW/WDW closer to the continental shelf whereas stronger westward flow would direct the less dilute LCDW/WDW into the centre of the gyre. Such downstream variability in WDW characteristics has been observed by Graham et al. (2013) and is attributed primarily to variations in surface wind stress.

Such variations in distribution would impact the cryosphere though affecting the rates of water mass modification processes associated with sea-ice formation and melt occurring over the continental shelf, and also impact the rate of basal melting of ice shelves due to varying supply of warm saline water onto the continental shelf. Additionally, the redistribution of mass in the Weddell Gyre would also affect the density distribution and thus the thermal wind component of mass

transport. As earlier noted, this variability is observable in SSH determined from satellite altimetry – even if this surface signature it is not always consistent with the IMBAM solutions.

The variability of water mass characteristics observed during repeat occupations of the A12 cruise section, as detailed by Fahrbach et al. (2011) and others, may be unrepresentative of any long-term trend, and also may not even be representative of inter-annual variability. This study has demonstrated the potential for significant aliasing due to non-consistent seasonal variation, and the potential for transient short-term variability arising from baroclinic instability related to the shedding of eddies as observed by de Steur et al. (2007). Furthermore, the deployment of moorings has not been sufficient to resolve spatial variability despite adding to knowledge of temporal variability at individual points in the Lazarev Sea. How this observational challenge can be overcome with sufficient resolution remains, as ever, problematic.

Issues of sufficiently high resolution sampling extend to the observation of the deep ocean as the scarcity of data decreases the reliability of the IMBAM solutions with respect to the deep circulation. This is particularly problematic for the solutions provided for *ANT-XXI/4* and *ANT-XXIV/2* as they do not include the deep variability in neutral surfaces across several degrees of latitude.

Whilst the formulation of IMBAM can be considered computationally robust, and the solutions it generates are internally consistent, concern remains over the validity of the stream function ADCP reference velocities which lead to such different results to Cisewski et al. (2011). Either the divergence-free stream function ADCP reference velocities impose unrealistic constraints on the density structure leading to erroneously large volume transports, or the stream function ADCP approach provides an appropriate contribution to the technique used in IMBAM which accounts for the 3-dimensional structure of the ocean. The uncertainty arising from different results produced by different studies is itself of interest as it reflects the challenges inherent in quantifying the complex and under-sampled Southern Ocean system.

If the results presented in this study do reflect the actual range of variability in volume transport, then this has significant implications for the short-term variability of the transport of thermohaline signals, particularly from the inflowing Warm Deep Water. Further study of the Lazarev Sea is merited, particularly further east where the submarine peninsula of Astrid Ridge presents an additional bathymetric obstacle to the southern limb of the Weddell Gyre.

In summary, this study suggests that the southern limb of the Weddell Gyre may experience higher transports than other recent studies have suggested, whilst simultaneously undergoing significant meandering variations in the pathways of the deep water flow. This has implications for the rate of upstream entrainment of LCDW into the eastern Weddell Gyre, and consequences for the distribution of WDW downstream into the south western Weddell Gyre where a significant proportion of climatically important ice-sea interactions take place.

4.7 Special Acknowledgements

Our thanks go to the scientists and crews of the *RV Polarstern* during *ANT-XXI/4*, *ANT-XXIII/2*, *ANT-XXIII/6* and *ANT-XXIV/2* whose data we have used, and to the Alfred Wegener Institute for hosting the publicly available data on the *Pangaea* database.

Additional thanks go to Clare Bellingham of the National Oceanography Centre, Liverpool, for providing ready access to AVISO sea surface height data.

Chapter 5

Summary

5.1 General conclusions

It is important to consider the Southern Ocean system simultaneously within the context of the Global Overturning Circulation and within the framework of the dynamics of the ACC in order to understand the processes governing circumpolar variability of water mass characteristics and transport. The overall result of isopycnal uplift and outcrop, water mass modification through interaction with the cryosphere, and the subsequent subduction of new water masses, is the formation of the bottom and intermediate limbs of the global ocean circulation. This process is mediated by the eastward transport of the ACC associated with strong meridional fronts and enabled by northward surface Ekman transport balanced by the sub-surface southward eddy transport.

The character of the Southern Ocean is by no means universal. There are clear regional variations in the definition of ocean fronts and the character of the water column. The frontal limits of the ACC are dynamic, locally variable and can be described using a variety of parameters (Sokolov and Rintoul 2002), whilst also simultaneously controlled by the large scale overturning circulation. It is therefore important to recognise that the Southern Ocean contains a continuum of different local regimes through which the large-scale circulation acts.

As a simple example such local conditions can clearly be observed in the vertical distribution of salinity maximum of the LCDW, which changes in depth over a 1000 m range as it moves from basin to basin (Figure 3.12b). Most notably is the progression from the southeast Indian sector through to the southwest Pacific sector, where the depth increases by 500 m as a result of changes to the overlying and underlying water masses, and topographic effect of passing over the Southeast Indian Ridge.

There is a clear circumpolar decrease in the deep salinity maximum (Figure 3.12a) starting from the NADW source ($S_P > 34.76$), advecting around Antarctica ($34.76 > S_P > 34.71$) and into the southern limb of the Weddell Gyre ($S_P < 34.71$). A short increase occurs in the northern Weddell Gyre through interaction with the ACC to the north. However the number of repeat occupations of sections in the dataset across the Southern Ocean is insufficient to identify an obvious temporal trend in salinity over the course of observations (Figure 3.13).

Low-rates of cross-frontal mixing are identified from bulk entrainment estimates (Table 3.2), with the dominant entrainment of NADW into the ACC occurring in the western Atlantic sector, as opposed to further east. The dominant entrainment of LCDW into the Weddell Gyre occurs in the eastern Weddell Gyre, and not along the northern boundary of the gyre where the fronts are stronger. It is worth noting that the whole of the WDW is not of direct CDW origin and is comprised of a progressive mix with overlying and underlying water masses (Whitworth and Nowlin 1987) which are ultimately derived from the WDW itself.

An estimate of mixing coefficients in the LCDW/WDW is consistent with other SO estimates. A vertical mixing coefficient of $\kappa_V = (2.86 \pm 1.91) \times 10^{-4}$ and an isopycnal mixing coefficient of $\kappa_I = (8.97 \pm 2.13) \times 10^{2}$ are calculated for the eastern Indian and Pacific sectors of the Antarctic Circumpolar Current. A $\kappa_V = (2.39 \pm 0.73) \times 10^{-5}$ an order of magnitude smaller and a $\kappa_I = (2.47 \pm 0.27) \times 10^{2}$ three times smaller are calculated for the southern and eastern Weddell Gyre. This reflects higher mixing rates above the rough bathymetry over which the ACC flows than through the abyssal plain dominated Weddell Gyre.

The results of the Inverse Multi-Box Adaptable Model suggest that the flow through the Lazarev Sea is variable in total transport (Figure 4.4.47) with an observed solution maximum of 118 Sv of westward transport across 3^{o}E. The flow is observed to either be dominated almost entirely by westward transport (e.g. Figure 4.4.38); or can incorporate large southward meanders (e.g. Figure 4.4.35); or can be in an intermediate state (Figure 4.4.32). Furthermore, due to the variable depth or absence of a level of no motion the different water masses can exhibit different flow fields. The

nature of the solutions significantly supports the concept of bathymetric control over the transport of the Lazarev Sea.

The Southern Ocean is a critical part of the global climate system, regulating the north-south exchange of heat through its meridional frontal barriers and moderating gyre circulations. This describes a system which acts to mitigate climate change by smoothing the propagation of themohaline signatures from the NADW, through the CDW into the gyres and coastal regions.

5.2 The LCDW link

The Circumpolar Deep Water is a critical link in the overturning circulation. It bridges the primordial North Atlantic Deep Water and the terminal Warm Deep Water via the dynamics of the Antarctic Circumpolar Current. The circumpolar trend in the deep salinity maximum demonstrates that this system acts to insulate the Weddell Gyre from short-term changes in the properties of the overturning circulation and debunks the classical perception of an overturning circulation dominated by its meridional component. There are two key conclusions resulting from this work:

1. The Antarctic Circumpolar Current acts as an oceanic blender of the Lower Circumpolar Deep Water, insulating the Weddell Gyre from short-term changes in the thermohaline properties of the North Atlantic Deep Water, whilst maintaining a circumpolar decrease in salinity along the ACC path;
2. The Lazarev Sea acts as a gateway region to the Weddell Sea proper whereby bathymetric influence results in variable flow fields, providing a significant contribution to the observed variability of transport and water mass characteristics.

In contrast to one another they show how the broad-scale circulation can mediate variability, whilst local conditions can significantly affect the observed state of the ocean.

5.3 The future – improving observations, enabling greater understanding

This thesis has analysed large oceanographic datasets of ship based observations to effectively demonstrate the variability and mixing of the Lower Circumpolar Deep Water, and the variability of the Lazarev Sea transport from inverse methods. However, this data – whilst particularly valuable in the sparsely sampled Southern Ocean – nevertheless represents a chronic under-sampling of an expansive and complex system. The practical and budgetary constraints of oceanographic and, particularly, Antarctic observational research is a serious challenge. From this it is clear that greater co-ordination of oceanographic survey programmes combined with more effective use of sea time to ensure the usefulness of datasets is of paramount importance particularly with respect to the deep ocean. A general view seems to be that the deep ocean is less variable and therefore has less observational value than the surface ocean. However, failing to observe the deep ocean provides an incomplete picture, and given the current hiatus in global warming which possibly arises from the export of ocean heat content to the deep ocean (e.g. Purkey and Johnson 2010, Kouketsu et al. 2011), it is more critical than ever to survey and understand the properties and circulation of the deepest waters of the global ocean. Projects such as the Synoptic Antarctic Shelf-Slope Interactions project (SASSI - see Heywood et al. 2012) and the progress in developing a multi-national Southern Ocean Observing System (SOOS - see Meredith et al. 2013) as a coherent endeavour are welcome progress, however making the data from such efforts readily available would seem to be an obvious and necessary direction to take.

Other techniques such as satellite observations, the ARGO float network, moorings and gliders provide other avenues for exploring the variability of the world's oceans; however the oceanographic community must be careful not to extrapolate interpretations beyond what the data can reasonably be expected to support. Aliasing of temporal variability by research vessel cruises is clearly a difficult logistical and budgetary problem which is unlikely to be overcome, but the temptation to fill in the gaps in understanding with point measurements only partially resolves the sampling issue. As an example, the use of mooring data by Fahrbach et al. (2011) has the potential to spatially aliase the transport and characteristics of the Greenwich Meridian, which when combined

with temporally aliased occupations of the A12 cruise track can lead to potentially misleading interpretations of the impacts of variability upon the circulation. On a more basic level there is a question as to whether the existing repeated hydrography along the Greenwich Meridian continues to be a worthwhile endeavour due to the limitations imposed by the bathymetrically controlled flow. At the very least there needs to be clear recognition of these limitations in order to help understand the variability of the Weddell Gyre transport and water mass properties.

Whilst these broad considerations of oceanographic sampling in general are important, there are vast regions of the Southern Ocean which simply have not been sampled in any detail, if at all. A prime example of this is Astrid Ridge along the eastern limit of the Lazarev Sea. It is a region of significant and complicated bathymetry which has the potential to play an important role in the variability of the transport in the southern limb of the Weddell Gyre. Yet to date virtually no oceanographic research has been undertaken to investigate this interesting stretch of polar ocean. A concerted effort to close such gaps in knowledge would be welcome.

This is the classical challenge of oceanography: bridging the gap between the Eulerian and Lagrangian within the constraints of limited resources. Perhaps it is a gap which can only ever be narrowed but never closed, however the important thing is to recognise the limitations of what is available and then make best use of it.

References

Arhan, M., Heywood, K. J. and King, B. A. (1999) 'The deep waters from the Southern Ocean at the entry to the Argentine Basin', *Deep Sea Research Part II: Topical Studies in Oceanography*, 46(1–2), 475-499.

Bathmann, U. (2008) *The expedition ANTARKTIS-XXIII/6 of the research vessel "Polarstern" in 2006*, 580, Bremerhaven: Alfred Wegener Institute for Polar and Marine Research.

Bathmann, U. (2010) *The expedition of the research vessel "Polarstern" to the Antarctic in 2007/2008 (ANT-XXIV/2)*, 604, Bremerhaven: Alfred Wegener Institute for Polar and Marine Research.

Beckmann, A., Hellmer, H. H. and Timmermann, R. (1999) 'A numerical model of the Weddell Sea: Large-scale circulation and water mass distribution', *Journal of Geophysical Research: Oceans*, 104(C10), 23375-23391.

Bersch, M., Becker, G. A., Frey, H. and Koltermann, K. P. (1992) 'Topographic effects of the Maud Rise on the stratification and circulation of the Weddell Gyre', *Deep Sea Research Part A. Oceanographic Research Papers*, 39(2), 303-331.

Bindoff, N. L., Rosenberg, M. A. and Warner, M. J. (2000) 'On the circulation and water masses over the Antarctic continental slope and rise between 80 and 150°E', *Deep Sea Research Part II: Topical Studies in Oceanography*, 47(12-13), 2299-2326.

Brandt, A., Bathmann, U., Brix, S., Cisewski, B., Flores, H., Göcke, C., Janussen, D., Krägefsky, S., Kruse, S., Leach, H., Linse, K., Pakhomov, E., Peeken, I., Riehl, T., Sauter, E., Sachs, O., Schüller, M., Schrödl, M., Schwabe, E., Strass, V., van Franeker, J. A. and Wilmsen, E. (2011) 'Maud Rise – a snapshot through the water column', *Deep Sea Research Part II: Topical Studies in Oceanography*, 58(19–20), 1962-1982.

Bryden, H. L. and Pillsbury, R. D. (1977) 'Variability of Deep Flow in the Drake Passage from Year-Long Current Measurements', *Journal of Physical Oceanography*, 7(6), 803-810.

Callahan, J. E. (1972) 'The structure and circulation of deep water in the Antarctic', *Deep Sea Research and Oceanographic Abstracts*, 19(8), 563-575.

Carmack, E. C. and Foster, T. D. (1975) 'On the flow of water out of the Weddell Sea', *Deep Sea Research and Oceanographic Abstracts*, 22(11), 711-724.

Casal, T. G. D., Beal, L. M., Lumpkin, R. and Johns, W. E. (2009) 'Structure and downstream evolution of the Agulhas Current system during a quasi-synoptic survey in February-March 2003', *Journal of Geophysical Research-Oceans*, 114, 16.

Cisewski, B., Strass, V. H. and Leach, H. (2011) 'Circulation and transport of water masses in the Lazarev Sea, Antarctica, during summer and winter 2006', *Deep Sea Research Part I: Oceanographic Research Papers*, 58(2), 186-199.

Cisewski, B., Strass, V. H., Losch, M. and Prandke, H. (2008) 'Mixed layer analysis of a mesoscale eddy in the Antarctic Polar Front Zone', *Journal of Geophysical Research-Oceans*, 113(C5), 19.

Cisewski, B., Strass, V. H. and Prandke, H. (2005) 'Upper-ocean vertical mixing in the Antarctic Polar Front Zone', *Deep Sea Research Part II: Topical Studies in Oceanography*, 52(9-10), 1087-1108.

Comiso, J. C. and Gordon, A. L. (1996) 'Cosmonaut polynya in the Southern Ocean: Structure and variability', *Journal of Geophysical Research: Oceans*, 101(C8), 18297-18313.

Cunningham, S. A., Alderson, S. G., King, B. A. and Brandon, M. A. (2003) 'Transport and variability of the Antarctic Circumpolar Current in Drake Passage', *Journal of Geophysical Research-Oceans*, 108(C5).

de Steur, L., Holland, D. M., Muench, R. D. and McPhee, M. G. (2007) 'The warm-water "Halo" around Maud Rise: Properties, dynamics and Impact', *Deep Sea Research Part I: Oceanographic Research Papers*, 54(6), 871-896.

Deacon, G. E. R. (1979) 'WEDDELL GYRE', *Deep-Sea Research Part a-Oceanographic Research Papers*, 26(9), 981-995.

Doos, K. (1995) 'INTEROCEAN EXCHANGE OF WATER MASSES', *Journal of Geophysical Research-Oceans*, 100(C7), 13499-13514.

Eberhard, F., Gerd, R., Norbert, S., Michael, S., ouml, der, Volker, S. and Andreas, W. (1995) 'Formation and discharge of deep and bottom water in the northwestern Weddell Sea', *Journal of Marine Research*, 53(4), 515-538.

Fahrbach, E., Hoppema, M., Rohardt, G., Boebel, O., Klatt, O. and Wisotzki, A. (2011) 'Warming of deep and abyssal water masses along the Greenwich meridian on decadal time scales: The Weddell gyre as a heat buffer', *Deep Sea Research Part II: Topical Studies in Oceanography*, 58(25–26), 2509-2523.

Fahrbach, E., Hoppema, M., Rohardt, G., Schroder, M. and Wisotzki, A. (2004) 'Decadal-scale variations of water mass properties in the deep Weddell Sea', *Ocean Dynamics*, 54(1), 77-91.

Fahrbach, E., Hoppema, M., Rohardt, G., Schröder, M. and Wisotzki, A. (2006) 'Causes of deep-water variation: Comment on the paper by L.H. Smedsrud "Warming of the deep water in the Weddell Sea along the Greenwich meridian: 1977-2001"', *Deep Sea Research Part I: Oceanographic Research Papers*, 53(3), 574-577.

Fahrbach, E., Rohardt, G., Schroder, M. and Strass, V. (1994) 'Transport and structure of the Weddell Gyre', *Annales Geophysicae*, 12, 840-855.

Firing, E. (1991) *Acoustic Doppler current profiling measurements and navigation*, WHPO 91-9, WOCE Report. 68/91, 24 pp.

Flores, H., van Franeker, J.-A., Cisewski, B., Leach, H., Van de Putte, A. P., Meesters, E., Bathmann, U. and Wolff, W. J. (2011) 'Macrofauna under sea ice and in the open surface layer of the Lazarev Sea, Southern Ocean', *Deep Sea Research Part II: Topical Studies in Oceanography*, 58(19–20), 1948-1961.

Flores, H., van Franeker, J. A., Siegel, V., Haraldsson, M., Strass, V., Meesters, E. H., Bathmann, U. and Wolff, W. J. (2012) 'The Association of Antarctic Krill <italic>Euphausia superba</italic> with the Under-Ice Habitat', *PLoS ONE*, 7(2), e31775.

Ganachaud, A. and Wunsch, C. (2000) 'Improved estimates of global ocean circulation, heat transport and mixing from hydrographic data', *Nature*, 408(6811), 453-457.

Garabato, A. C. N., Polzin, K. L., King, B. A., Heywood, K. J. and Visbeck, M. (2004) 'Widespread intense turbulent mixing in the Southern Ocean', *Science*, 303(5655), 210-213.

Garabato, A. C. N., Stevens, D. P. and Heywood, K. J. (2003) 'Water mass conversion, fluxes, and mixing in the Scotia Sea diagnosed by an inverse model', *Journal of Physical Oceanography*, 33(12), 2565-2587.

Georgi, D. T. and Toole, J. M. (1982) 'The Antarctic Circumpolar Current and the oceanic heat and freshwater budgets', *Journal of Marine Research*, 40(S), 183-197.

Gille, S. T. (2002) 'Warming of the Southern Ocean since the 1950s', *Science*, 295(5558), 1275-1277.

Gille, S. T. (2003a) 'Float Observations of the Southern Ocean. Part I: Estimating Mean Fields, Bottom Velocities, and Topographic Steering', *Journal of Physical Oceanography*, 33(6), 1167-1181.

Gille, S. T. (2003b) 'Float Observations of the Southern Ocean. Part II: Eddy Fluxes', *Journal of Physical Oceanography*, 33(6), 1182-1196.

Gladyshev, S., Arhan, M., Sokov, A. and Speich, S. (2008) 'A hydrographic section from South Africa to the southern limit of the Antarctic Circumpolar Current at the Greenwich meridian', *Deep-Sea Research Part I-Oceanographic Research Papers*, 55(10), 1284-1303.

Gordon, A. L. and Huber, B. A. (1995) 'Warm Weddell Deep Water west of Maud Rise', *Journal of Geophysical Research: Oceans*, 100(C7), 13747-13753.

Gordon, A. L., Huber, B. A., Hellmer, H. H. and Ffield, A. (1993) 'DEEP AND BOTTOM WATER OF THE WEDDELL SEAS WESTERN RIM', *Science*, 262(5130), 95-97.

Gordon, A. L., Martinson, D. G. and Taylor, H. W. (1981) 'The wind-driven circulation in the Weddell-Enderby Basin', *Deep Sea Research Part A. Oceanographic Research Papers*, 28(2), 151-163.

Gordon, A. L., Molinelli, E. and Baker, T. (1978) 'Large-scale relative dynamic topography of the Southern Ocean', *Journal of Geophysical Research: Oceans*, 83(C6), 3023-3032.

Gordon, A. L., Visbeck, M. and Huber, B. (2001) 'Export of Weddell Sea Deep and Bottom Water', *Journal of Geophysical Research-Oceans*, 106(C5), 9005-9017.

Gouretski, V. (1997) *The large-scale thermohaline structure of the Ross Gyre*, translated by Spezie, G. M. G. M. R., Lerici, Italy: Springer-Verlag Italia, 77-100.

Gouretski, V. V. and Danilov, A. I. (1993) 'WEDDELL GYRE - STRUCTURE OF THE EASTERN BOUNDARY', *Deep-Sea Research Part I-Oceanographic Research Papers*, 40(3), 561-582.

Gouretski, V. V. and Danilov, A. I. (1994) 'Characteristics of warm rings in the African sector of the Antarctic Circumpolar Current', *Deep Sea Research Part I: Oceanographic Research Papers*, 41(8), 1131-1157.

Graham, J. A., Heywood, K. J., Chavanne, C. P. and Holland, P. R. (2013) 'Seasonal variability of water masses and transport on the Antarctic continental shelf and slope in the southeastern Weddell Sea', *Journal of Geophysical Research: Oceans*, 118(4), 2201-2214.

Grumbine, R. W. (1991) 'A MODEL OF THE FORMATION OF HIGH-SALINITY SHELF WATER ON POLAR CONTINENTAL SHELVES', *Journal of Geophysical Research-Oceans*, 96(C12), 22049-22062.

Heywood, K. J., Garabato, A. C. N. and Stevens, D. P. (2002) 'High mixing rates in the abyssal Southern Ocean', *Nature*, 415(6875), 1011-1014.

Heywood, K. J., Garabato, A. C. N., Stevens, D. P. and Muench, R. D. (2004) 'On the fate of the Antarctic Slope Front and the origin of the Weddell Front', *Journal of Geophysical Research-Oceans*, 109(C6).

Heywood, K. J., Muench, R. and Williams, G. (2012) 'An Overview of the Synoptic Antarctic Shelf-Slope Interactions (SASSI) project for the International Polar Year', *Ocean Science*, 8(6), 1111-1116.

Hibbert, A., Leach, H., Strass, V. and Cisewski, B. (2009) 'Mixing in cyclonic eddies in the Antarctic Circumpolar Current', *Journal of Marine Research*, 67(1), 1-23.

Jackett, D. R. and McDougall, T. J. (1997) 'A neutral density variable for the world's oceans', *Journal of Physical Oceanography*, 27(2), 237-263.

Jacobs, S. S. (1991) 'On the nature and significance of the Antarctic Slope Front', *Marine Chemistry*, 35(1–4), 9-24.

Joseph, B. and Legras, B. (2002) 'Relation between Kinematic Boundaries, Stirring, and Barriers for the Antarctic Polar Vortex', *Journal of the Atmospheric Sciences*, 59(7), 1198-1212.

Joyce, T. M. (1989) 'On In Situ "Calibration" of Shipboard ADCPs', *Journal of Atmospheric and Oceanic Technology*, 6(1), 169-172.

Jullion, L., Jones, S. C., Garabato, A. C. N. and Meredith, M. P. (2010) 'Wind-controlled export of Antarctic Bottom Water from the Weddell Sea', *Geophysical Research Letters*, 37.

Klatt, O., Fahrbach, E., Hoppema, M. and Rohardt, G. (2005) 'The transport of the Weddell Gyre across the Prime Meridian', *Deep Sea Research Part II: Topical Studies in Oceanography*, 52(3-4), 513-528.

Kouketsu, S., Doi, T., Kawano, T., Masuda, S., Sugiura, N., Sasaki, Y., Toyoda, T., Igarashi, H., Kawai, Y., Katsumata, K., Uchida, H., Fukasawa, M. and Awaji, T. (2011) 'Deep ocean heat content changes estimated from observation and reanalysis product and their influence on sea level change', *Journal of Geophysical Research: Oceans*, 116(C3), C03012.

Lauderdale, J., Garabato, A. N., Oliver, K. C., Follows, M. and Williams, R. (2013) 'Wind-driven changes in Southern Ocean residual circulation, ocean carbon reservoirs and atmospheric CO2', *Climate Dynamics*, 41(7-8), 2145-2164.

Leach, H. (1986) 'THE ANALYSIS OF CURRENTS MEASURED FROM A MOVING SHIP IN THE REGION OF THE NORTH-ATLANTIC POLAR FRONT', *Deep-Sea Research Part a-Oceanographic Research Papers*, 33(8), 1069-1081.

Leach, H., Strass, V. and Cisewski, B. (2011) 'Modification by lateral mixing of the Warm Deep Water entering the Weddell Sea in the Maud Rise region', *Ocean Dynamics*, 61(1), 51-68.

Ledwell, J. R., St. Laurent, L. C., Girton, J. B. and Toole, J. M. (2010) 'Diapycnal Mixing in the Antarctic Circumpolar Current', *Journal of Physical Oceanography*, 41(1), 241-246.

Ledwell, J. R., Watson, A. J. and Law, C. S. (1998) 'Mixing of a tracer in the pycnocline', *Journal of Geophysical Research-Oceans*, 103(C10), 21499-21529.

Leinweber, V. T. and Jokat, W. (2012) 'The Jurassic history of the Africa–Antarctica corridor — new constraints from magnetic data on the conjugate continental margins', *Tectonophysics*, 530–531(0), 87-101.

Losch, M., Redler, R. and Schroter, J. (2002) 'Estimating a mean ocean state from hydrography and sea-surface height data with a nonlinear inverse section model: Twin experiments with a synthetic dataset', *Journal of Physical Oceanography,* 32(7), 2096-2112.

Losch, M. and Schroter, J. (2004) 'Estimating the circulation from hydrography and satellite altimetry in the Southern Ocean: limitations imposed by the current geoid models', *Deep-Sea Research Part I-Oceanographic Research Papers,* 51(9), 1131-1143.

Macdonald, A. M. (1998) 'The global ocean circulation: a hydrographic estimate and regional analysis', *Progress In Oceanography,* 41(3), 281-382.

Mantyla, A. W. and Reid, J. L. (1983) 'ABYSSAL CHARACTERISTICS OF THE WORLD OCEAN WATERS', *Deep-Sea Research Part a-Oceanographic Research Papers,* 30(8), 805-&.

Margules, M. (1906) 'Über Temperaturschichtung in stationär bewegter und ruhender Luft', *Hann-Band. Meteor. Z,* 23, 243-254.

Marshall, J. and Radko, T. (2006) 'A model of the upper branch of the meridional overturning of the southern ocean', *Progress In Oceanography,* 70(2–4), 331-345.

Marshall, J. and Speer, K. (2012) 'Closure of the meridional overturning circulation through Southern Ocean upwelling', *Nature Geosci,* advance online publication.

Martinson, D. G., Stammerjohn, S. E., Iannuzzi, R. A., Smith, R. C. and Vernet, M. (2008) 'Western Antarctic Peninsula physical oceanography and spatio-temporal variability', *Deep-Sea Research Part Ii-Topical Studies in Oceanography,* 55(18-19), 1964-1987.

McCartney, M. S. and Donohue, K. A. (2007) 'A deep cyclonic gyre in the Australian-Antarctic Basin', *Progress In Oceanography,* 75(4), 675-750.

McDonagh, E. L., Bryden, H. L., King, B. A. and Sanders, R. J. (2008) 'The circulation of the Indian Ocean at 32 degrees S', *Progress In Oceanography,* 79(1), 20-36.

Meredith, M. P. and Hogg, A. M. (2006) 'Circumpolar response of Southern Ocean eddy activity to a change in the Southern Annular Mode', *Geophysical Research Letters,* 33(16).

Meredith, M. P., Schofield, O., Newman, L., Urban, E. and Sparrow, M. (2013) 'The vision for a Southern Ocean Observing System', *Current Opinion in Environmental Sustainability,* 5(3–4), 306-313.

Meredith, M. P., Woodworth, P. L., Chereskin, T. K., Marshall, D. P., Allison, L. C., Bigg, G. R., Donohue, K., Heywood, K. J., Hughes, C. W., Hibbert, A., Hogg, A. M., Johnson, H. L., Jullion, L., King, B. A., Leach, H., Lenn, Y.-D., Maqueda, M. A. M., Munday, D. R., Garabato, A. C. N., Provost, C., Sallée, J.-B. and Sprintall, J. (2011) 'SUSTAINED

MONITORING OF THE SOUTHERN OCEAN AT DRAKE PASSAGE: PAST ACHIEVEMENTS AND FUTURE PRIORITIES', *Reviews of Geophysics,* 49.

Meyer, B., Fuentes, V., Guerra, C., Schmidt, K., Atkinson, A., Spahic, S., Cisewski, B., Freier, U., Olariaga, A. and Bathmann, U. (2009) 'Physiology, growth, and development of larval krill Euphausia superba in autumn and winter in the Lazarev Sea, Antarctica', *Limnology and Oceanography,* 54(5), 1595-1614.

Moore, J. K., Abbott, M. R. and Richman, J. G. (1999) 'Location and dynamics of the Antarctic Polar Front from satellite sea surface temperature data', *Journal of Geophysical Research: Oceans,* 104(C2), 3059-3073.

Muench, R., Padman, L., Gordon, A. and Orsi, A. (2009) 'A dense water outflow from the Ross Sea, Antarctica: Mixing and the contribution of tides', *Journal of Marine Systems,* 77(4), 369-387.

Muench, R. D., Morison, J. H., Padman, L., Martinson, D., Schlosser, P., Huber, B. and Hohmann, R. (2001) 'Maud Rise revisited', *Journal of Geophysical Research-Oceans,* 106(C2), 2423-2440.

Munk, W. H. (1950) 'ON THE WIND-DRIVEN OCEAN CIRCULATION', *Journal of Meteorology,* 7(2), 79-93.

Munk, W. H. (1966) 'Abyssal recipes', *Deep Sea Research and Oceanographic Abstracts,* 13(4), 707-730.

Naveira Garabato, A. C., Ferrari, R. and Polzin, K. L. (2011) 'Eddy stirring in the Southern Ocean', *Journal of Geophysical Research: Oceans,* 116(C9), C09019.

Naveira Garabato, A. C., Heywood, K. J. and Stevens, D. P. (2002a) 'Modification and pathways of Southern Ocean Deep Waters in the Scotia Sea', *Deep Sea Research Part I: Oceanographic Research Papers,* 49(4), 681-705.

Naveira Garabato, A. C., McDonagh, E. L., Stevens, D. P., Heywood, K. J. and Sanders, R. J. (2002b) 'On the export of Antarctic Bottom Water from the Weddell Sea', *Deep Sea Research Part II: Topical Studies in Oceanography,* 49(21), 4715-4742.

Naveira Garabato, A. C., Oliver, K. I. C., Watson, A. J. and Messias, M.-J. (2004) 'Turbulent diapycnal mixing in the Nordic seas', *Journal of Geophysical Research: Oceans,* 109(C12), C12010.

Nunes Vaz, R. A. and Lennon, G. W. (1996) 'Physical oceanography of the Prydz Bay region of Antarctic waters', *Deep Sea Research Part I: Oceanographic Research Papers,* 43(5), 603-641.

Núñez-Riboni, I. and Fahrbach, E. (2009) 'Seasonal variability of the Antarctic Coastal Current and its driving mechanisms in the Weddell Sea', *Deep Sea Research Part I: Oceanographic Research Papers*, 56(11), 1927-1941.

Okubo, A. (1971) 'OCEANIC DIFFUSION DIAGRAMS', *Deep-Sea Research*, 18(8), 789-&.

Olbers, D., Borowski, D., VÖLker, C. and WÖLff, J.-O. (2004) 'The dynamical balance, transport and circulation of the Antarctic Circumpolar Current', *Antarctic Science*, 16(04), 439-470.

Orsi, A. H., Johnson, G. C. and Bullister, J. L. (1999) 'Circulation, mixing, and production of Antarctic Bottom Water', *Progress In Oceanography*, 43(1), 55-109.

Orsi, A. H., Nowlin, W. D. and Whitworth, T. (1993) 'ON THE CIRCULATION AND STRATIFICATION OF THE WEDDELL GYRE', *Deep-Sea Research Part I-Oceanographic Research Papers*, 40(1), 169-203.

Orsi, A. H., Whitworth, T. and Nowlin, W. D. (1995) 'ON THE MERIDIONAL EXTENT AND FRONTS OF THE ANTARCTIC CIRCUMPOLAR CURRENT', *Deep-Sea Research Part I-Oceanographic Research Papers*, 42(5), 641-673.

Orsi, A. H. and Wiederwohl, C. L. (2009) 'A recount of Ross Sea waters', *Deep-Sea Research Part Ii-Topical Studies in Oceanography*, 56(13-14), 778-795.

Padman, L., Fricker, H. A., Coleman, R., Howard, S. and Erofeeva, L. (2002) 'A new tide model for the Antarctic ice shelves and seas', *Annals of Glaciology*, 34(1), 247-254.

Pakhomov, E. A., Dubischar, C. D., Hunt, B. P. V., Strass, V., Cisewski, B., Siegel, V., von Harbou, L., Gurney, L., Kitchener, J. and Bathmann, U. (2011) 'Biology and life cycles of pelagic tunicates in the Lazarev Sea, Southern Ocean', *Deep Sea Research Part II: Topical Studies in Oceanography*, 58(13–16), 1677-1689.

Pardo, P. C., Pérez, F. F., Velo, A. and Gilcoto, M. (2012) 'Water masses distribution in the Southern Ocean: Improvement of an extended OMP (eOMP) analysis', *Progress In Oceanography*, 103(0), 92-105.

Patterson, S. L. and Sievers, H. A. (1980) 'THE WEDDELL-SCOTIA CONFLUENCE', *Journal of Physical Oceanography*, 10(10), 1584-1610.

Peterson, R. G. and Whitworth, T. (1989) 'THE SUB-ANTARCTIC AND POLAR FRONTS IN RELATION TO DEEP-WATER MASSES THROUGH THE SOUTHWESTERN ATLANTIC', *Journal of Geophysical Research-Oceans*, 94(C8), 10817-&.

Pollard, R. and Read, J. (1989) 'A Method for Calibrating Shipmounted Acoustic Doppler Profilers and the Limitations of Gyro Compasses', *Journal of Atmospheric and Oceanic Technology*, 6(6), 859-865.

Polzin, K. L., Toole, J. M., Ledwell, J. R. and Schmitt, R. W. (1997) 'Spatial variability of turbulent mixing in the abyssal ocean', *Science*, 276(5309), 93-96.

Press, F. (1968) 'Earth models obtained by Monte Carlo Inversion', *Journal of Geophysical Research*, 73(16), 5223-5234.

Purkey, S. G. and Johnson, G. C. (2010) 'Warming of Global Abyssal and Deep Southern Ocean Waters between the 1990s and 2000s: Contributions to Global Heat and Sea Level Rise Budgets*', *Journal of Climate*, 23(23), 6336-6351.

Rintoul, S. R. (1991) 'SOUTH-ATLANTIC INTERBASIN EXCHANGE', *Journal of Geophysical Research-Oceans*, 96(C2), 2675-2692.

Rintoul, S. R. and Wunsch, C. (1991) 'MASS, HEAT, OXYGEN AND NUTRIENT FLUXES AND BUDGETS IN THE NORTH-ATLANTIC OCEAN', *Deep-Sea Research Part a-Oceanographic Research Papers*, 38, S355-S377.

Robertson, R., Visbeck, M., Gordon, A. L. and Fahrbach, E. (2002) 'Long-term temperature trends in the deep waters of the Weddell Sea', *Deep-Sea Research Part Ii-Topical Studies in Oceanography*, 49(21), 4791-4806.

Sallée, J. B., Speer, K., Rintoul, S. and Wijffels, S. (2010) 'Southern Ocean Thermocline Ventilation', *Journal of Physical Oceanography*, 40(3), 509-529.

Sallée, J. B., Speer, K. and Rintoul, S. R. (2011) 'Mean-flow and topographic control on surface eddy-mixing in the Southern Ocean', *Journal of Marine Research*, 69(4-6), 753-777.

Schröder, M. and Fahrbach, E. (1999) 'On the structure and the transport of the eastern Weddell Gyre', *Deep Sea Research Part II: Topical Studies in Oceanography*, 46(1-2), 501-527.

Sloyan, B. M. (2006) 'Antarctic bottom and lower circumpolar deep water circulation in the eastern Indian Ocean', *Journal of Geophysical Research: Oceans*, 111(C2), C02006.

Sloyan, B. M. and Rintoul, S. R. (2001) 'Circulation, Renewal, and Modification of Antarctic Mode and Intermediate Water*', *Journal of Physical Oceanography*, 31(4), 1005-1030.

Smedsrud, L. H. (2005) 'Warming of the deep water in the Weddell Sea along the Greenwich meridian: 1977-2001', *Deep Sea Research Part I: Oceanographic Research Papers*, 52(2), 241-258.

Smedsrud, L. H. (2006) 'Causes of deep-water variations: Reply to comment by E. Fahrbach, M. Hoppema, G. Rohardt, M. Schröder and A. Wisotzki', *Deep Sea Research Part I: Oceanographic Research Papers*, 53(3), 578-580.

Smetacek, V., Bathmann, U. and Helmke, E. (2005) *The expeditions ANTARKTIS XXI/3-4-5 of the research vessel "Polarstern" in 2004 = Die Expeditionen ANTARKTIS XXI/3-4-5 des Forschungsschiffes "Polarstern" 2004*, 500, Bremerhaven: Alfred Wegener Institute for Polar and Marine Research.

Smith, K. S. and Marshall, J. (2009) 'Evidence for Enhanced Eddy Mixing at Middepth in the Southern Ocean', *Journal of Physical Oceanography*, 39(1), 50-69.

Sokolov, S. and Rintoul, S. R. (2002) 'Structure of Southern Ocean fronts at 140°E', *Journal of Marine Systems*, 37(1–3), 151-184.

Sokolov, S. and Rintoul, S. R. (2009a) 'Circumpolar structure and distribution of the Antarctic Circumpolar Current fronts: 1. Mean circumpolar paths', *Journal of Geophysical Research-Oceans*, 114.

Sokolov, S. and Rintoul, S. R. (2009b) 'Circumpolar structure and distribution of the Antarctic Circumpolar Current fronts: 2. Variability and relationship to sea surface height', *Journal of Geophysical Research-Oceans*, 114.

Strass, V. (2007) *The expedition ANTARKTIS-XXIII/2 of the research vessel "Polarstern" in 2005/2006*, 568, Bremerhaven: Alfred Wegener Institute for Polar and Marine Research.

Sudre, J., Garçon, V., Provost, C., Sennéchael, N., Huhn, O. and Lacombe, M. (2011) 'Short-term variations of deep water masses in Drake Passage revealed by a multiparametric analysis of the ANT-XXIII/3 bottle data', *Deep Sea Research Part II: Topical Studies in Oceanography*, 58(25–26), 2592-2612.

Thompson, A. F. and Sallée, J.-B. (2012) 'Jets and Topography: Jet Transitions and the Impact on Transport in the Antarctic Circumpolar Current', *Journal of Physical Oceanography*, 42(6), 956-972.

Turner, J. and Overland, J. (2009) 'Contrasting climate change in the two polar regions', *Polar Research*, 28(2), 146-164.

Venables, H. J., Pollard, R. T. and Popova, E. E. (2007) 'Physical conditions controlling the development of a regular phytoplankton bloom north of the Crozet Plateau, Southern Ocean', *Deep Sea Research Part II: Topical Studies in Oceanography*, 54(18–20), 1949-1965.

Wang, Z. and Meredith, M. P. (2008) 'Density-driven Southern Hemisphere subpolar gyres in coupled climate models', *Geophysical Research Letters*, 35(14).

Whitworth, T. and Nowlin, W. D. (1987) 'WATER MASSES AND CURRENTS OF THE SOUTHERN-OCEAN AT THE GREENWICH MERIDIAN', *Journal of Geophysical Research-Oceans*, 92(C6), 6462-6476.

Williams, A., Bacon, S. and Cunningham, S. (2006) 'Variability of the Lower Circumpolar Deep Water in Drake Passage 1926–2004', *Geophysical Research Letters*, 33(3), L03603.

Wunsch, C. (1978) 'NORTH-ATLANTIC GENERAL CIRCULATION WEST OF 50-DEGREES-W DETERMINED BY INVERSE METHODS', *Reviews of Geophysics*, 16(4), 583-620.

Zika, J. D., Sloyan, B. M. and McDougall, T. J. (2009) 'Diagnosing the Southern Ocean Overturning from Tracer Fields', *Journal of Physical Oceanography*, 39(11), 2926-2940.